NTNU

Norwegian University of
Science and Technology

Notched Fatigue Behaviour of Additively Manufactured Inconel 718

Klas Solberg

Mechanical Engineering
Submission date: June 2018
Supervisor: Filippo Berto, MTP

Norwegian University of Science and Technology
Department of Mechanical and Industrial Engineering

Preface

This master's thesis was written spring 2018 as the final work in the two year master of science program of mechanical engineering at the department of mechanical and industrial engineering, Norwegian University of Science and Technology. The work is a continuation of my specialisation project "A study of stress distribution in notched components" supervised by Filippo Berto fall 2018, where I was introduced and used the mathematical models proposed by Paolo Lazzarin, which also play an important role in this work.

I would like to thank both Filippo Berto and Jan Torgersen, that will be the supervisors for my PhD, for their support and encouragement this semester and for guiding me finding a novel topic with no previously published results.

I would like to thank Filippo Berto especially for giving me the freedom to shape the task myself, but also guiding me to find interesting ways of looking at problems when it comes to mathematical models and problems related to structural integrity

I would like to thank Jan Torgersen especially for dedicating so much time to me in this work, for including me in his projects and for discussing problems and giving me a lot of good literature guidance related to additive manufacturing.

I would like to thank Seyed Mohammad Javad Razavi, my office mate, for dedicating time to discuss problems and for guiding mechanical testing and use of different microscopes.

Klas Solberg, Trondheim 2018

Abstract

Fatigue behavior for different notch geometries of additively manufactured Inconel 718 produced by Selective Laser Melting is investigated at room temperature. Additive manufacturing enables complex geometries in components by producing parts layer by layer from computer aided 3D models, however the produced surfaces are rough and can contains defects, which strongly influence the mechanical behaviour of respective components. In order to take advantage of the possibilities available concerning topology optimization and the allowed complexity of geometry when fabricating with additive manufacturing for load bearing applications, the notched fatigue behaviour of the materials must be evaluated. Inconel 718 is a Ni-based superalloy with high strength, creep and fatigue resistance at elevated temperatures, commonly used in aerospace industries and other industries with high demands of mechanical properties in extreme conditions.

In this work I investigate the high cycle fatigue strength of different notch geometries produced by additively manufactured Inconel 718 specimens, a topic not yet reported in literature, but of great importance in terms of the complexity of the components currently being designed for additive manufacturing. The fatigue strength is evaluated for four different geometries, one smooth, one semi-circular and two different blunt v-shaped notches. Fractography of the fracture surfaces is done with scanning electron microscopy, showing that the cracks are initiating from surface defects such as lack of fusion in the notched region. Further the fatigue data is analysed by use of the energy based method strain energy density, unifying all the fatigue data in one single notch independent curve predicting the fatigue life.

Sammendrag

Utmattingsegenskaper for forskjellige kjervgeometrier av additivt tilvirket Inconel 718 produsert av selektiv laser smelting, er undersøkt i romtemperatur. Additiv tilvirkning tillater komplekse geometrier i komponenter ved å produserer komponentene lag-for-lag ved hjelp av data assistert konstruksjon, men overflatene til komponentene som er produsert på denne måten er ofte ru, og inneholder defekter, dette kan sterkt påvirke komponentenes levetid og mekaniske egenskaper. For å dra nytte av mulighetene tilgjengelig når det kommer til additiv tilvirkning og topologi optimalisering, for last bærende applikasjoner, er det nødvendig å kartlegge utattingsegenskapene for materialet. Inconel 718 er en Ni-basert legering, med høye mekaniske egenskaper mot utmatting og kryp ved høye temperaturer. Materialet er brukt av flyindustrien og av andre industrier som har høye krav til mekaniske egenskaper ved ekstreme forhold.

I denne oppgaven undersøker jeg utmattingsegenskapene til forskjellige kjervgeometrier produsert ved hjelp av additivt tilvirket Inconel 718, et emne som ennå ikke er rapportert i litteraturen, men som er av stor betydning når det kommer til komplekse komponenter som blir designet og produsert ved hjelp av additiv tilvirkning. Utmattingsegenskapene er evaluert for fire forskjellige kjervgeometrier, en jevn, en semi-sirkulær og to forskjellige sløve v-formede kjerver. Bruddflatene er analysert med sveipelektronmikroskop for å kartlegge hvilke mekanismer som bidrar til utmatting. Mikroskopbildene viser at sprekkene starter ved små defekter i overflatene på prøvene, som oppstår på grunn av mangel på smelting mellom lagene prøvene er produsert i. Videre er utmattinsdataene analysert ved hjelp av gjennomsnittlig kritisk tøyningsengergi, hvor alle utmattingsdataene samles til en kurve, som beskriver utmattingslevetiden som en funksjon av gjennomsnittlig kritisk tøyningsengergi.

Nomenclature

2α	Notch opening angle
$\bar{W}$	Average Strain Energy Density
ΔK	Stress Intensity range / Notch Stress Intensity Range
δ	Laves Phases
$\Delta\bar{W}$	Average Strain Energy Density Range
$\Delta\bar{W}_c$	Critical Average Strain Energy Density Range
$\Delta\sigma$	Stress Range
$\Delta\sigma_a$	Fatigue Strength
γ	Gamma Phase
γ'	Gamma Prime Phase
γ''	Gamma Double Prime Phase
λ	Williams' Eigenvalue
μ	Notch Radius Parameter in P. Lazzarin and R. Tovo Stress Field
ν	Poisson's Ratio
ρ	Notch Radius
σ	Stress
σ_∞	Far Field Stress
σ_a	Stress Amplitude
σ_u	Ultimate tensile Strength
σ_y	Yield Stress
σ_{max}	Maximum Stress
σ_{mean}	Mean Stress
σ_{min}	Minimum Stress
τ	Shear Stress
θ	Angle
ε	Strain
E	Young's Modulus
h	Hour
K	Stress Intensity Factor / Notch Stress Intensity Factor
K	Stress Intensity Factor

k_f	Fatigue Notch Sensitivity
k_t	Elastic Stress Concentration Factor
K_{IC}	Fracture Thougness
l	Length of Specimen
l_0	Length of Notch
N_f	Number of Cycles to Failure
q	Opening Angle Parameter in P. Lazzarin and R. Tovo Stress Field
R	Loading Ratio
r	Distance in Polar Coordinates
R_0	Critical Radius for Strain Energy Density
r_0	Placement of Coordinate System in P. Lazzarin and R. Tovo Stress Field
R_1	Radius of Control Region for Strain Energy Density, Blunt Notch
T	Temperature
t	Thickness
U	Energy
w_1	Width of Specimen
w_2	Width of Specimen in Notched Region
W_c	Critical Strain Energy Density

Acronyms

AC Air Cooling

AM Additive Manufacturing

BCC Body Centre Cubic

BCT Body Centre Tetragonal

EBM Electron Beam Melting

FC Furnace Cooling

FCC Face Cubic Centere

FDM Fused Deposition Modelling

HIP Hot Isostatic Pressure

HT heat Treatment

IN718 Inconel 718

OM Optical Microscope

NSIF Notch Stress Intensity Factor

PBF Powder Bed Fusion

RT Room Temperature

SED Strain Energy Density

SEM Scanning Electron Microscope

SIF Stress Intensity Factor

SLM Selective Laster Melting

SLS Selective Laser Sintering

SP Shoot Peening

UV Ultra Viololett radiation ???

Contents

1 Introduction

1.1 Background

Inconel 718 (IN718) is a Ni-based superalloy with high strength, corrosion and creep resistance at high temperatures. Due to these properties IN718 is commonly used in gas turbine blades, seals, combustors, nuclear reactors, aircraft components, pressure vessels, and in general components requiring high strength in extreme conditions [1]. However, high strength, hardness and thermal conductivity makes it hard to process the material with conventional machining and fabrication methods. Additive Manufacturing (AM) is a new manufacturing method that allows building components in a layer-by-layer method assisted by 3D models created in computer aided software, allowing complex geometries and internal structures not available by machining or other manufacturing methods [2]. Due to the mechanical properties and the possibilities of AM producing IN718 components by use of AM has promising applications in the future. However, mechanical properties for AM components are not yet fully understood and outlined, and engineers are not yet able to design and predict the service life of load bearing components. During fabrication different defects, microstructure, surface roughness, residual stresses can differ based on the process parameters and conditions. Because of the new geometrical complexity available when designing AM components, fatigue strength must be determined, not just determining the material properties of machined AM specimens, but the as-build specimen containing the surface defects and notch geometries likely to be present in an actual designed part.

1.2 Problem Description

AM allows building complex geometries not previously available by conventional fabrication methods such as machining. Because of this engineers can now create designs components containing features like undercuts and internal structures not previously possible to manufacture. Components designed like this could easily result in notched geometries. Few results has been reported in literature on notched fatigue strength in the high cycle regime of AM IN718. This work aims to describe the notched fatigue behaviour of "as-built" additive manufactured IN718 and its failure mechanisms.

1.3 Project Scope

1.3.1 Objectives

The objectives for the work is to determine the fatigue behaviour of notched AM IN718 components, and the driving mechanisms for failure.

1.3.2 Research Questions

- What is the fatigue properties of as-built AM IN718?
- How does notched influence the fatigue life of as-built AM718?
- Is it possible to predict the materials fatigue behaviour using linear elastic models and the energy-based approach of Strain Energy Density?

1.4 Structure of Report

This thesis concerns structural integrity of additive manufactured Ni-based superalloy IN718. The thesis starts by introducing the fundamentals concepts of additive manufacturing. Then it introduces the fundamental concepts of structural integrity, starting at the basic formulations of stress, strain, material models, moving on to elastic stress fields, failure in material, different approaches to fatigue and the energy based concept of strain energy density (SED). Then superalloys are introduced, with some basic metallurgy, then followed by a short review of the mechanical properties of the superalloy IN718. Then a short review is given on the literature published on AM IN718, with focus on fatigue and tensile properties. After this a section describing testing and specimens used for obtaining fatigue properties for the superalloy. Analysis of the specimens used in the testing are done in the finite element (FE) software Abaqus CAE, and by analytical models describing elastic stress fields. The fatigue results are analysed by use of SED. The next section presents the results obtained from testing, the fatigue data is presented both in terms of stress versus number of cycles to failure and average critical strain energy density versus number of cycles to failure. Fractography is performed by use of scanning electron microscopy (SEM), determining the failure mechanisms of the samples, and reasoning for scatter in data. The results obtained in the work is discussed, and in the final section a conclusion summarising the work by answering the research questions is given.

1.5 Literature

The literature used in this thesis can be divided into two categories: Literature used to describe the fundamental concepts and literature used to describe empirical results obtained in special cases. The fundamental concepts explained in the thesis is mainly based and adopted form text books on the same topic, this is stated in the beginning of the section, and the whole section is based on that reference. In the case of explaining some specific results, journal papers are used as references.

2 Additive Manufacturing

In this section an overview of different AM production methods are presented, and some of the most commonly used methods are explained in further detail.

2.1 Introduction to Additive Manufacturing

Additive manufacturing (AM) is a manufacturing process that builds three-dimensional parts by adding material, usually in a layer-by-layer manner. The parts build is based on a digital 3D model of the part. This production technology avoids the geometrical limitations of conventional production technologies, complex parts can be produced directly without use of machining, dies, punches or molds. AM makes is the possible to make designs which does not require assembling like welding, bolts or other joining methods, as complexity of geometry is not an issue. This available complexity in the geometry opens up a new word when it comes to topology optimisation, parts can be optimised for for example strength, heat transfer or vibrations. AM allows parts to be manufactured on demand, this make it possible for industries to reduce inventory by not having all spare parts in storage. Industries like aerospace, medical, automotive, oil and gas, marine and electronics but also consumer products buildings and food industries are looking into using AM. However, the industries are still facing challenges before it is possible to implement this new technology and exploit its full potential [3]. Topological and mechanical properties of the build part evolves during the building process, this should be taken into account when designing for additive manufacturing. Building with overhang will for many processes give bad surface quality, or in sintering methods, that quality is dependent on the heat transfer through the part [4].

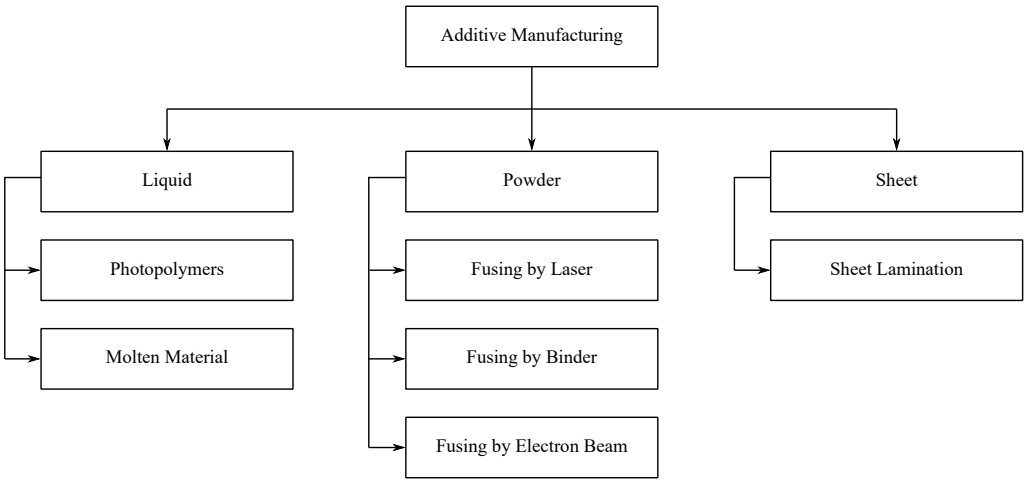

Figure 1: Overview of main AM methods

AM can be divided into three different categories: Liquid-based, powder-based and sheet-based. In the liquid based method components are built up by material solidifying layer by layer. The two most common ways to do this is by curing a photopolymer with UV light layer by layer, or extruding material into a part layer by layer. In the powder based method, the powder are fused together either by use of laser, binder or electron beam layer by layer. Depending on the manufacturing method the material used is in powder form, this powder is

bounded together by different methods (melted, partly melted, glued together etc.) forming a part. In the sheet based method sheets are cut out and attached together. An overview of the most common AM methods are shown in Figure 1.

2.2 Different Methods of Printing

2.2.1 Photopolymerisation

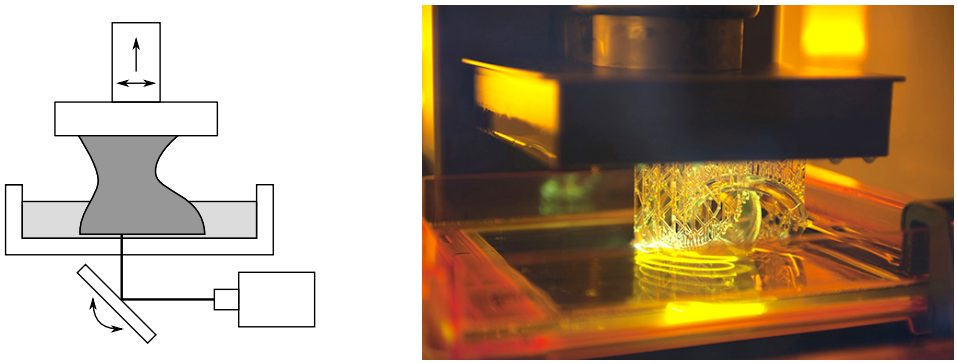

Figure 2: left: Illustration of stereolithography. Build part is lowered down into bath of photopolymer and curved by UV-light. Right: Picture of stereolithography process [5]

In Additive manufacturing by photopolymerisation a liquid photopolymer is stored in a vat, and selectively solidified by scanning a UV light. Stereolitography (SLA) is the most common method of photopolymerisation, by use of laser beam and mirrors the UV light is selectivly scanning the crosssection of the build part, attaching new material to the build part. Then the part is moved up, and the process is repeated, layer-by-layer the parts is built [4]. An illustration of the process is shown in Figure 2. The technology is introduced by Chuck Hull in 1986 as the first AM fabrication method [6]. One of the main advantages with the stereolithography method is the high resolution. Resolutions down to nano scale has been reported in literature by J. Torgersen et al. [7].

2.2.2 Molten Material

Figure 3: Left: Illustration of Fused Deposit Modelling. Right: Picture of FDM process [8].

In Fused Deposition Modelling (FDM) filament is heated and feed (extruded) through a nozzle, creating components layer-by-layer. With the FDM technology it is easy to combine several materials into one part, usually there is one build filament and one support filament, fed though different nozzles [9]. In FDM the material is melted and solidified again, therefor thermoplastics are used, the curing process for thermoplastics are fully reversible, so the material can be liquefied when heated, and solidified when cooled. The FDM-machines often have a cooling element for the extruded material, which ensures a quicker solidification. FDM is often used for rapid prototyping, as the machines can be bought quite cheap, parts are produced fast, the main disadvantage with FDM is the poor resolution [4].

2.2.3 Fusing by Laser

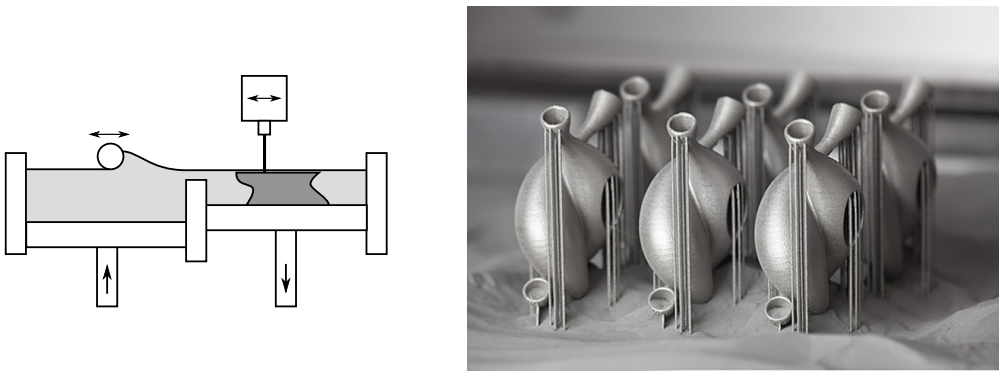

Figure 4: Left: Schematic illustration of powder bed fusion. Right: Picture of parts produced by selective laser melting [10].

Powder Bed Fusion (PBF) is a method similar to sintering. A powder bed is layer-by-layer fused into a component. A schematic illustration of the process and a complete part is shown in Figure 4. A thin layer of powder is melted in a selective manner by a laser or electron beam, then new powder is fed on top of the previous layer, forming a new layer, then this new layer is melted, this process is repeated until the build part is finished. The method can be done by use of binder. Different methods of sintering can be used; solid state sintering, chemically induced binding, liquid phase sintering partial melting or full melting [3].

Selective Laser Melting (SLM) is one of the most common methods of producing metal parts with AM. SLM fuses the powder selectively by use of a laser beam. The process is usually done in a controlled environment containing Ni- or Ar-gas, at temperatures up to 250°C. SLM can be used to produce a wide range of metal alloys including Ti-based, Ni-based, Cu-based and Fe-based. The main advantages with SLM is that one can produce a large range of materials, relatively low cost, and it produces near-to-net complex shaped components. The main disadvantages with SLM is that the process speed is slow, there are size restrictions, surfaces can be rough (depending on process parameters and powder) and high temperature gradients in the build part causing residual stresses [3].

Electron beam melting (EBM) is similar to SLM, but rather than using a laser beam to fuse the powder, an electron beam are used. The process is performed in a vacuum and the powder is heated during processing in order to form sinter-bridges, because of the high temperature during processing the temperature gradients are less steep than in SLM and there are less problems concerning residual stresses. Because of this it is easier to produce

brittle parts without fracturing the components during processing. Optimizing the process parameters is more complex than for SLM, and only a few materials are availible: IN718, Ti6Al4V, Ti-grade 2 and CoCrMo. [3].

2.3 Strategy of Printing

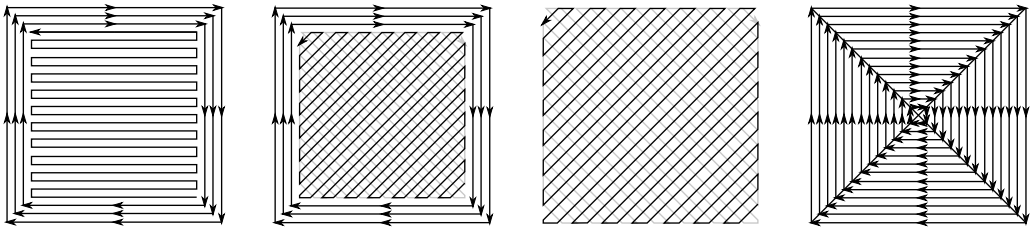

Figure 5: Schematic illustration of different melt strategies [11]

Different melt strategies used in selective AM fabrication methods is shown in Figure 5, where the black lines are illustrating the current layer, while grey lines are illustrating the previous layer. The outer lines are called contours, while the inner lines are called hatching. Different strategies can be used building a part, a common startegy is to use 2 or 3 contours and hatching inside, as hatching is faster [11].

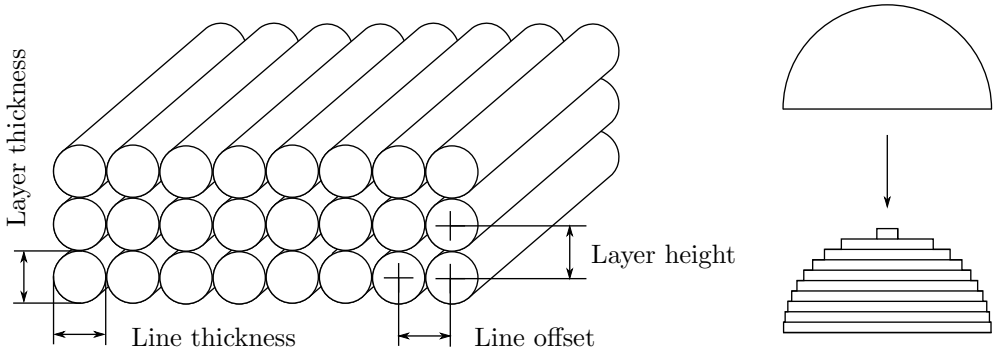

Figure 6: Lines/layers of material building the part.

When building a part by use of AM by selective methods, the part is build up by arrays of lines in layers, this is illustrated in Figure 6. Parameters like line thickness, line offset, layer height and layer thickness are affecting the material and surface quality and the resolution of the part.

2.4 Additive Manufacturing versus Conventional Manufacturing Technologies

The cost per unit is compared to the number of units produced is compared for conventional manufacturing and AM in the graph left in Figure 7. The cost of AM units does not change with the number of units, while for conventional methods, it is expensive for a low number

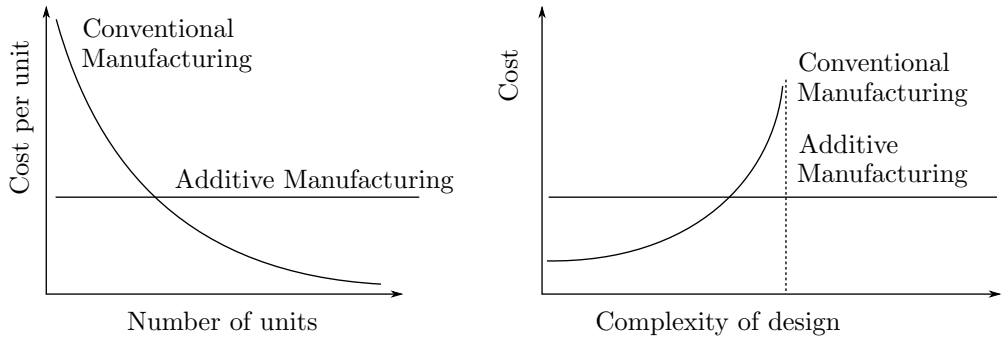

Figure 7: Comparison between conventional manufacturing technologies and additive manufacturing. Left: Cost per unit versus number of units [12]. Right: Cost versus complexity of design [4].

of units and cheaper for a high number of units [12]. The cost versus the complexity of the design in shown right in Figure 7, it shows that the cost of the AM components does not change as the complexity change, while for conventional methods the price gets arbitrarily high at a certain point. These two graphs makes it clear that if a complex design and few number of units are needed AM could be the best choice of manufacturing method.

2.5 Topology Optimization - Challanges

Figure 8: Topology optimised structure by S. Galjaard et al. [13]

Topology optimisation allows for computer assisted engineering tools to optimise geometries in terms of different loads and boundary conditions, this could be stresses, strains, heat transfer, frequencies etc. With AM there is less boundary condition in the topology optimisation due to the fact that there are no or little limitations in terms of complexity of the geometries. When designing with topology optimisation tools, complex geometries are usually generated. S. Galjaard et al. [13] has topology optimised a load bearing component shown in Figure 8. based on the initial and new geometry a comparison between strength, cost and aesthetics has been done. It was reported that downwards facing surfaces with an angle less that 45°needs support structure. The component contains regions with local notches that acts as stress risers that can decrease the fatigue life.

2.6 Example of Application from SpaceX

One high end application of additive manufacturing in the industries is from Elon Musks SpaceX Falcon 9 rocket, where the main oxidizer valve is produced by additive manufactured

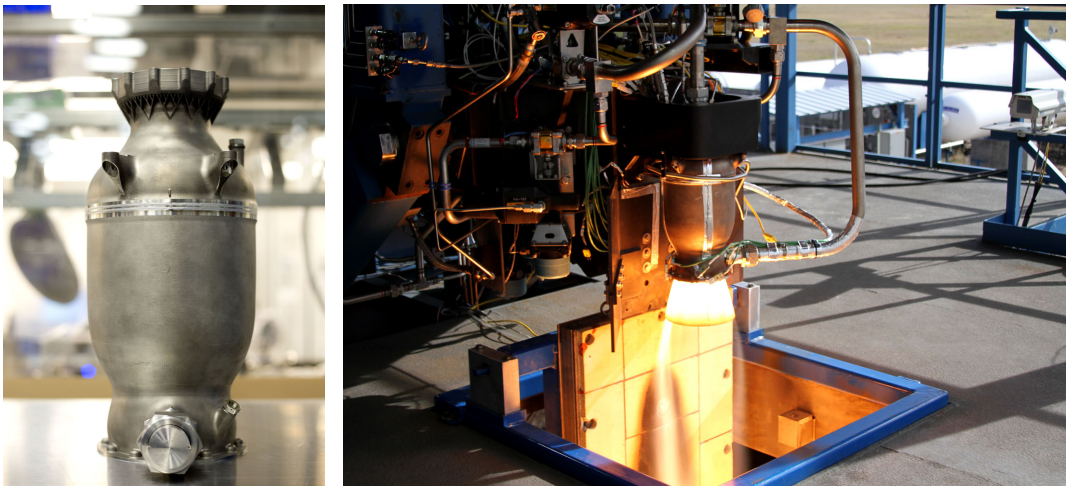

Figure 9: Main oxidizer valve used for SpaceX Falcon 9 rocket [14].

Inconel 718. The valve was printed in two days, while the casting cycle for creating the mold and the part takes several months. When comparing the printed valve with the casted valve, the printed one has superior strength, ductility and fracture resistance, allowing both operating in elevated and cryogenic temperatures [14]. The valve is shown in Figure 9. In order to utilise the possibilities with AM in load bearing applications, high strength alloys such as IN718 and TI6Al4V is often used [2].

3 Structural Integrity

In this section some fundamental concepts concerning mechanical behaviour of materials are explained and defined. The section describes stress, strain, material models, analytical solutions to elastic stress fields, failure in materials, with focus on fatigue and SED.

3.1 Stress

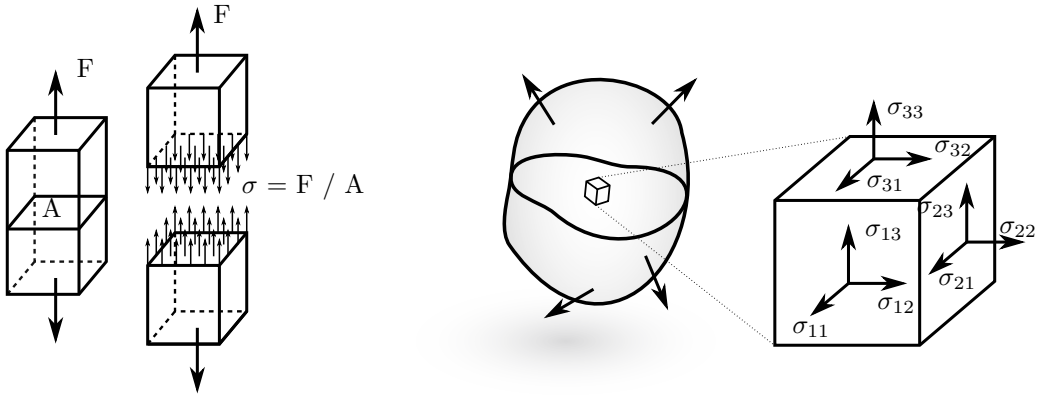

Figure 10: Uniaxial stress and complex stress state

Stress, σ, is defined as force per area. When decomposing the stresses normal stress is acting normal to a surface, while stress action parallel to a surface is called shear stress, τ. For complex stress states the stress state can be expressed for a infinite small element by a 2.order tensor; the Cauchy stress tensor written as [15]:

$$\boldsymbol{\sigma} = \begin{bmatrix} \sigma_{11} & \sigma_{12} & \sigma_{13} \\ \sigma_{21} & \sigma_{22} & \sigma_{23} \\ \sigma_{31} & \sigma_{32} & \sigma_{33} \end{bmatrix} = \begin{bmatrix} \sigma_{11} & \tau_{12} & \tau_{13} \\ \tau_{12} & \sigma_{22} & \tau_{23} \\ \tau_{13} & \tau_{23} & \sigma_{33} \end{bmatrix} \tag{1}$$

For any stress state, the element can be rotated into a position where there are no shear stresses, in position there are only normal stresses, they are called principal stresses.

3.2 Material

Materials response to stress is strain, ε. For a real material the material response is initially following a linear loading path (linear elastic behaviour), after the linear response many materials will experience non-linear behaviour, and in many cases the deformation is no longer elastic but plastic, that is nonrecoverable strain. Figure 11 shows differnet material behaviour, real material behaviour is shown left, initially the material has linear behaviour, with a slope E, the Young's modulus of the material. Then the material reaches its yield strength, σ_y, and starts to deviate from the linear path. At the ultimate tensile strength, σ_u, the material starts to neck, and voids are forming inside the material. At the true fracture strength, σ_f, the material ruptures. The centre graph shows the material behaviour engineers

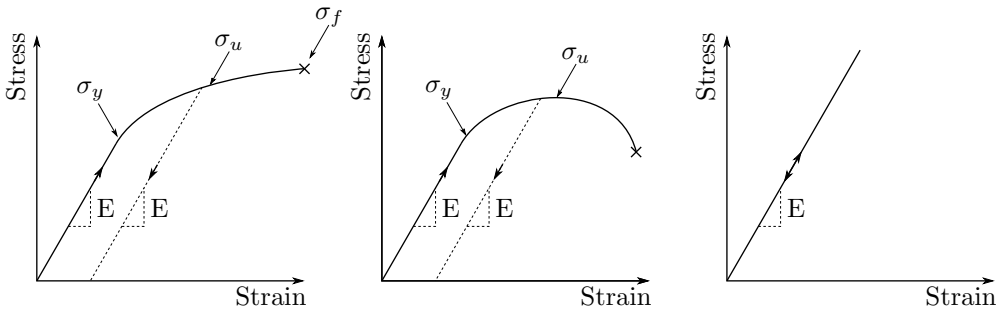

Figure 11: Left: Typical real material behaviour for metal, True stress versus true strain. Centre: Engineering stress versus engineering strain. Left: Linear elastic material used for calculations.

measure considering constant cross sections. The ultimate tensile strength is maximum stress measured. The right graph shows the material model commonly used by engineers when making calculations, this material is elastic and has a linear behaviour. The linear material behaviour can be described by Hooke's law $\sigma = E\varepsilon$. In 3D the law is formulated as [15]:

$$\begin{aligned}
\sigma_{xx} &= \tfrac{E}{(1+\nu)(1-2\nu)}[(1-\nu)\varepsilon_x + \nu(\varepsilon_y + \varepsilon_z)] \\
\sigma_{yy} &= \tfrac{E}{(1+\nu)(1-2\nu)}[(1-\nu)\varepsilon_y + \nu(\varepsilon_x + \varepsilon_z)] \\
\sigma_{zz} &= \tfrac{E}{(1+\nu)(1-2\nu)}[(1-\nu)\varepsilon_z + \nu(\varepsilon_x + \varepsilon_y)]
\end{aligned} \tag{2}$$

Where ν is the Poisson's ratio defined as the ratio of transverse strain to axial strain.

3.3 Notch

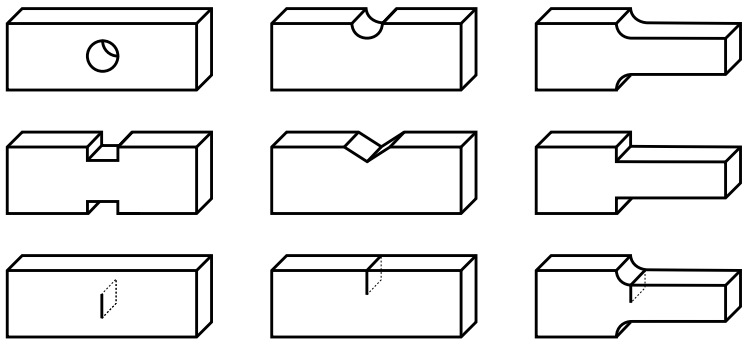

Figure 12: Schematic illustration of different notch and crack geometries. Top: Blunt notches. Middle: Sharp notches. Bottom: Cracks

A notch is a geometric configuration in a member, that potentially can cause perturbation of the stress field. Figure 12 Shows different notch geometries [16]. When dealing with notches there are several parameters used to describe the notch mathematically, these parameters

varies in the different mathematical models. Notch radius, opening angle and notch bisector line is shown in Figure 13. In this report different types of notch geometries will be characterised the following way:

Blunt notch When the notch has a finite radius, the notch is characterised as a blunt notch.

Sharp notch When the notch has a radius equal to zero, the notch is characterised as a sharp notch.

V-shaped notch When the notch has a constant opening angle, the notch is characterised as v-shaped.

Semi-circular notch When the notch has a notch radius with its centre at the edge of the component, the notch is characterised as semi-circular.

Crack When the notch radius is equal to zero and opening angle equal to zero the notch is characterised as a crack.

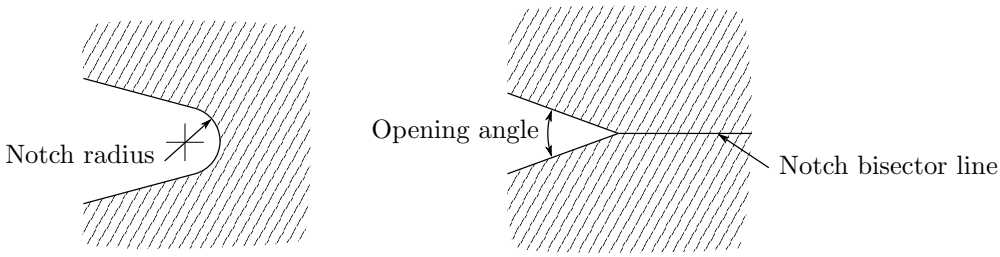

Figure 13: Schematic illustration of important parameters concerning notches.

When dealing with notches and crack the loading are divided into thre different loading modes; Mode I - Opening, Mode II - In-plane shear and Mode III - Out-of-plane shear [15]. Theses different loading modes are shown in Figure 14.

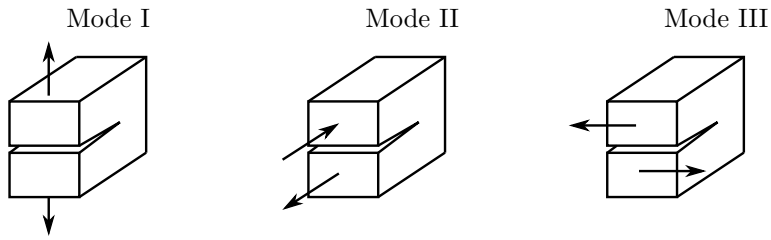

Figure 14: Modes of loading when dealing with cracks and notches.

3.4 Mathematical Models Describing Elastic Stress Fields

In this section some of the analytical mathematical models for describing linear elastic stress field surrounding notches and cracks analytically are presented. If the stress field in a member is perturbed, the magnitude of the stress increases in the perturbed area. The models used are shown for plane problems, and the solution to the stress fields presented are only for mode I loading.

3.4.1 Kirch's Solution

In 1898 Ernst Gustav Kirsch developed a method for describing stress fields for linear elastic materials around a hole in plate, as shown in Figure 15. Kirch's solution is formulated as [17]:

$$\begin{aligned}
\sigma_{rr} = &\frac{\sigma_\infty}{2}\left[1-\left(\frac{a}{r}\right)^2\right]+\frac{\sigma_\infty}{2}\left[1-4\left(\frac{a}{r}\right)^2+3\left(\frac{a}{r}\right)^4\right]\cos 2\theta \\
\sigma_{\theta\theta} = &\frac{\sigma_\infty}{2}\left[1+\left(\frac{a}{r}\right)^2\right]-\frac{\sigma_\infty}{2}\left[1+3\left(\frac{a}{r}\right)^4\right]\cos 2\theta \qquad (3)\\
\tau_{r\theta} = &-\frac{\sigma_\infty}{2}\left[1+\left(\frac{a}{r}\right)^2\right]-\frac{\sigma_\infty}{2}\left[1+2\left(\frac{a}{r}\right)^2-3\left(\frac{a}{r}\right)^2\right]\sin 2\theta
\end{aligned}$$

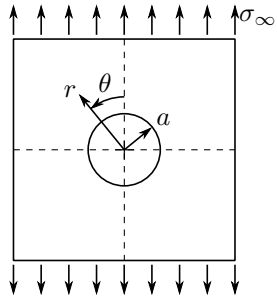

Figure 15: Geometry of Kirch solution

When $\theta = \pm\pi/2$ the tangential stress component is $\sigma_{\theta\theta} = 3\sigma_\infty$. The stress at the tip of the hole is not dependent on the radius of the hole.

3.4.2 Inglis's Solution

In 1913 Charles Inglis developed a solution for stress fields around elliptical holes in plates. The maximum stress at the tip sharp tip of the ellipse is given as [18]:

$$\sigma_{max} = \sigma_\infty\left(1+2\frac{a}{b}\right) = \sigma_\infty\left(1+2\sqrt{\frac{a}{\rho}}\right) \qquad (4)$$

The stress can be expressed in terms of the radius of the ellipse, and the solution predicts that when the ellipse collapses ($\rho \to 0$) and becomes a crack the stress at the tip of the ellipse tends to infinite.

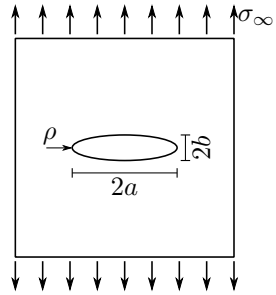

Figure 16: Geometry of Inglis solution

3.4.3 Westergaard's Solution

In 1939 H. M. Westergaard developed a solution for describing the stresses surrounding cracks in biaxial tension. The solution is developed in rectangular coordinates, with a coordinate system: $z = x+iy$. A complex stress function, $Z(z) = Re(Z)+Im(Z)$, is used to to define an Airy stress function. The coordinate system is translated to the crack tip and the following stress field is obtained [15]:

$$\sigma_{xx} = \frac{K_I}{\sqrt{2\pi r}}\cos\left(\frac{\theta}{2}\right)\left[1-\sin\left(\frac{\theta}{2}\right)\sin\left(\frac{3\theta}{2}\right)\right] \qquad (5)$$

$$\sigma_{yy} = \frac{K_I}{\sqrt{2\pi r}}\cos\left(\frac{\theta}{2}\right)\left[1+\sin\left(\frac{\theta}{2}\right)\sin\left(\frac{3\theta}{2}\right)\right] \qquad (6)$$

$$\tau_{xy} = \frac{K_I}{\sqrt{2\pi r}}\cos\left(\frac{\theta}{2}\right)\sin\left(\frac{\theta}{2}\right) \qquad (7)$$

This solution also shows a singularity at the crack tip, Westergaard described this singularity

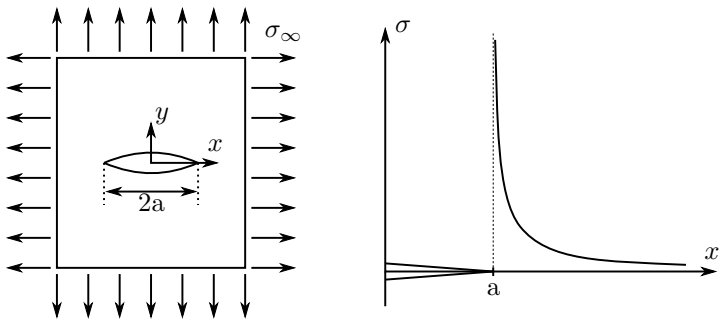

Figure 17: Left: Schematic illustration of geometry of Westergaard's solution. The crack length is given by 2a and the plate is under biaxial tension. Right: Schematic illustration of the stress along $y = 0$.

by use of stress intensity. The stress field is expressed in terms of the distance from crack tip, r, angle θ and mode I stress intensity , K_I. The solution predicts a $1/\sqrt{r}$ singularity at the crack tip as shown right in Figure 17. The solution is also derived for mode II loading, but will not be shown in this work.

3.4.4 Williams' Solution

In 1952 M. L. Williams developed a method for determining the stress fields at the tip a sharp v-shaped notches [19]. Williams showed that the stress at the tip of a v-shaped notch can be expressed by an infinite series where $1/\sqrt{r}$ is the leading term. A semi infinite wedge element as shown in Figure 18 is used. The angles are set to be $\alpha = \beta$, so that the wedge forms a sharp notch, for this solution the opening angle is given by $2\pi - 2\alpha$. The solution is developed based on polar coordinate system at the notch tip.

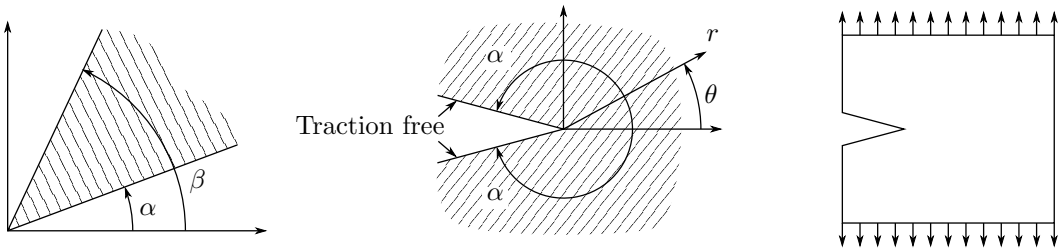

Figure 18: Left: Arbitrary wedge element. Middle: Semi-infinite sharp notch. Right: Notched plate in tension.

When the opening opening angle of the notch is zero the stress fields for mode I loading can

be expressed as:

$$\begin{aligned}
\sigma_{rr} &= \frac{K_I}{\sqrt{2\pi r}}\left[\frac{5}{4}\cos\left(\frac{\theta}{2}\right) - \frac{1}{4}\cos\left(\frac{3\theta}{2}\right)\right] \\
\sigma_{\theta\theta} &= \frac{K_I}{\sqrt{2\pi r}}\left[\frac{3}{4}\cos\left(\frac{\theta}{2}\right) + \frac{1}{4}\cos\left(\frac{3\theta}{2}\right)\right] \\
\tau_{r\theta} &= \frac{K_I}{\sqrt{2\pi r}}\left[\frac{1}{4}\sin\left(\frac{\theta}{2}\right) + \frac{1}{4}\sin\left(\frac{3\theta}{2}\right)\right]
\end{aligned} \tag{8}$$

3.4.5 P. Lazzarin and R. Tovo Solution

P. Lazzarin and R.Tovo method gives a unifying mathematical approach for evaluation linear elastic stress fields around cracks, sharp notches and blunt notches [20]. The coordinate system and notch geometries are shown in Figure 19.

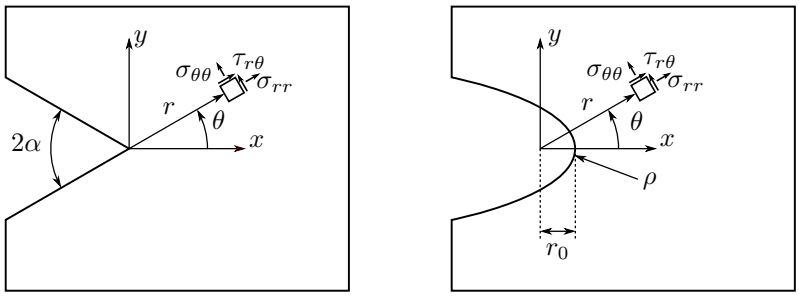

Figure 19: Geometry, stress components and coordinate system for the Lazzarin-Tovo solution. Left: Sharp notch. Right: Blunt notch.

The different notch geometries are described using a curvilinear coordinate system defined as:

$$x + iy = r^{i\theta} = z = w^q = (u + iv)^q \tag{9}$$

Where the opening angle, 2α, can be expressed in terms of q by $2\alpha = \pi(2 - q)$. Further the notch radius, ρ, at the notch bisector line is given by:

$$\rho = \frac{qr_0}{q-1} \tag{10}$$

The stress field for mode I loading is expressed as:

$$\begin{aligned}
\begin{bmatrix} \sigma_{\theta\theta} \\ \sigma_{rr} \\ \tau_{r\theta} \end{bmatrix} = &\frac{1}{\sqrt{2\pi}} \frac{r^{\lambda_1 - 1} K_I}{(1+\lambda_1) + X(1-\lambda_1)} \Bigg[\Bigg[\begin{bmatrix} (1+\lambda_1)\cos(1-\lambda_1)\theta \\ (3-\lambda_1)\cos(1-\lambda_1)\theta \\ (1-\lambda_1)\cos(1-\lambda_1)\theta \end{bmatrix} \\
&+ X_1(1-\lambda_1) \begin{bmatrix} \cos(1+\lambda_1)\theta \\ -\cos(1+\lambda_1)\theta \\ \sin(1+\lambda_1)\theta \end{bmatrix} \Bigg] \\
&+ \left(\frac{r}{r_0}\right)^{\mu_1 - \lambda_1} [(3-\lambda_1) - X_1(1-\lambda_1)] \begin{bmatrix} \cos(1+\mu_1)\theta \\ -\cos(1+\mu_1)\theta \\ \sin(1+\mu_1)\theta \end{bmatrix} \Bigg]
\end{aligned} \tag{11}$$

Where λ, μ and X are parameters dependent on the geometry of the notch, and K_I, in the case of a crack the stress intensity factors (SIF) or in the case of notch, the notch stress

intensity factors (NSIF) for mode I loading. The mathematical models is described in more detail in Appendix A.

3.5 Failure in Materials

The following section is based on Ted L. Anderson textbook Fracture Mechanics: Fundamentals and Applications [15].

A failure criteria is a mathematical model, which based on empirical data tries to predict failure in a material, based on some level of stress, strain, energy or other load. Many failure criterias uses a critical level of stresses to predict failure. If the stresses exceeds this critical level the failure will occur in the component, this critical level can refer to different failure modes, such as yielding or fracture. For yielding, many different criterias has been developed, the two most common mathematical models are the Von Mises and Tresca. The yield surfaces for Von Mises and Tresca is formulated as:

$$\sigma_{VonMises} = \frac{\sqrt{(\sigma_1 - \sigma_2)^2 + (\sigma_2 - \sigma_3)^2 + (\sigma_1 - \sigma_3)^2}}{2}, \qquad \sigma_{Tresca} = \frac{\sigma_1 - \sigma_3}{2} \tag{12}$$

Where σ_1, σ_2 and σ_3 is the principal stress components. Von Mises is based on critical distortional energy, while Tresca is based on critical shear stress.

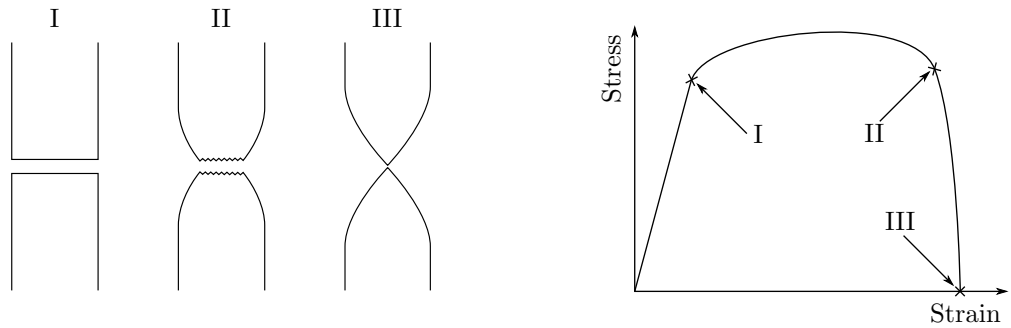

Figure 20: I - Brittle failure, no plasticity. II - Moderatly ductile failure. III - Perfect (100%) plasticity. Left: Illustration of broken specimens. Right: Stress-Strain curve with the different failures indicated.

Different types of failure is shown in Figure 20. Failure occurring without plasticity is characterised as brittle failure, this material behaviour is linear until failure. Failure with some amount of plasticity and then a sudden fracture is characterised as moderately ductile failure. When a material fails from continuous necking and no sudden fracture part, it is characterised as perfect (100%) plastic failure.

Ductile fracture usually happens as a result of formation of voids at inclusions or second phase particles. The void grows around the particle, as the voids grow they will start to interact and coalescing with neighbouring voids. In ductile fracture the fracture surface shows dimples from the void nucleation, shown left in Figure 21.

There are two main types of brittle fracture, cleavage which is crack propagation across grains and intergranular fracture which are fracture along the grain boundaries, both are shown in Figure 21. For brittle materials, or materials assumed to have only elastic behaviour a critical level of SIF is defined as the fracture toughness, K_{IC}. The fracture toughness can

be measured according to the standard: ASTM E1820 - 17a [21], and its often taken to be a material property.

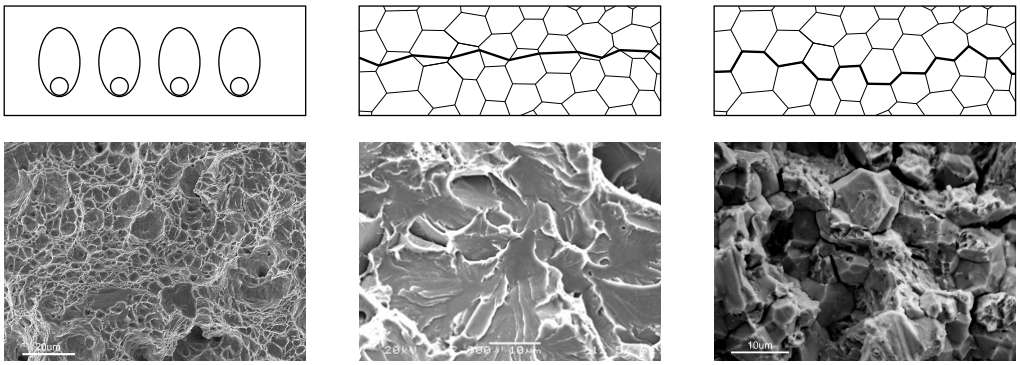

Figure 21: Schematic illustration and SEM of fracture surface. Left: Ductile fracture [22]. Centre: Cleavage fracture [23]. Right: Intergranular fracture [22]

An illustration of crack propagation direction for the different modes in brittle material of loading is shown in Figure 22. If a member is under a combination of the loading modes, the loading is characterised as mixed mode loading. In brittle fracture surfaces it is possible to predict the present loading mode(s) driving the crack propagation, as shown i Figure 22.

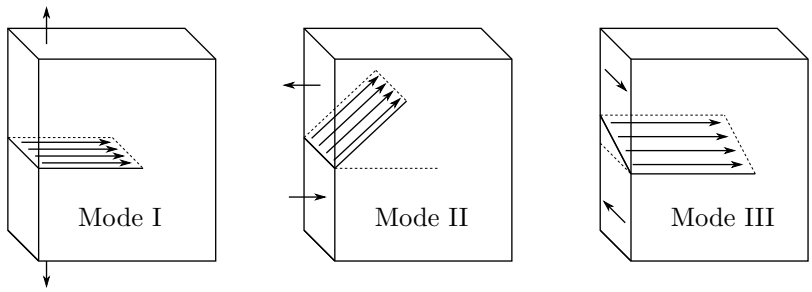

Figure 22: Crack propagation direction under different modes of loading for brittle fracture. Left: Mode I loading. Center: Mode II loading. Right: Mode III loading.

3.6 Fatigue

The following section is based on N. E. Dowling's text book Mechanical Behavior of Materials [16].

80% of all failures in mechanical components are caused by fatigue, it is estimated the annual cost of fatigue failure make up 3% of the gross national product in the United States. Fatigue is generally characterised as damage and failure of material due to cyclic loading below the materials ultimate strength. When a component or material is subjected to cyclic loading, the stresses can cause microscopic damage that is hard to detect, it is therefore convenient to be able to predict the failure.

Different loading can occur in fatigue, in the testing it is common to use sinusoidal, trapezoidal or triangular loading shown in Figure 23. Describing the alternating loads for a

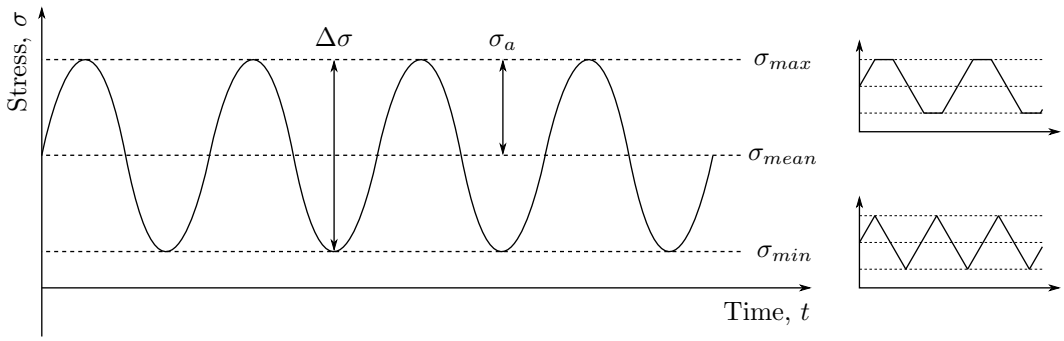

Figure 23: Left:Sinusoidal stress as a function of time. Right: Trapezoidal and triangular loading.

constant amplitude loading is done by defining a maximum stress, σ_{max}, a minimum stress, σ_{min} as shown in Figure 23. The mean stress, σ_{mean}, the stress amplitude, σ_a, the stress range, $\Delta\sigma$, and the loading ratio, R, is then defined as:

$$\sigma_{mean} = \frac{\sigma_{max} + \sigma_{min}}{2}, \quad \Delta\sigma = \sigma_{max} - \sigma_{min}, \quad \sigma_a = \frac{\Delta\sigma}{2}, \quad R = \frac{\sigma_{min}}{\sigma_{max}} \tag{13}$$

There are several different approaches for evaluating fatigue, the three main approaches used in engineering are: Stress-based approach, strain-based approach and fracture mechanics-based approach.

3.6.1 Stress-Based Approach to Fatigue

Stress based approach to fatigue is commonly used for evaluating fatigue life in the high cycle regime with focus on applied stresses. The approach is often based on nominal stress in the critical regions of the components. In this approach to fatigue, the life of the component is often presented in a $S - N$ diagram. In an $S - N$ diagram the stress level is plotted versus the number of cycles to failure, and it is constructed as shown in Figure 24. If the data is plotted in log-log scale, they often display a linear trend that can be described by the Basquin equation: $\sigma_a = AN_f^B$. Some materials have a distinct limit from which under the stress will not cause failure. This limit is often called fatigue limit or endurance limit, this value is often considered a material property. The term fatigue strength used to describe the strength at a given number of cycles, for example the stress amplitude at 2×10^6 cycles.

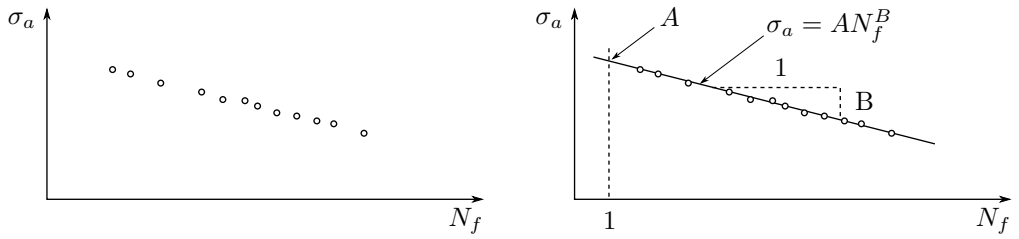

Figure 24: Method of obtaining $S - N$ diagrams. Left: Illustration of fatigue data showing a linear trend in log-log scale. Right: Fatigue data fitted with a Basquin equation.

In the case of notched geometries, the elastic stress concentration factor, k_t, is defined as the ratio between the local maximum static stress and the nominal static stress:

$$k_t = \frac{\sigma_{local}}{\sigma_{nominal}} \tag{14}$$

In fatigue the fatigue notch sensitivity factor, k_f, is defined as a ratio between the fatigue limit for a smooth member and the fatigue strength for a notched member.

$$k_f = \frac{\sigma_{a,notched}}{\sigma_{a,smooth}} \tag{15}$$

The fatigue notch sensitivity is dependent on both material and the notch geometry. In order to estimate it some relations have been developed by R. E. Peterson:

$$q = \frac{K_f - 1}{K_t - 1} = \frac{1}{1 + \frac{\alpha}{\rho}} \Rightarrow \quad K_f = 1 + \frac{K_t - 1}{1 + \frac{\alpha}{\rho}} \tag{16}$$

Where α is a material dependent value that can be estimated based on the expression:

$$\log \alpha = 2.654 \times 10^{-7} \sigma_u^2 - 1.309 \times 10^{-3} \sigma_u + 0.01103 \tag{17}$$

3.6.2 Strain-Based Approach to Fatigue

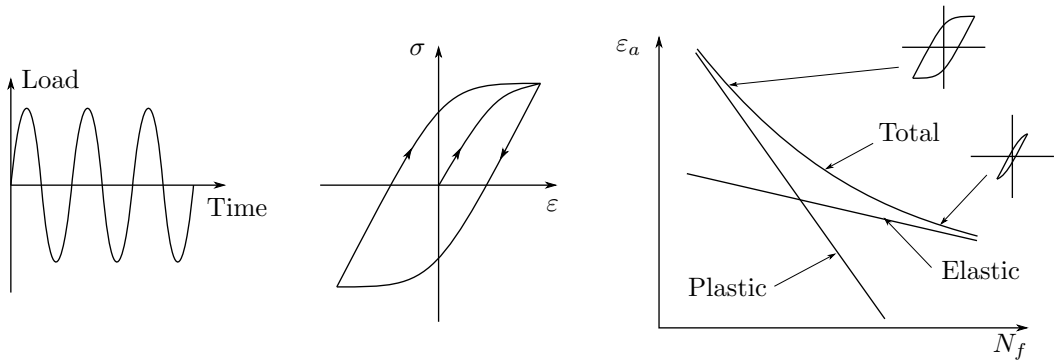

Figure 25: Method of doing strain-based fatigue. Left: Some cyclic load is applied. Middle: Cyclic stress strain relationship, forms a hysteresis loop. Right: Strain amplitude versus number of cycles to failure are combined by an elastic part and a plastic part.

The strain-based approach to fatigue is taking into consideration the plastic deformations occurring during cyclic loading. The method of analysing fatigue data by use of strain-based approach i shown in Figure 25, the load is applied cyclic, resulting in a hysteresis loop (centre), that is cyclic stress-strain behaviour. Then the strain amplitude can be plotted versus number of cycles to failure. The strain amplitude, ε_a, can be divided in an elastic amplitude component, ε_{ea}, and a plastic amplitude component, ε_{pa}:

$$\varepsilon_a = \varepsilon_{ea} + \varepsilon_{pa}, \quad \varepsilon_{ea} = \frac{\sigma_a}{E} = \frac{\sigma'_f}{E}(2N_f)^b, \quad \varepsilon_{pa} = \varepsilon'_f(2N_f)^c \tag{18}$$

The Coffin-Manson relationship can be employed to describe the fatigue behaviour in terms of the elastic and the plastic strain component:

$$\varepsilon_a = \frac{\sigma'_f}{E}(2N_f)^b + \varepsilon'_f(2N_f)^c \tag{19}$$

3.6.3 Fracture Mechanics Approach to Fatigue

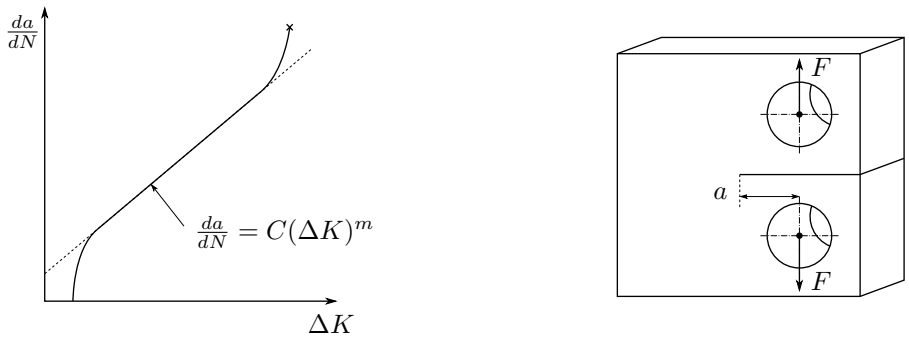

Figure 26: Left: Crack growth rate versus stress intensity range, in log-log coordinates, a linear trend is observed in the curve. Right: Illustration of sample with applied load and crack size a.

Fracture mechanics approach to fatigue is based on considering the crack as it is growing in the member. A common way to use fracture mechanics in fatigue is by using linear elastic fracture mechanics and in particular SIF. In the same way way as defining a stress range, $\Delta\sigma$, as in the stress-based approach to fatigue, the stress intensity range, ΔK, can be defined:

$$K = f\sigma\sqrt{\pi a} \quad \rightarrow \quad \Delta K = f\Delta\sigma\sqrt{\pi a} \tag{20}$$

Where f is a geometric factor. If the crack growth rate, da/dN, is plotted versus stress intensity range, a linear trend shown in log-log coordinates. This relation can be described by Paris law:

$$\frac{da}{dN} = C(\Delta K)^m \tag{21}$$

Where C and m are constants defining the trend line.

3.7 Strain Energy Density

Strain energy is energy stored in the material when it is subjected to deformation, for an elastic material the energy is recovered when the material in unloaded. Strain energy can be expressed as [24]:

$$U = \frac{1}{2}\int_V \sigma_{ij}\varepsilon_{ij}dV \tag{22}$$

SED is defined as strain energy per volume. Critical SED is a failure criterion for tensile stresses which states that failure occurs when the average value of strain energy density, $\bar{W}$, is equal to a critical value of average strain energy density, W_c [25]:

$$\bar{W} = W_c \tag{23}$$

This critical value of SED is dependent on the material. For an ideally brittle material under static loading W_c can be evaluated by using the ultimate tensile strength. The critical value

is then given by $W_c = \sigma_u^2/2E$, where E is the Young's modulus. In the case of fatigue loading the average SED range can be calculated from [26]:

$$\Delta\bar{W} = \frac{e_1}{E}\left(\frac{\Delta K_I^N}{R_0^{1-\lambda_1}}\right)^2 \tag{24}$$

where ΔK_I^N is the NSIF range, E is the Young's modulus, R_0 the radius of the control region (critical radius), and e_1 is given by

$$e_1 = -5.373 \times 10^{-6}(2\alpha)^2 + 6.151 \times 10^{-4}(2\alpha) + 0.1330 \tag{25}$$

The geometry of the control area with the critical radius is shown in Figure 27. For a sharp crack or notch the control area is placed with its centre at the tip of the crack of notch, while in the case of a blunt notch the radius of the control volume is given by $R_1 = r_0 + R_0$, and the edge of the control area is placed a distance R_0 from the notch tip, along the notch bisector line. The coordinate system used for determining the position of the control volume is based on the same coordinate system used for the elastic stress field described in Section 3.4.5 for the unified elastic stress field for different notch geometries by P. Lazzarin and R. Tovo [20].

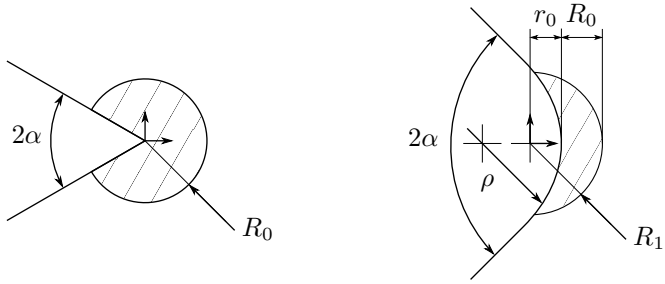

Figure 27: Control volume used for Strain Energy Density. Left: For sharp notch. Right: For blunt notch.

The critical radius, R_0, used for the control region for static loading is given by [25]:

$$R_0 = \frac{(1+\nu)(5-8\nu)}{4\pi}\left(\frac{K_{IC}}{\sigma_t}\right)^2 \tag{26}$$

In the case of fatigue another formulation for predicting the critical radius is used [27]:

$$R_0 = \left(\frac{\Delta K_{IC}^N}{f_1(2\alpha)\Delta\sigma_A^S}\right)^{\frac{1}{(1-\lambda_1)}} \tag{27}$$

Where ΔK_{IC}^N is the stress intensity range at the fatigue limit for the notched geometry, $\Delta\sigma_A^S$ is the fatigue limit for a smooth specimen of the same material and $f_1(2\alpha)$ is function dependent on the opening angle of the notch given by:

$$f_1 = 4.897 \cdot 10^{-5} \cdot (2\alpha)^2 - 5.598 \cdot 10^{-3} \cdot (2\alpha) + 1.959 \tag{28}$$

The value of R_0 for fatigue can be found by referring to the fatigue limits for a smooth and a notched sample, the same average SED should be found for the smooth sample and for the

notched sample using the critical radius for the control volume when evaluating the value at the fatigue limit [25]:

$$\Delta \bar{W}_c^{Smooth} = \frac{(\Delta \sigma_A^{Smooth})^2}{2E} = \Delta \bar{W}_c^{Notched}(R_0) \tag{29}$$

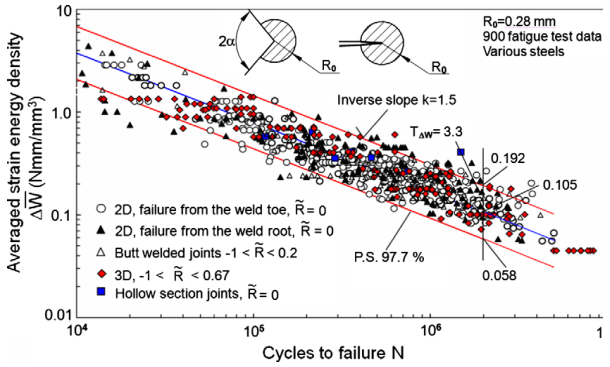

Figure 28: Strain energy density used to analyse fatigue data of welded joints [25]. 900 fatigue test results for various steels and weld geometries.

Numerous works has been done on SED of different notch geometries, in 2009 F. Berto and P. Lazzarin [25] made a review of SED approach to v-shaped and welded structures. The paper considers a large bulk of experimental data obtained from static and fatigue tests of notched components and welded joints. The data er analysed by use of SED in FEA and is presenting the fatigue data in one unifying avg. critical SED versus number of cycles to failure, a $\Delta \bar{W} - N$ curve. The results of 900 fatigue data analysed by SED are shown in Figure 28.

Table 1: Number of elements in control volume and avg. SED in FE-model of weld geometry [28].

Number of elements	1696	768	324	96	24	4
Avg. SED ($\bar{W}$)	0.07937	0.07903	0.07896	0.07895	0.07790	0.07594

One of the main advantages of using SED for failure prediction in members is that the FEA calculations are not mesh sensitive, and a coarse mesh can be used. For predicting failure based on stresses the FEA models are strongly dependent of the mesh. Mesh sensitivity for SED calculations in FE was demonstrated by Lazzarin et al. [28] in 2007. The results are shown in Table 1, the difference in the results for SED between the finest and the coarsest mesh is less than 5%.

4 Superalloys

In this section superalloys and in particular Inconel 718 (IN718) is presented. First an introduction to superalloys is given. Then IN718 is introduced, followed by a literature review of both conventional IN718 and AM IN718. The conditions for testing, post processing and results are briefly described.

Engineers are constantly searching for better materials, stronger, lighter, more corrosion resistant, functioning under more extreme conditions. Stainless steel was developed in the second and third decades of the 20th century and was a starting point for corrosive resistant material for high temperature applications. Stainless steel was found limited in strength, and because of this "superalloys" was developed [1].

Superalloys are Ni-, Fe-Ni-, Co-based alloys with high mechanical properties at up to 70% of the melting temperature [29]. A large number of superalloys has been developed and studied during the years, many of them are patented and used by industries. In crystal structure superalloys, Fe, Co and Ni are usually face-centre-cubic (FCC)-austenitic [1].

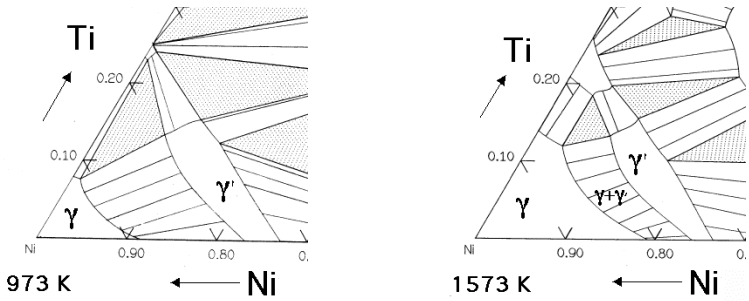

Figure 29: Phase diagram for Ni-Ti-Al at left: 973 K (700°C) and right: 1573 K (1300°C)

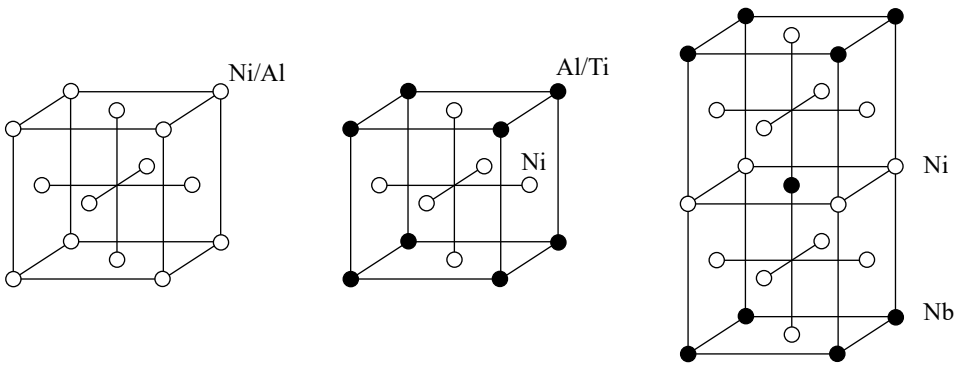

Figure 30: Crystal structure of γ, γ' and γ'' [29]

The essential solutes in superalloys are Ti and Al, the concentration of these alloying elements are usually less than 10 percent. The combination of Ni, Ti and Al generates a two-phase equilibrium microstructure of gamma (γ) and gamma prime (γ') phase, the Ni-Ti-Al phase diagram is shown in Figure 29. The phase diagram in Figure 29 shows that, for a given composition, when the temperature increase the fraction of γ' decreases. This result is

used to generate a uniform distribution of γ' strengthening precipitates in the material by dissolving γ' at high temperature (solution treatment), and then ageing the material at lower temperature. The crystal structures for γ and γ' is shown in Figure 30, both are FCC in crustal structure. γ'-phase has a FCC structure with Ni at the faces, and Al or Ti at the corners. The chemical formula is Ni3Al, Ni3Ti or Ni3(Al,Ti). The γ' is a precipitate in the γ matrix in a cube-cube orientation because of the similar lattice structure. Because of the orientation of the γ and γ', it is difficult for the γ dislocations to penetrate γ'. This is one of the mechanisms contributing to strengthening the superalloys [29]. When high strength is also required at lower temperatures the gamma double prime (γ'')-phase can be used, this phase is present in IN718. The γ''-phase is body-centred tetragonal with Ni and Nb (for IN718) or V atoms. The crystal structures of γ'' is shown in Figure 30.

Heat treatment (HT) is performed on superalloys in order increase the material properties. Some of the most common HT performed on superalloys are [1]:

Stress relieving Removing the residual stresses in a material without effecting the corrosion resistance and high-temperature properties.

Annealing Full recrystallization and achieving maximum softness of the material (reduce hardness and increase ductility).

Solution treatment In many cases the same treatments as annealing, but has a different purpose. Solution treatment has the purpose of dissolve second phases for reprecipitation/aging and increase corrosion resistance.

Precipitation/age hardening Heat treatment done in order to achieve desirable strengthening precipitates in the material and control other secondary phases. Typically the material is heat treated at in several stages, with controlled cooling between.

4.1 Inconel 718

One of the most popular superalloys is the Ni-based IN718. It is a continuation of stainless steel technology, with a similar composition in terms of alloying elements, but a higher amount of Ni [1]. The nominal composition of IN718 is shown in Table 2.

Table 2: Nominal composition in IN718 of alloying elements in percent [1]

C	Ni	Cr	Mo	Fe	Al	Ti	Cu	Nb
0.04	53	19	3	18	0.5	0.9	0.1	5

Other phases present in IN718 than γ, γ' and γ'' is the Laves (Ni,Cr,Fe)3(Nb,Ti,Mo) - topological close packed, MC carbides (Nb, Ti)C and δ with an orthohombic crystalstructure and with a Ni3Nb composition [30][31]. In order to obtain the the precipitate strengthening phases in IN718 post processing is done. Fully Ageing (FA) of the material is usually done by solution treating and ageing as described [1]:

- Solution treatment at 980° for 1 hour, air cool (AC) to room temperature (RT).
- Double ageing which involves heating the material to a 720° and keep for 8 hour, then furnace cool to 620° and keep for 8 hour, then AC to RT.

IN the case of AM, IN718 can be produced by both SLM and EBM [3]. One problem concerning structural integrity of AM components is porosities inside the material, from manufacturing process. Porosities can be reduced by Hot Isostaic Pressure (HIP) the components. In HIP components are subjected to hot isostatic pressure in a controlled gas atmosphere, for a certain amount of time. When removing or reducing the porosities mechanical properties such as hardness, and strength can be increased, but due to the temperature the properties can also be decreased [31][2].

4.2 Literature Review of Conventional Inconel 718

In this section a literature review on conventional manufactured IN718 is presented, the focus is put on tensile and fatigue properties.

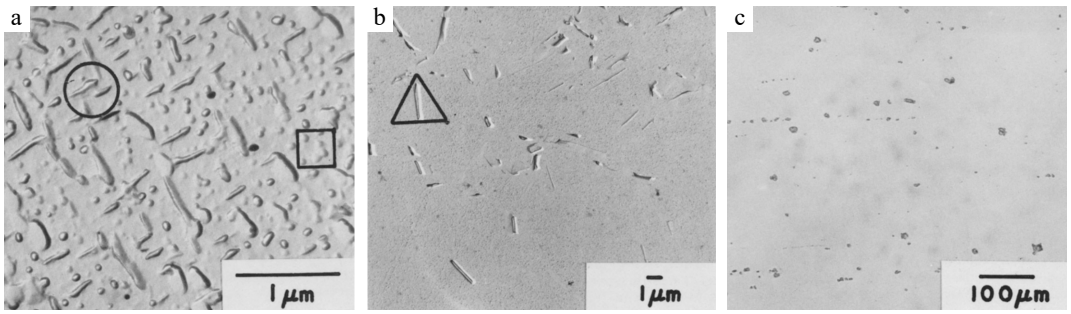

Figure 31: Microstructure of IN-718 reported by Stout and Gerberich [32]. a) γ'', γ', b) δ, c) TiN, NbC

Table 3: Static mechanical properties, yield strength, tensile strength and fracture toughness for material obtained by Stout and Gerberich [32]

Heat Treatment	σ_y [MPA]	σ_u [MPa]	K_{IC} [MPa$\sqrt{m}$]
FA	1190	1540	75
FA + 648°C (100 h)	1230	1560	76
FA + 760°C (100 h)	950	1440	81
FA + 842°C (16 h)	800	1320	126
FA + 876°C (16 h)	640	1170	130

Ductile fracture behaviour of IN718 with five different heat treatments has been studied by Stout and Gerberich [32]. The following heat treatment were done to fully age the material: 945°C (1h) $\rightarrow$ AC to RT $\rightarrow$ 760°C (8h) $\rightarrow$ FC (56°C/h) to 648 (10h) $\rightarrow$ AC to RT. After fully ageing, the samples were kept at a constant temperature for a certain amount of time, as described in Table 3. Figure 31 shows the microstructure of FA IN718, the open circle shows γ'' precipitations, in the open box the γ' precipitations are shown and in the triangle a δ (laves)-phase is shown. Fracture toughness of the different heat treated samples was found by using a J-integral technique. The samples used was fatigue pre-cracked compact tension geometries. Some of the results obtained is shown in Table 3. The fracture process were examined from the crack profiles and the surfaces of the cracked samples, from this it was found that the fracture initiated from carbides by formation of delamination. The delaminations formed by two different methods, in the microstructure with low yield strength it formed by mode I void nucleation and growth, in the microstructues with high yield strength it formed by mode II.

Table 4: Static mechanical properties for material used for high temperature fatigue by Kawagoishi et al.[33].

Temperature [°C]	Yield Strength [MPA]	Tensile Strength [MPa]
RT	1320	1460
300	1130	1340
500	1050	1250
600	1020	1230

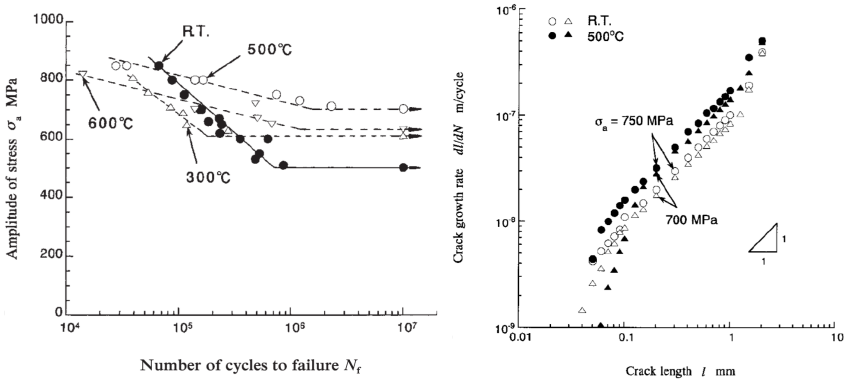

Figure 32: Fatigue data obtained by Kawagoishi et al.[33]. Left: S-N curve for different temperatures, Right: Crack growth behaviour for room temperature and 500°C.

Fatigue properties of IN718 at elevated temperatures under rotary bending has been investigated by Kawagoishi et al.[33]. The material used was heat treated by: 982°C (1h) → quenched in water → RT → 720°C (8h) → FC to 621°C (8h) → AC to RT. The samples used for testing were electro-polished round hourglass shaped, with a radius of 4 mm in the gauge section. The samples were tested at 300°C, 500°C, 600°C and at RT, with loading ratio of R = - 1 at a frequency of 55 Hz. Some of the results found are shown in Figure 32 and Table 4, they are showing that fatigue strength is increased for higher temperatures, while the static strength properties decreases for high temperatures. A partial notch was included in the samples for studying crack growth behaviour at both room temperature and at 500°C, shown right in Figure 32. The results shows that the crack growth rate is increased at higher temperature.

Notched fatigue strength under rotary bending loading of IN718 at 500°C and at room temperature has been studied by Chen et al. [34]. The material (heat treatment), test procedure and geometry of the smooth specimens used is the same as described by Kawagoishi et al. [33] previous in this section. The notched samples has a blunt v-shaped notch with an opening angle of 60° and a notch radius of 0.05mm. The effect of temperature on the fatigue strength and on the notch sensitivity was examined and the results are shown left in Figure 33. The results shows a higher notch sensitivity at higher temperatures. For different notch geometries, the samples are examined in optical microscope in order to detect non propagating cracks. Linear elastic notch mechanics is employed in order to evaluate the fatigue limit for crack initiation, σ_{w1}, and the fatigue limit for crack propagation, σ_{w2}. σ_{w1} and σ_{w2} are plotted versus the stress concentration factor right in Figure 33, and shows that under a given stress crack are initiating, but not propagating.

Low cycle fatigue behaviour of heat treated IN718 at room temperature and at 550°C has

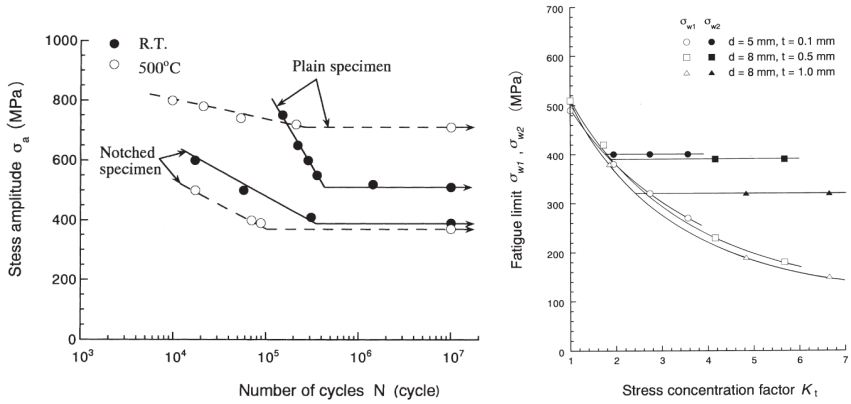

Figure 33: Fatigue data obtained by Chen et al. [34]. Left: S-N curve for notched and smooth samples are room temperature and at 500°C. Right: Fatigue limit for crack initiation and propagation versus stress concentration factor.

Table 5: Static mechanical properties for material used for high temperature fatigue by D. Fournier and A. Pineau [35]

Temperature [°C]	Yield Strength [MPA]	Tensile Strength [MPa]
RT	1100	1350
500	1000	1200

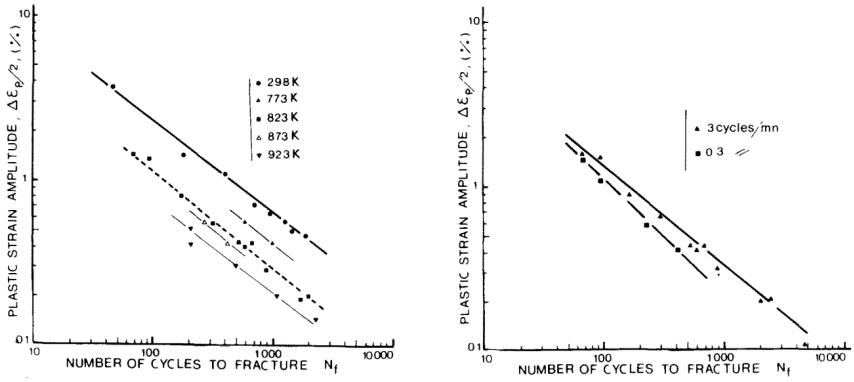

Figure 34: Plastic strain amplitude versus number of cycles to failure for: Left: Different temperatures, Right: Different strain rates at 550°C (823K)[35]

been studied by Fournier and Pineau [35]. The stress-strain behaviour under fully reversed strain controlled loading was studied, and optical and electron microscopy were used to study crack behaviour during loading. Material used was hot forged and fully aged by the following heat treatment: 955°C (1h) → AC to RT → 720°C (8h) → FC to 620°C (8h) → AC to RT. The samples used for where hour glass shaped with a diameter of 5mm in the gauge section. For the high temperature fatigue, the heating was performed by induction. The static mechanical properties are shown in Table 5. From an obtained hysteresis loop, the strain was divided into plastic and elastic components. Some results from the fatigue tests are shown in Figure 34. Left in Figure 34, the effect of temperature in the plastic strain amplitude is shown, the data shows that the material fails from a lower plastic strain

amplitude when the temperature is increased. Right in Figure 34, the effect of loading frequency is shown for 550°C, decreasing the loading frequency gives shorter life for the same plastic strain amplitude.

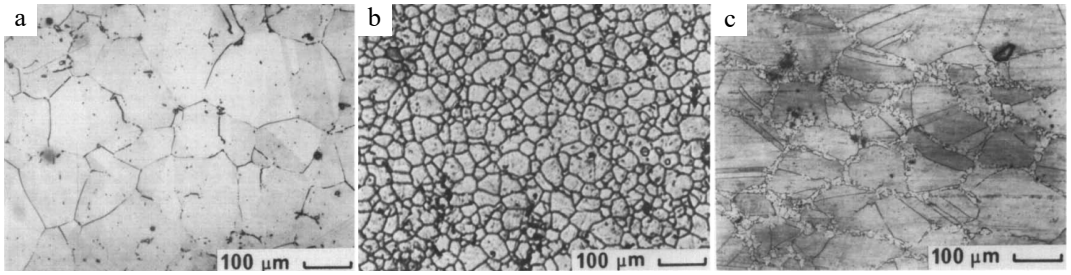

Figure 35: a: coarse grained microstructure, b: fine grained microstructure, c: necklace microstructure.

Table 6: Static mechanical properties for material used for high temperature fatigue by Pedron and Pineau [36]

Structure	T [°C]	σ_y [MPA]	σ_u [MPa]	Tensile ductility [%]
Necklace	25	1240	1350	18
	650	1000	1080	17
Coarse	25	1145	1290	24
	650	885	960	17
Fine	25	1245	1415	24
	650	990	1130	19

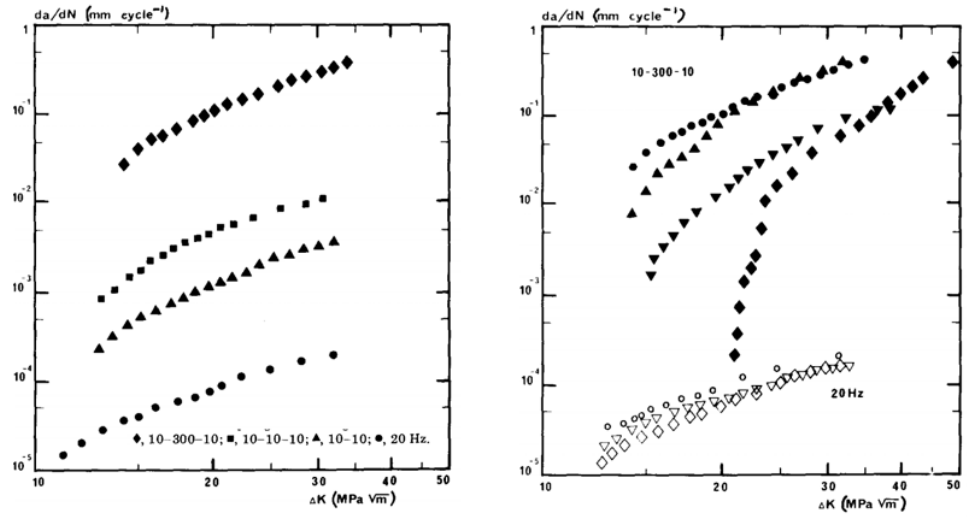

Figure 36: Left: Fatigue crack growth for fine grains, for different loading methods. Right: Fatigue crack growth for the different microstructures for different loading methods. ○ - fine grained, ◇ - necklace, △,▽ - coarse grained (two different orientations)

The effect of environment and microstructure on fatigue and creep loading in IN718 has

been studied by Pedron and Pineau [36]. Different microstructures has been developed and tested in a temperature of 650°C. For fatigue the effect of loading frequency was also studied in the range of 20Hz to 0.05 Hz. By use of thermomechanical treatment three different microstructure was obtained, one coarse, one fine and on necklace microstructure, the different microstructures are shown in Figure 35. The different microstructures are obtained by different procedures of rolling and heat treatment. The coarse microstructure consist of equiaxed grains, with a size about 200μm. From transmission electron microscopy the grain boundaries were found clean, with some platelets of β phase orthorhombic phase precipitates occasionally, the disk-shaped γ'' hardening particles had an average diameter of 16 nm. For the fine grained microstructure the grain boundaries were found to be free of β participates, the disk-shaped γ'' hardening particles had an average diameter of 20 nm. For the necklace microstructure percipites of the β phase were found at the grain boundaries, surrounding these percipitates impoverishment of γ'' particles were found. The disk-shaped γ'' hardening particles had an average diameter of 21nm. The mechanical properties from the static tests in room temperature and at elevated temperature are shown in Table 6. The fine grained microstruture gives the highest values of tensile strength both at room and elevated temperature. The fatigue crack growth at 650° for the different microstructures were checked for different loading methods, sinusoidal loading with 20 Hz, triangular with 0.05 Hz (10-10) and trapezodial with loading and unloading times of 10 s, and hold time of 300 s (10-300-10). The results for different loading methods are shown left in Figure 36 for fine grain, and it shows that the highest crack growth rate is found for the 10-300-10 loading method, while the lowest crack growth rate was found for sinusodial loading. The crack growth rate for different microstructures is shown right in Figure 36. It shows less dependency for sinusodial loading, while for the 10-300-10 method the crack growth rate is fastest for the fine grain, and slowest for the necklace microstructure.

Concluding remarks conventional manufactured IN718:

- Fatigue life and mechanical properties in general is increased by heat treating the material.
- Mechanical properties is decreased by loading in higher temperatures.
- Fatigue life is decreased by introducing notches.
- Fatigue life is decreased by increasing high temperature.
- Notch sensitivity is increased by increasing temperature.
- Crack growth rate is increased by increasing temperature.
- Crack growth rate is dependent on loading strategy, sinusoidal versus trapezoidal gives different crack propagation properties.
- Microstructure obtained from heat treatment is influencing the crack propagation properties for different loading strategies.
- Combined creep fatigue loading gives higher crack growth rate than pure fatigue loading.

4.3 Literature Review of Additively Manufactured Inconel 718

In this section a small selection of journal papers done on mechanical properties of AM IN718 is presented. This include tensile and fatigue properties for different process methods,

printing strategies and heat treatments. Different printing directions according to ASTM [37] for different tensile test samples are shown in Figure 37.

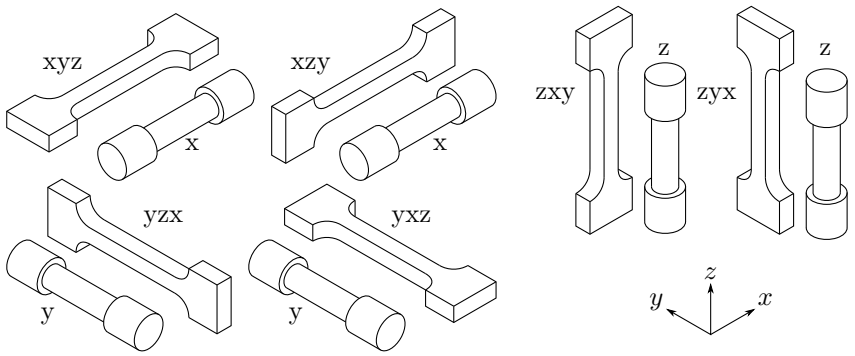

Figure 37: Printing direction of samples

J. J. Lewandowski et al. has reviewed mechanical properties of AM metals, in which some IN718 results are presented [38]. The reported results are shown in Table 7, and shows different mechanical properties for different processing methods, printing directions and heat treatments. The data shows variation in properties for different machine types, however, the mechanical properties are increased by heat treating.

Table 7: Mechanical properties for additive manufactured IN718 reported in literature by J. J. Lewandowski et al. [38]

Machine type	Condition	Ori	E [GPa]	σ_y [MPa]	σ_u [MPa]	Elongation [%]	
EOS M280	Heat treated	Z	NA	1034	1309	27	[39]
		XY		1068	1344	27	
SLM	As built	XY	NA	816±24	1085±11	19.1±0.7	[40]
		Z		737±4	1010±10	20.6±2.1	
	Heat treated	XY		1227±1	1447±10	101±0.6	
		Z		1136±16	1357±5	13.6±0.2	
Arcam S12	As built	Z	NA	410	750	44	[41]
	HIP			330	770	69	
SMD	As built	XY	NA	473±6	828±8	28±2	[42]
DLD	As built	Z	NA	650	1000	NA	[43]
	Heat treated			1257	1436		
Laser	As built	NA	NA	590	845	11	[44]
	Heat treated			1133	1240	9	
EBF3	As built	XY	159	580	910	22	189
EBF3	As built	XY	138	655	978	NA	99
		YX	194	699	936		
	Heat treated	XY	174	986	1114		
		YX	192	998	1162		
DLD	Heat treated	NA	NA	1097	1321	9.8	111
DLD	Heat treated	NA	NA	1034	1276	12	190
Laser/wire	Heat treated	NA	NA	1079	1314	20.4	191

Microstructure and mechanical behaviour of SLM IN718 has been studied by K. N. Amato et al. [31]. The samples was build in z and x-direction, in both nitrogen and argon gas, and mechanical properties tested in both directions as printed and heat treated with hot isostatic pressure (HIP). The powder used for building the test specimens are shown in Figure 38a, the average powder size is 17 μm. A cross section of the powder used is shown in Figure 38b, internal microdendritic structure is visible. Figure 39 shows an 3D optical metallograph

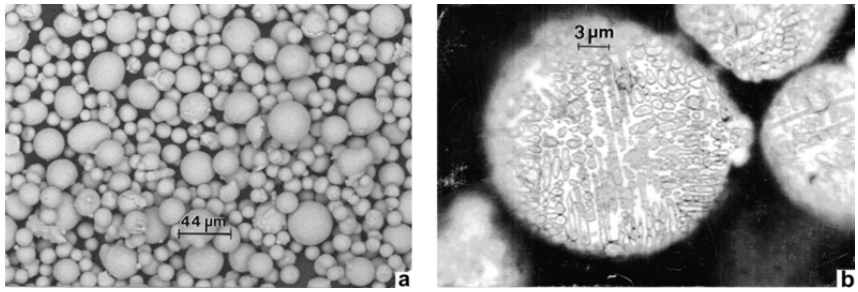

Figure 38: a) Pre-alloyed powder in scanning electron microscope. b) Cross section of etched powder in optical microscope.[31]

composite image of the microstructure and grains in the specimen built in x-direction in argon gas, for both as-build and heat treated material. The as-build materials displays a microstructure with irregular columnar architecture with dimensions between 0.5 and 1 μm. The heat treated material shows a more regular columnar architecture. The mechanical properties for the different build directions, process parameters and post treatments are shown in Table 8. Producing in argon and nitrogen-atmospehere gives similar mechanial properties, the yield strength of the material build in nitrogen is higher than for the one built in argon.

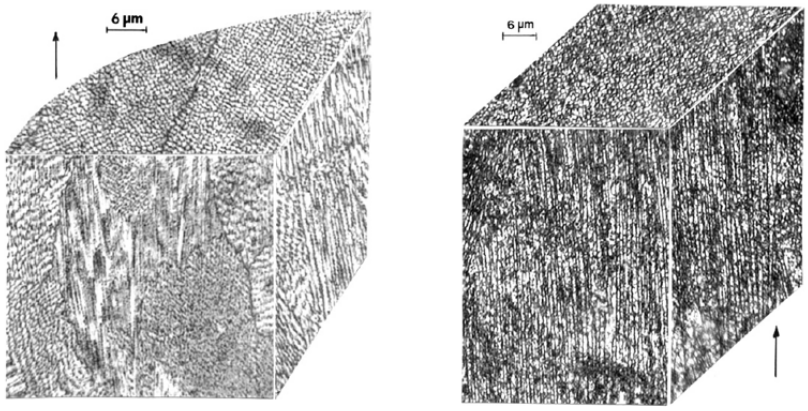

Figure 39: 3D optical metallograph composite showing the microstructure and grains for of as build material (left) and heat treated material(right), both in argon gas. The build direction is indicated by the arrows. [31]

Mechanical properties of different techniques of AM IN-718 is correlated with the microstructure for different post process methods by B. Farber et al.[30]. Four different post treatments conditions are considered: annealing + double againg (HT), HT + Hot isostativ pressure (HIP), HT + shoot peening (SP) and HT + HIP + shoot peening (SP). The mechanical

Table 8: Static mechanical properties for material used for high temperature fatigue by Amato et al. [31]

Orientation	Argon			Nitrogen		
	σ_y [MPa]	σ_u [MPa]	EL [%]	σ_y [MPa]	σ_u [MPa]	EL [%]
z - As build				830	1120	25
x - HIP + Annealed	850	1140	28	880	1140	30
z - HIP + Annealed	890	1200	28	930	1200	27

properties obtained is shown in Table 9, HT showed highest hardness and mechanical properties, while HT + HIP showed the same elongation and tensile properties as HT but lower hardness and yields strength. The difference in yield strength between HT and HIP+HT was found to be cause by δ precipitates within the grains in the HT material, while the HIP + HT material had larger grains without δ precipitates. SEM of etched HT material is shown in Figure 40. In Figure 40a an array of needle shaped δ-phase is visible, the γ' and γ'-phases are also visible.

Table 9: Mechanical properties of IN718 for different post processing methods reported by B. Farber et al. [30]

	E [GPa]	σ_y [MPa]	σ_u [MPa]	EL [%]
HT	188	1170	1380	9
HIP+HT	210	1090	1310	8.2
HT+SP	196	1110	1340	4.3
HIP+HT+SP	220	1080	1350	7.5
Wrought	208	1098	1250	16.5
Cast	198	694	920	8

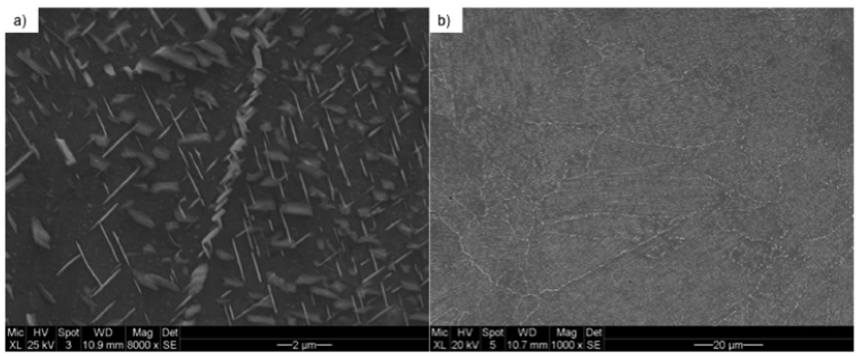

Figure 40: SEM image of etched HT material displaying δ and Laves-phases a) longitudinal direction b) transverse direction

The effect of texture and anisotropy on low cycle fatigue properties for IN-718 produced by electron beam melting has been studied by M. M. Kirka [45]. The samples were post processed with HIP and HT. The fatigue properties in both parallel and perpendicular direction to the build direction were tested and compared to wrought samples under fully reversed strain controlled loading at 650^oC. The additive manufactured HIP and HT had

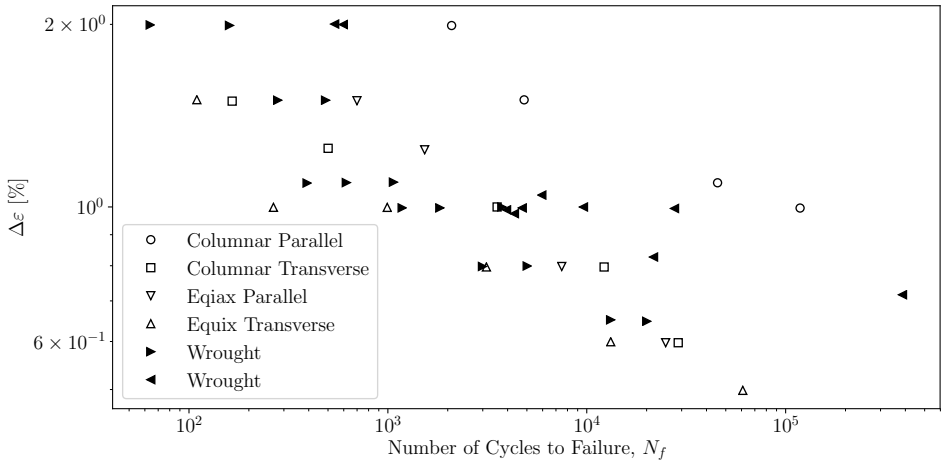

Figure 41: Low cyle fatiue for different microstructures and directions by M. M. Krika et al. [45]

similar or longer fatigue life than the wrought samples in all cases. On average the samples with columnar grains in parallel to the build directions showed higher fatigue life compared to the samples with grain orientation transverse to the build direction and equiaxed grained samples. In the case of columnar grains parallel to the build direction, the cracks propagated intergrannually, and initiated from the surface. In the case of grains in the direction transverse to the build direction the crack propagated transgranually. The fatigue results for the different microstructures and directions are shown in Figure 41, and are compared to wrought material. Columnar grains tested parallel to the grain direction displayed the longest fatigue life for a given strain range.

Mechanical properties of AM IN718 produced by SLM at room temperature and at 650^{o}C for different build directions has been investigated by F. Caiazzo et al. [46]. Support structures has been used for downward facing surfaces (overhang surfaces) dependent on the angles. Heat treatment has been performed on the specimens before removing them from the building plate. The specimens has been subjected to Solution treating and double ageing in argon atmosphere (according to AMS 5664 standard). The results from the tests are shown in Table 10, and shows highest mechanical properties for 45° building angle for at room temperature and at 650^{o}C.

Table 10: Yield and ultimate tensile strength for different printing angles and temperatures [46].

Sample	T [^{o}C]	σ_y [MPa]	σ_u [MPa]
EOS Reference [47]	24	1239	1384
Flat build		1295	1484
45^o-build	24	1368	1521
Upright-built		1240	1398
Flat build		1033	1139
45^o-build	650	1124	1187
Upright-built		978	1114

Microstructure, Fatigue behaviour, and Failure Mechanisms of Direct Laser-Deposited Inconel 718 has been investigated by A. Johnson et al. [48]. The samples was produced by Laser Engineered Net Shaping (LENS), heat treated and machined. The following heat treatment was done: 940°(2h) AC to RT → 718°C (8h) → FC (50°C/h) to 612°C (8h) → AC to RT. Fatigue test were done on machined cylindrical hourglass shaped specimens using fully reversed strain controlled loading. The as-built parts showed dendritic structure and elongated grains in the building direction. The samples were built from a substrate one sample at the time, in the region close to the substrate lack of fusion defects were found, while spherical pores were found away from the substrate. The heat treated grain structure were smaller and more uniform than the as-built. The fatigue data for the AM and wrought samples is shown in Figure 42, where strain amplitude is plotted versus number of cycles to failure. The fatigue life of the AM samples was shown to have a comparable fatigue life to the wrought in the short fatigue life regime, while in the high cycle fatigue regime the AM samples showed a shorter fatigue life. The cracks initiated at hard particles and pores at or in the region close to the surface.

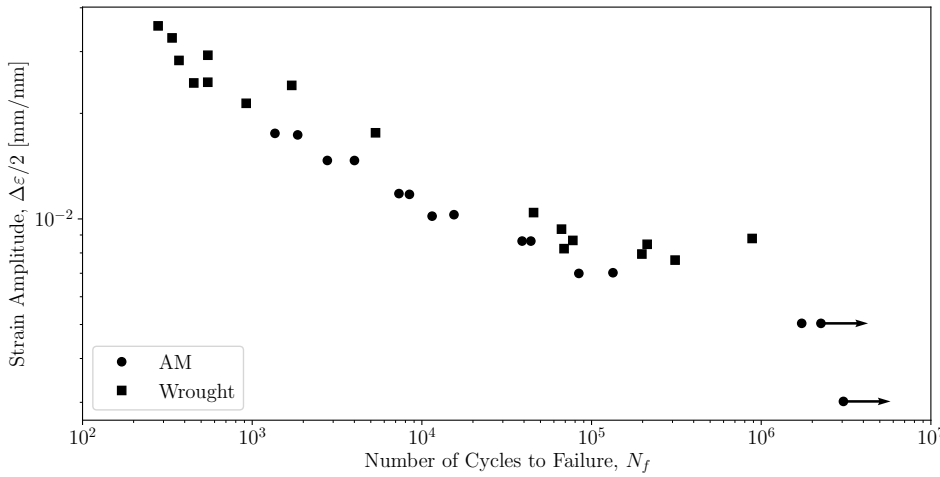

Figure 42: Low cycle fatigue for AM and wrought IN718 reported by A. Johnson et al. [48]

The effect of different post processing methods on fatigue behaviour of AM IN718 has been studied by D. Wells [49]. The specimens was given the same heat treatment, then different surface treatments. The following heat treatment was done to the specimens: Stress relief 1065°C (1.5h) FC, HIP 1165°C 100 MPa (3-4h), Solution 1066°C (1h) → AC to RT → aging 760°C (10h) → FC to 650°C (20h). The microstructure of the as-built and post processed microstructure and the different surfaces are shown in Figure 43. The build direction is clearly visible in the as-built material. Fatigue behaviour AM IN718 with different surface treatments is shown in Figure 44, the data shows a large increase in fatigue life when machining the surface, and a small effect for the other methods. This could indicate that there is surface defects such as lack of fusion in the samples, removing the outer layer of the surface will increase the fatigue life, while tumbling the samples will not necessarily remove the defects, only make the surface smoother.

Yadollahi et al. [50] has made an overview of fatigue behaviour of different AM metals, including IN718. Figure 45 shows a comparison between wrought and AM IN718 under fully reversed cyclic loading (R = -1) in room temperature. Both samples are machined, and has

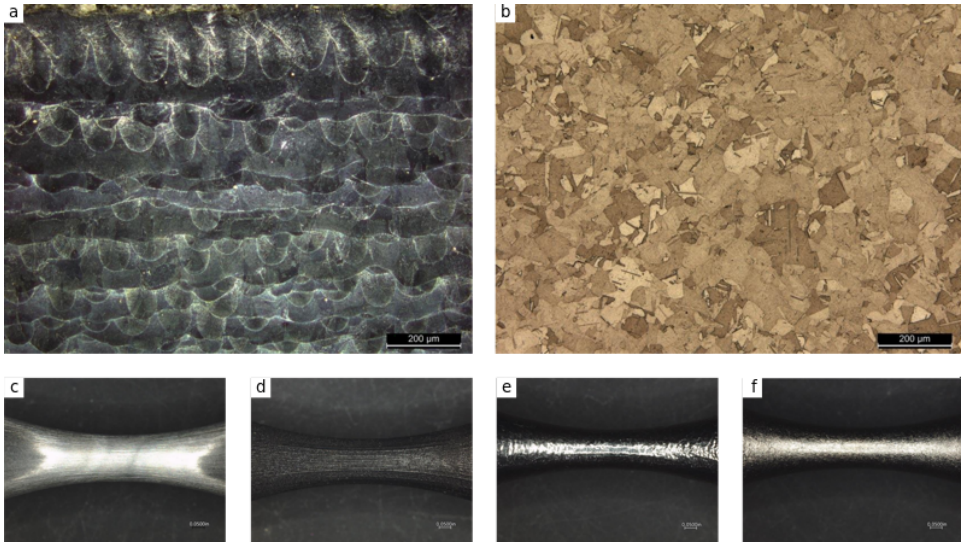

Figure 43: Microstructure of AM IN718: a) as build material; b) Heat treated material. Different surface treatments: c) Low stress ground; d) As-built; e) Tumbled and electropolished; f) Tumbled and chemical milling

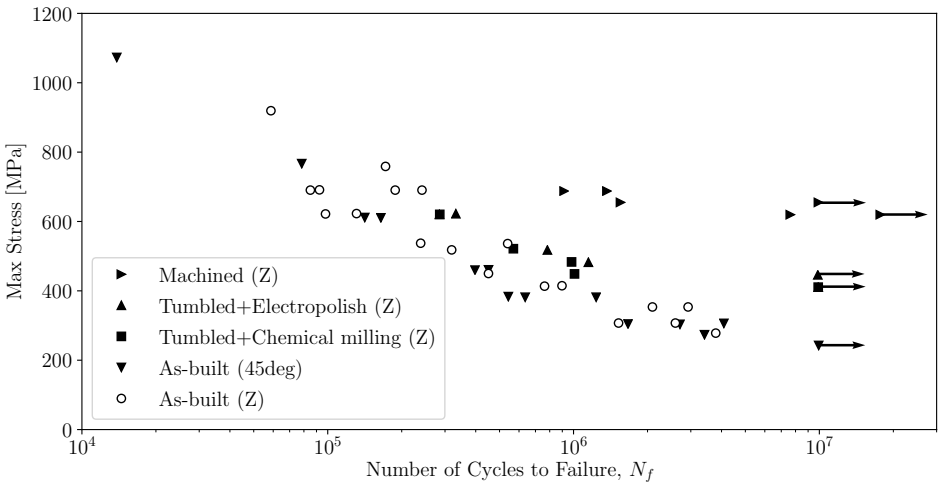

Figure 44: Fatigue data obtained by D. Wells [49] for different surface treatments of post processed IN718. Loading ratio R = 0.1.

undergone the same post treatments, HIP and conventional heat treatment for IN718. The fatigue limit of the wrought material are higher than the AM material. Fractography done by SEM shows that the cracks are initiating from lack of fusion defects in the surface region. This can indicate that the specimens was machined before HIPing, as the defect was not closed by HIPing.

Concluding remarks on literature review of AM IN718:

- Mechanical properties, both static and fatigue, is increased by heat treatment

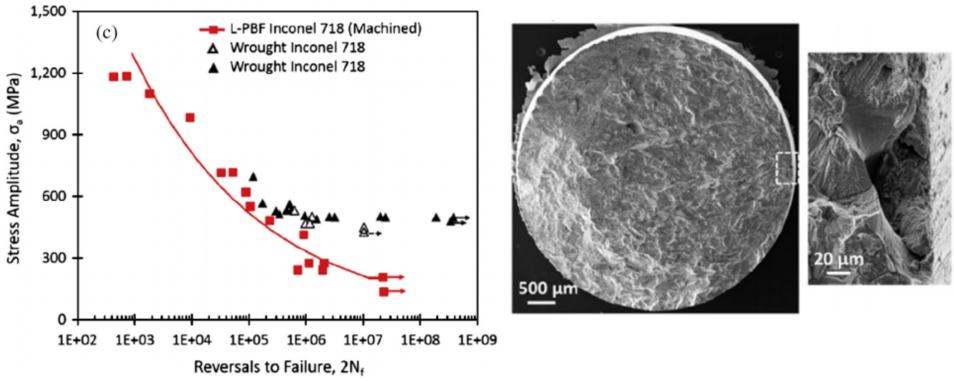

Figure 45: Left: difference in fatigue behaviour of worught and AM IN718. Right: Fractography of AM sample, fatigue initiating from lack of fusion area [50].

- AM components contains defects such as lack of fusion and porosities, fatigue is initiating from these places.
- Static mechanical properties gives different values of printing direction (samples angle relative to build direction)
- Surface treatments can increase fatigue life, machining is more efficient than tumbling/polishing. Probably due to removing material more likely to contain defects close to surface.
- In general, the fatigue life is better for conventional IN718 than AM.
- Different AM processes gives different mechanical properties, not enough data has been published to state the trends for each process.

5 Testing

In this section the test specimens and method used for testing is described.

5.1 Test Geometries

In order to evaluate the notched fatigue behaviour of AM IN718, four different specimen geometries will be analysed in this work. The geometries are shown in 46, from left, the first one is an unnotched specimen, used as reference for the notched geometries. The second one is a semi-circular notch, the two last geometries are both v-shaped notches, the first one with a notch radius $\rho = 1$ mm, and the second one with a notch radius of $\rho = 0.1$ mm. The dimensions of the specimens are shown in Table 11.

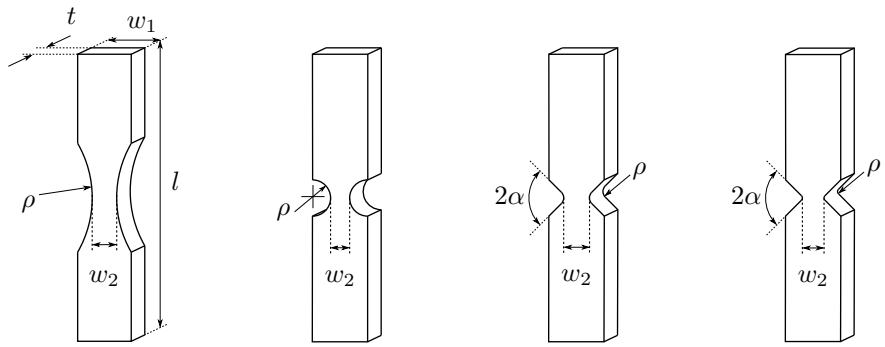

Figure 46: Geometry of test specimen. From left: Unnotched, Semi-circular notch, v-shaped with with notch radius of 1 mm and v-shaped with with notch radius of 0.1 mm

Table 11: Dimensions of test specimens

Geometry	t [mm]	w_1 [mm]	w_2 [mm]	l [mm]	ρ [mm]	2α [°]
Unnotched	5	15	7	80	30.31	-
Semi-circular notch	5	15	5	80	5.000	-
V-shaped notch $\rho = 1$	5	15	5	80	1.000	90
V-shaped notch $\rho = 0.1$	5	15	5	80	0.100	90

5.2 Test Specimens

The four different notch geometries where ordered from FIT Additive Manufacturing Group in Germany with the following specification:

- Material: Inconel 718
- Untreated without any finish work
- The parts is built up solidly
- Part will be build in 50 μm layer size

- Printing direction: Z
- laser melting of metal powder (SLM)

Figure 47: Picture of additively manufactured IN-718 samples used for testing. From left: Unnotched, semi-circular, v-notch $\rho = 0.1$ mm and v-notch $\rho = 1$ mm. Build direction is indicated by the arrow.

A picture of the specimens and the build direction is shown in Figure 47. The specimens displays a rough surface with horizontal lines referring to the layer-by-layer manner of producing the specimens. The contouring and hatching strategy used is visible from the top surface of the specimens and shown in 48, in the left optical microscopy taken on Olympus BX53M is shown, and right an illustration of the strategy. Optical microscopy shows that the thickness of the contouring has an approximate thickness of 200 μm.

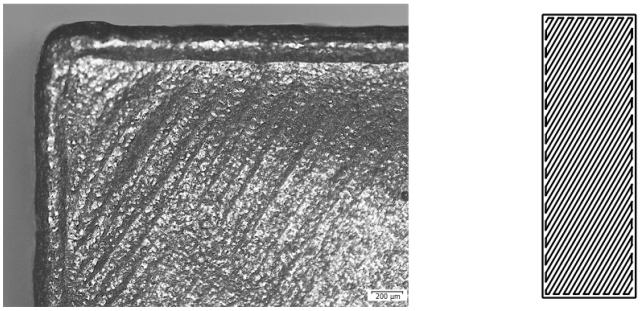

Figure 48: Hatching and contouring on the top of a sample. Left: Optical microscope of surface. Right: Illustration of contouring.

The parts are as-build, and has a rough surface. For one v-shaped notch specimen the surface roughness was measured on a Alicona Infinite Focus Microscope along a line of 2-4 mm length in the different regions of the sample, indicated by (a), (b), (c), and (d) in Figure 49. Region (a) is built with an overhang, region (b) is built with a positive angle and region (c) and (d) are built straight upwards. The building angle and surface roughness is shown in Table 12, the overhang region has a significantly higher surface roughness than the other regions.

Scanning Electron Microscopy (SEM) of the two surfaces noted by (a) and (b) in Figure 49 is

Table 12: Surface roughness and angle of printing relative to build direction

	a	b	c	d
Printing angle [°]	-45	45	0	0
Roughness, Ra [μm]	20.95	3.09	1.97	3.21

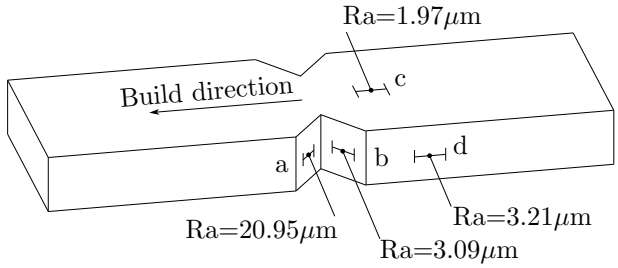

Figure 49: Different surface roughness in different regions of the samples. The region a is build with overhang and has a higher roughness compared to the other regions.

shown in Figure 50. The surface (b), left in Figure 50, has a wavy-like surface, corresponding to the height of the layers building the part. While surface (a), built with an angle of -45° (overhang), is rougher, and it seems like the gravity has been pulling the material downwards forming droplets hanging down from the part. From the SEM both surfaces appears to have been sandblasted.

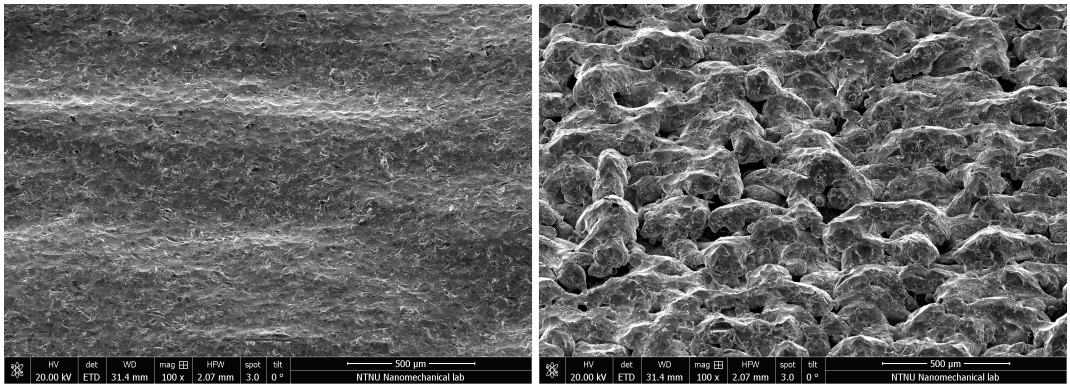

Figure 50: SEM of surface in notched region.

Optical microscopy of polished specimens are shown in Figure 51. The cross section is shown in Figure 51a and shows less amount of porosities in the contouring region, and higher amount of porosities in the hatched region. The same result has been shown by S.Tammas-Williams et al. [11]. In Figure 51b the specimen is polished down from the surfaces, both lack of fusion and porosities are visible, it appears that there are no porosities in the region close to the larger defects.

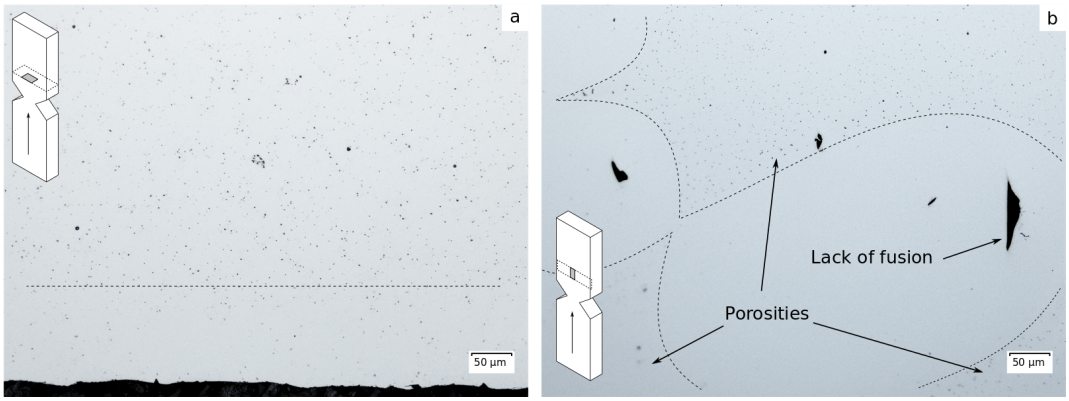

Figure 51: Optical microscopy of polished surface in two different orientations.

5.3 Static Test

A static test of on AM IN718 specimen was done in order to find the ultimate tensile strength of the material. The geometry of the sample was the unnotched, produced by the same company with the same specifications, but from a different batch of specimens. The test was performed with a loading rate of 0.03mm/min in room temperature. The results from the test is shown in Figure 52. The maximum applied load was 33.6 kN, this corresponds to a ultimate tensile strength of 960 MPa. The test is not performed with an extensiometer, so the Young's modulus or yield strength can not be determined accurately, however the loading path starts to deviate from the linear elastic part at about 25 kN, this corresponds to a yield strength of 714 MPa. It should be noted that this is only one static test, and there is a possibility of lack of fusion and other defects in the material reducing the material properties measured, as reported by D. Wells [49].

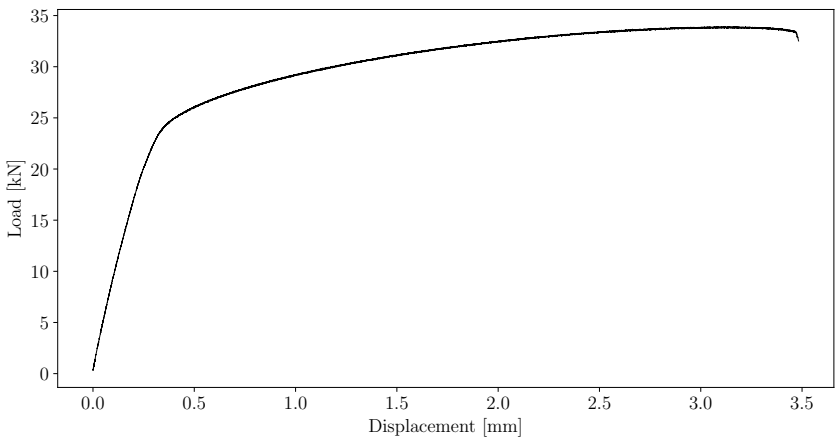

Figure 52: Static test of unnotched specimen

5.4 Fatigue Testing

For fatigue, the samples will be tested in room temperature on an MTS Landmark Servohydraulic Test System with a loading frequency of 10 Hz load controlled sinusoidal loading. In order to avoid compressive stresses in the notched regions the loading ratio R ($\sigma_{max}/\sigma_{min}$) is set to 0. When testing, a maximum and minimum load is defined. The minimum load is 0 kN for all test. When the tests starts the load is first ramped to the mean load level, when this is done the cyclic loading begins. The samples is clamped by the grips with a pressure of 6 MPa. The test machine with specimen inside, and detail of fixed specimen with brackets used for aligning the sample is shown in Figure 53.

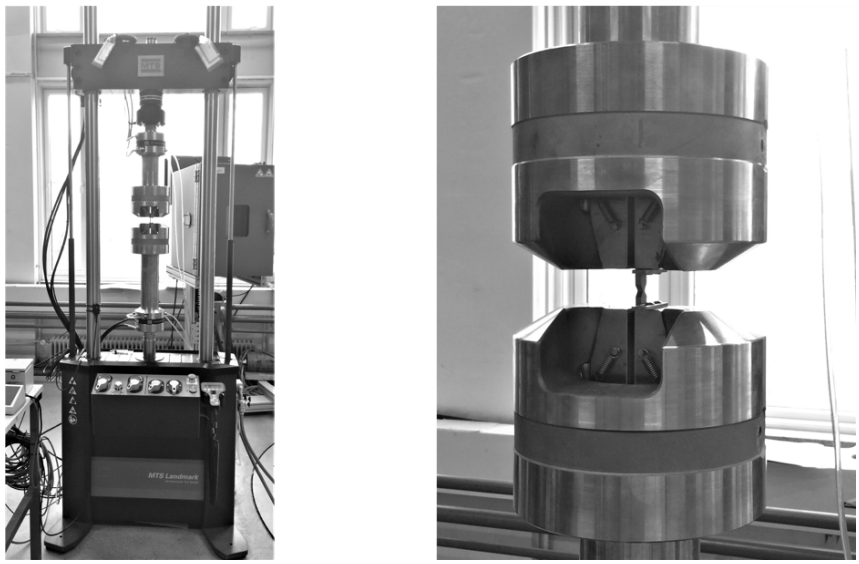

Figure 53: MTS Machine and mounting of samples used for fatigue tests.

6 Analysis

In this section different analysis of the test specimens is described. Numerical analysis is done by use of Finite Element in Abaqus/CAE. Analytical calculations is done based on the mathematical model by P. Lazzarin and R. Tovo [20], described in Section 3.4.5.

6.1 Introduction to the Finite Element Method

Finite Element (FE) is a numerical method of solving mathematical problems often related to engineering and physics. The concept is to discretize a problem into several finite elements with some property, boundary conditions and loads applied, the degree of discritization determines the accuracy of the analysis. Complex structures can be represented by a finite number of elements, for example trusses or beams. The problem is then reduced to a set of equations with a finite number of unknowns, this new system of equations can be solved done by use of computers. In FE physical response is represented by field variables, which is expressed as interpolation functions for each element. Elements are usually defined by nodes placed at he boundaries of the element [51].

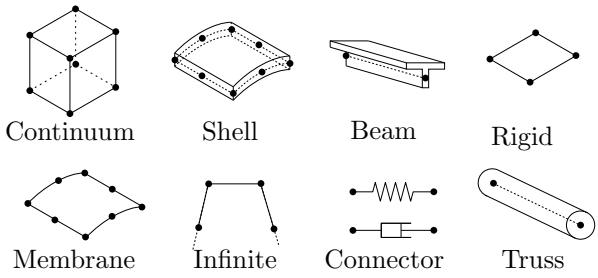

Figure 54: Element families in Abaqus [52].

In this work the software Abaqus CAE will be used for doing simulations on the test specimens. There are several different types of elements available in Abaqus, the different families of elements are shown in Figure 54. The displacements/degrees of freedom is calculated at the the nodes of the elements, at any other point in the element we need to interpolate in order to find the displacement. This interpolation order is given by the geometric order of the element. Linear or first-order elements have nodes only at the corners of the elements, while quadratic or second order elements have midside nodes and nodes at the corners of the elements, and therefor higher order of interpolation functions [52]. In order to describe material behaviour Abaqus uses numerical integration, for most elements Gaussian quadrature is used. Abaqus therefore evaluates material response in the integration points inside the elements. Choosing continuum elements in Abaqus one can choose either full or reduced integration, the reduced integration option will use less number of integration points and therefore give less accuracy [52].

6.2 Numerical Analysis - General Setup

Two different types of simulations will be done in this thesis:

- The elastic stress fields in the different geometries will be found, these stress fields will

be compared to analytical solution by P. Lazzarin and R. Tovo [20], and the stress concentration factors, and notch stress intensity factors (NSIF) are calculated.

- SED analysis is done on the different geometries and their $S-N$ curves, from this one single $\Delta\bar{W}_c - N$ curve with all the fatigue results will be presented.

The general setup in Abaqus for the both simulations calculating the elastic stress field and the SED is the same, the only change is the mesh and the outputs. Abaqus is built up in modules; for each module some data can be specified, and output can be requested, the following has been specified in the different modules.

- In the part module the geometry is created. The geometries are simplified to 2D models and symmetry is utilized as shown in Figure 55.
- In the property module the material properties is defined, elastic material is defined, with a Young's modulus of 200 GPa and a Poisson's ratio of 0.29 [53]. Abaqus does not operate with units, all units use will be in SI[mm].
- In the step module one step is created as static general .
- In the load module the loads and boundary conditions are added. The boundary conditions are added in the initial step, and the loads are added in step 1. The load and boundary conditions is shown in Figure 55, the load applied is $\sigma_0 = 1$ MPa in tension.
- In the mesh module CPS8 elements are used. The CPS8 elements are 8-node plane stress quad elements, with quadratic geometric order, without reduced integration.

Figure 55 shows the simplification, coordinate systems used, boundary conditions and loads of the notched specimen used in Abaqus.

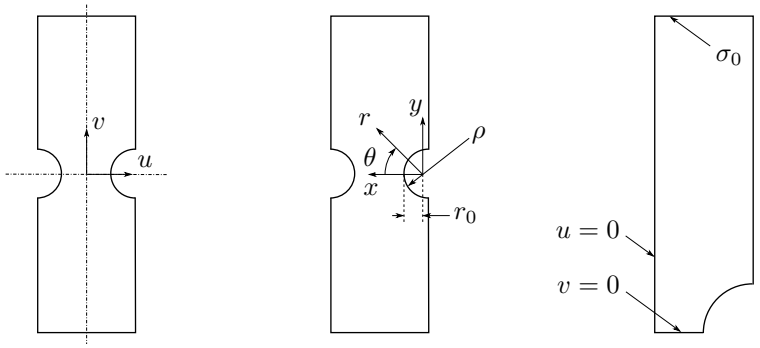

Figure 55: Left: uv-coordinate system in the centre of the specimen. Centre: Coordinate system and some parameters from Lazzarin et al. mathematical models for linear elastic stress fields. Right: Boundary conditions and loads applied in the Abaqus model.

6.3 Simulations for Obtaining Stress Fields

Describing the stress state in the region close to the notch tip is the goal in these simulations. In the areas where the stress gradient is steep, a fine mesh is needed in order to capture the

stresses accurately. In order to save computational time, coarse mesh is used in the areas far away from the notch tip. To avoid distorted elements the geometries are partitioned and meshed by the method shown in Figure 56. The mesh for the four different geometries used in the simulations calculating the stress concentration factors is showed in Figure 57.

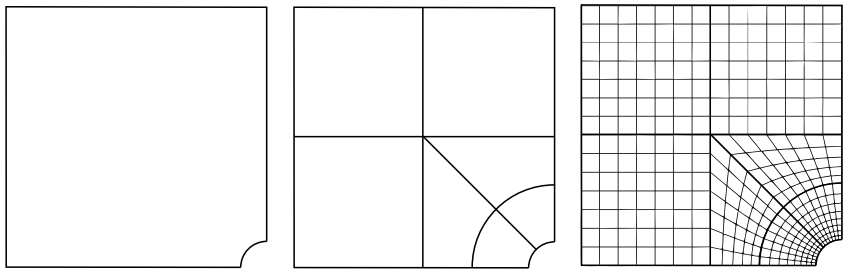

Figure 56: Method for meshing notched components. Left: Part geometry. Centre: Partitioned part geometry. Right: Meshed part.

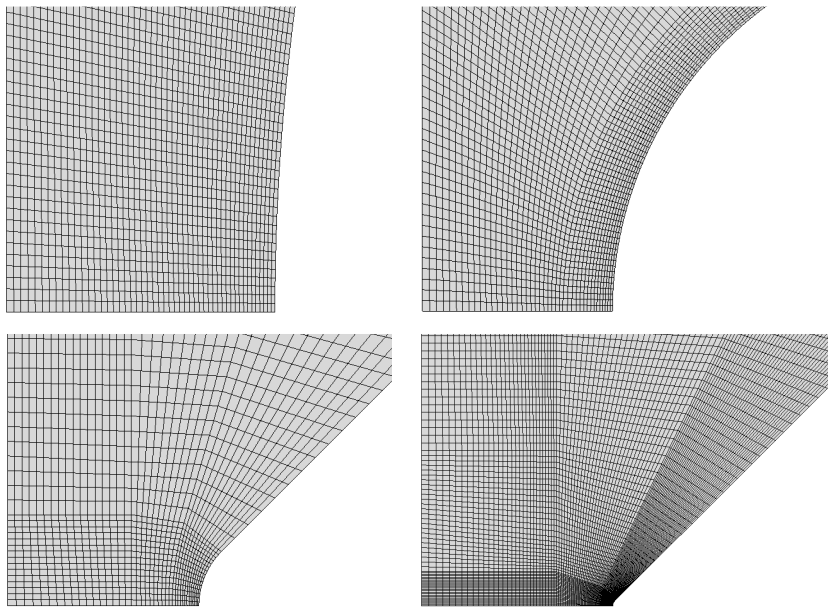

Figure 57: Detail of mesh from Abaqus. Upper left: Unnotched specimen. Upper right: Semicircular notched specimen Lower left: V-shaped notch ρ=1mm. Lower right: V-shaped notch ρ=0.1mm.

The results from the FEA is shown in Figure 58. The stress component $\sigma_{\theta\theta}$ divided by the nominal stress, is plotted versus the distance from the centre of the specimen. The elastic stress concentration at the notch tip is given by $k_t = \sigma_{\theta\theta max}/\sigma_{nominal}$, giving the stress concentrations as shown in Table 13.

6.4 Analytical Solution of Stress Fields

General formulation of the stress fields under mode I loading expressed in terms of maximum local stress according to Lazzarin et al. [20]:

$$\begin{aligned}\begin{bmatrix}\sigma_{\theta\theta}\\ \sigma_{rr}\\ \tau_{r\theta}\end{bmatrix} = \frac{\sigma_{max}}{4}\left(\frac{r}{r_0}\right)^{\lambda_1-1}\Bigg[\Bigg[\Bigg[\begin{bmatrix}(1+\lambda_1)\cos(1-\lambda_1)\theta\\ (3-\lambda_1)\cos(1-\lambda_1)\theta\\ (1-\lambda_1)\cos(1-\lambda_1)\theta\end{bmatrix}\\ + X_1(1-\lambda_1)\begin{bmatrix}\cos(1+\lambda_1)\theta\\ -\cos(1+\lambda_1)\theta\\ \sin(1+\lambda_1)\theta\end{bmatrix}\Bigg]\\ + \left(\frac{r}{r_0}\right)^{\mu_1-\lambda_1}[(3-\lambda_1)-X_1(1-\lambda_1)]\begin{bmatrix}\cos(1+\mu_1)\theta\\ -\cos(1+\mu_1)\theta\\ \sin(1+\mu_1)\theta\end{bmatrix}\Bigg]\end{aligned} \tag{30}$$

Where the coefficient X_{ik} are given:

$$X_1 = -\frac{\sin(1-\lambda_1)q\pi/2}{\sin(1+\lambda_1)q\pi/2} \tag{31}$$

In the case of the unnotched and the semi-circular notch the stress distribution of a u-shaped notch will be used [20]:

$$\begin{bmatrix}\sigma_{\theta\theta}\\ \sigma_{rr}\\ \sigma_{r\theta}\end{bmatrix} = \frac{K_I}{\sqrt{2\pi r}}\begin{bmatrix}\cos(\theta/2[(1-\sin^2\theta/2) & +\rho/2r])\\ \cos(\theta/2[(1+\sin^2\theta/2) & -\rho/2r])\\ \sin(\theta/2[(\cos^2\theta/2) & +\rho/2r])\end{bmatrix} \tag{32}$$

For $\theta = 0$ and $K_I = \sigma_{max}\sqrt{\pi\rho}/2$ the solution to the stress field for the unnotched geometry can be written as:

$$\sigma_{\theta\theta} = 1.94647\sigma_{max}(1 + 15.155r^{-1})r^{-0.5} \tag{33}$$

And for the semi-circular it can be written as:

$$\sigma_{\theta\theta} = 0.79056\sigma_{max}(1 + 2.5r^{-1})r^{-0.5} \tag{34}$$

In the case of the v-shaped notches the P. lazzarin and S. Filippi has reported parameters used in the mathematical model for different v-shaped notch geometries [54]. The parameters obtained is shown in Table 13.

Along $\theta = 0$ the stress field for v-shaped notch with $\rho = 1$ mm can be expressed as:

$$\sigma_{\theta\theta} = 0.153\sigma_{max}(2.380 + 0.609r^{-0.890})r^{-0.455} \tag{35}$$

And the stress field for v-shaped notch with $\rho = 1$ mm can be expressed as:

$$\sigma_{\theta\theta} = 0.0532\sigma_{max}(2.380 + 0.07448r^{-0.890})r^{-0.455} \tag{36}$$

Table 13: Values used for the analytical solution of the elastic stress field for the different notch geometries. λ_1 and μ_1 values are used from [54]

	ρ	r_0	2α	q	λ_1 [54]	μ_1 [54]	$\bar{\omega}$ [54]	k_t
Unnotched	30.31	15.16	0	2.000	0.500	-0.500	1.000	1.073
Semicircular notch	5.000	2.500	0	2.000	0.500	-0.500	1.000	1.308
v-shaped notch r=1	1.000	0.333	$\pi/2$	1.500	0.545	-0.345	0.810	2.279
v-shaped notch r=0.1	0.100	0.033	$\pi/2$	1.500	0.545	-0.345	0.810	6.236

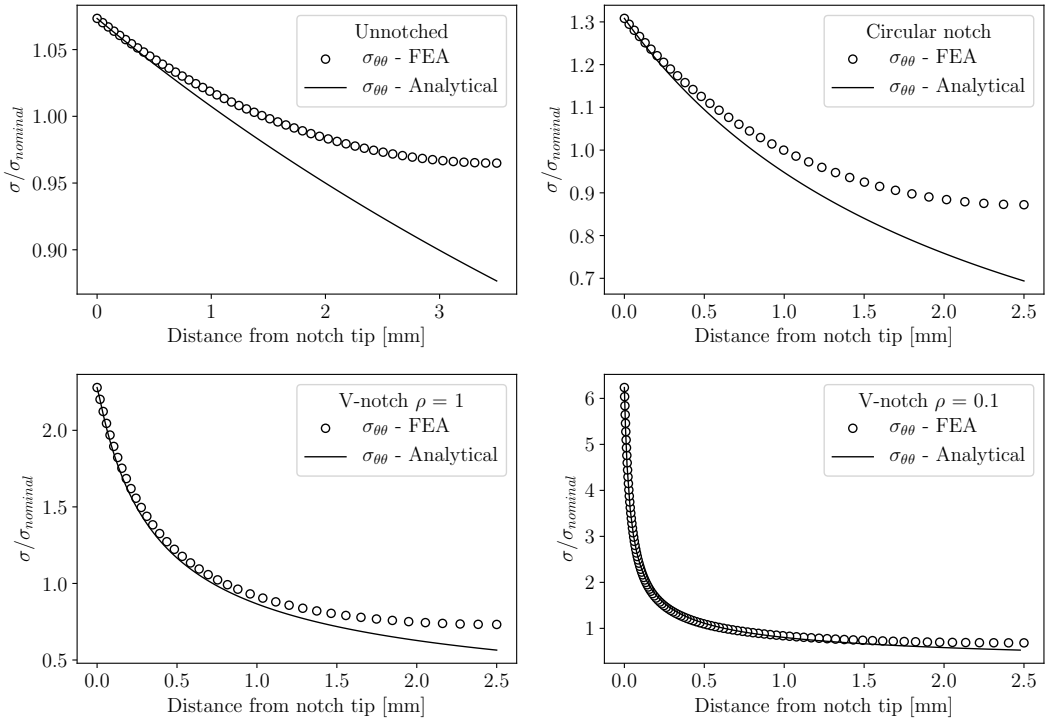

Figure 58: For the different geometries the stress is plotted along the notch bisector line, this is done for FEA and for analytical solution

6.5 Comparison Between Numerical and Analytical Stress Fields

Figure 58 shows the analytical and numerical solution to the elastic stress field in the geometries, from the plot it seems that the mathematical model for v-shaped notches are quite accurate, while the semi-circular and unnotched does not show a good fit. Some remarks on the fit:

- The fit is better as the sharpness of the notch increases
- The accuracy of the model can be influenced by the fact that the geometries are double notched, and not infinite plate. The model should give a more accurate result for a small value of ρ/w_2 than for a large one. This has also been noted by P. Lazzarin and S. Filippi [54].
- Assuming u-shaped notch for unnotched and semi-circular notch could be a bad choice

and not describing the geometry well.

6.6 Notch Stress Intensity Factor

The stress fields can be expressed in terms of NSIF by the relation suggested by P. Lazzarin and S. Filippi [54]:

$$K = \sqrt{2\pi} r^{1-\lambda_1} \frac{\sigma_{\theta\theta}}{1 + \bar{\omega}_1 \left(r/r_0\right)^{\mu_1 - \lambda_1}} \tag{37}$$

The parameters used for the formulation of NSIF for the different geometries is shown in Table 13. The stress component $\sigma_{\theta\theta}$ is plotted in log-log coordinates versus distance, r, with the coordinate system placed as described in Figure 19. A sharp v-notch is also analysed, taken as a reference value checking the value for the two blunt v-shaped notches. The NSIF for a notch with a finite radius should be higher than for a sharp notch, as reported by Lazzarin and Filippi [54]. Using the formulation from Equation 11 the stress field is expressed as [20]:

$$\sigma_{\theta\theta} = 0.732 K r^{-0.455} \tag{38}$$

The stress distributions are shown in Figure 59, both stress versus distance, r, and NSIF and SIF versus distance r. In the case of v-shaped notch with radius equal to 1 mm and 0 mm, the models are able to predict a constant value of NSIF and SIF. While for the semi-circular notch and the v-shaped notch with radius of 0.1 mm, the model does not give a constant value NSIF. Expressing the stress field by a different placement of the coordinate system was tried, that is, changing the value of r_0. For the semi-circular notch, the value was changed from 2.5 mm to 2.85 mm, while for the v-shaped notch with a radius of 0.1 mm, the value was changed from 0.033 mm to 0.026, to obtain a constant value of NSIF.

Table 14: Values used of notch stress intensity factors and r_0 used.

	r_0	K/σ_{nom}
Semi-circular	2.8500	6.944
V-shaped notch $\rho = 1$	0.3333	1.166
V-shaped notch $\rho = 0.1$	0.0026	1.018
V-shaped notch $\rho = 0$	0	1.022

The results of NSIF and SIF calculations are shown in table 14. As reported by P. Lazzarin and S. Flippi [54], the NSIF values is increasing with the radius of the notch. The Lazzarin model is fitting well for both the sharp notch and the notch with 1 mm radius, however for the notch with 0.1 mm radius and the semi-cirular notch, the model is not fitting perfectly for the suggested value of r_0.

6.7 Simulations for SED

For the SED analysis in Abaqus the control region around the notch is defined, and in this region volume and strain energy is requested. Other than this the same boundary conditions, loads, element type and material as the analysis for obtaining the stress fields is used. Based on the strain energy and volume requested from Abaqus simulations, the

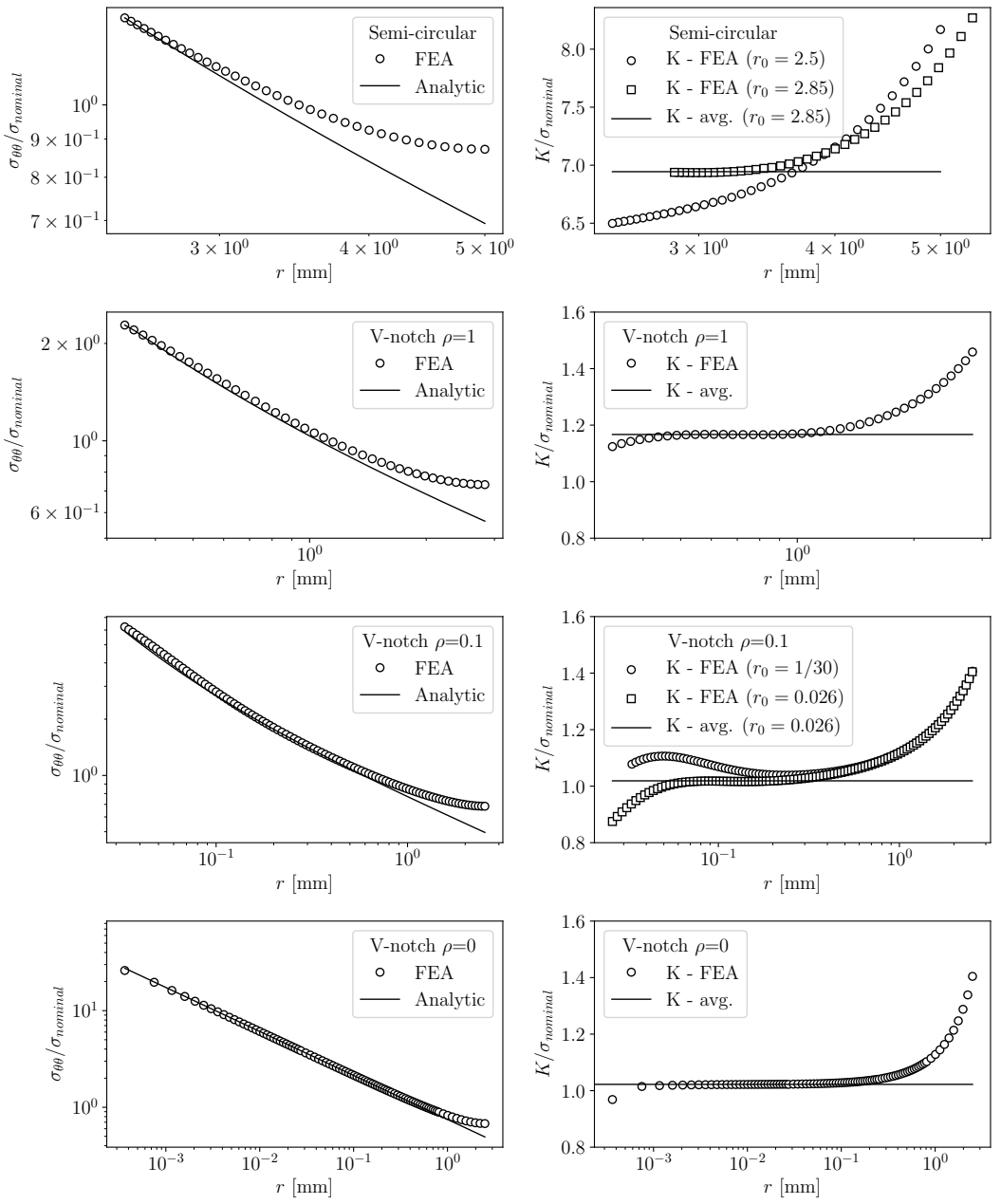

Figure 59: Left: For different v-shaped notch geometries the stress distribution is shown in log-log coordinates and compared to the analytical solution. Right: the stress intensity factor K, calculated based on the stress distributions.

avg. SED is calculated. SED is calculated for several values of the critical radius, Figure 60 shows the mesh in the control region used for a critical radius of 1 mm, note the mesh is very coarse compared to the simulations used for obtaining the stress fields.

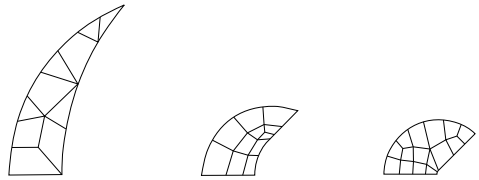

Figure 60: Mesh inside the control region for the different notch geometries, with a critical radius of 1 mm.

7 Results and Discussion

In this section the results obtained from testing and simulations will be presented and discussed.

7.1 Fatigue Strength

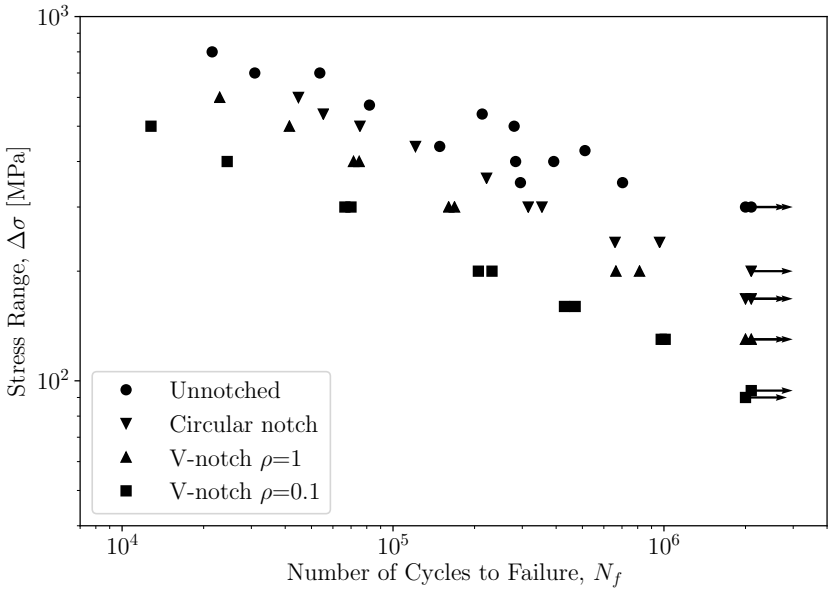

Figure 61: Fatigue data for all the different notch geometries.

The data from the fatigue test is shown in Figure 61. The data is showing a correlation between the elastic stress concentration factor and the fatigue notch sensitivity.

Haibach scatter bands is calculated in the software Faticaw, for confidence levels 97.7%, 50% and 2.3% as shown in Figure 62. The scatter parameter $T_{\Delta W}$ and the inverse slope of the curves, k, are shown in the figure. In Table 15 the parameters from the Haibach scatter bands are shown at 2×10^6 cycles.

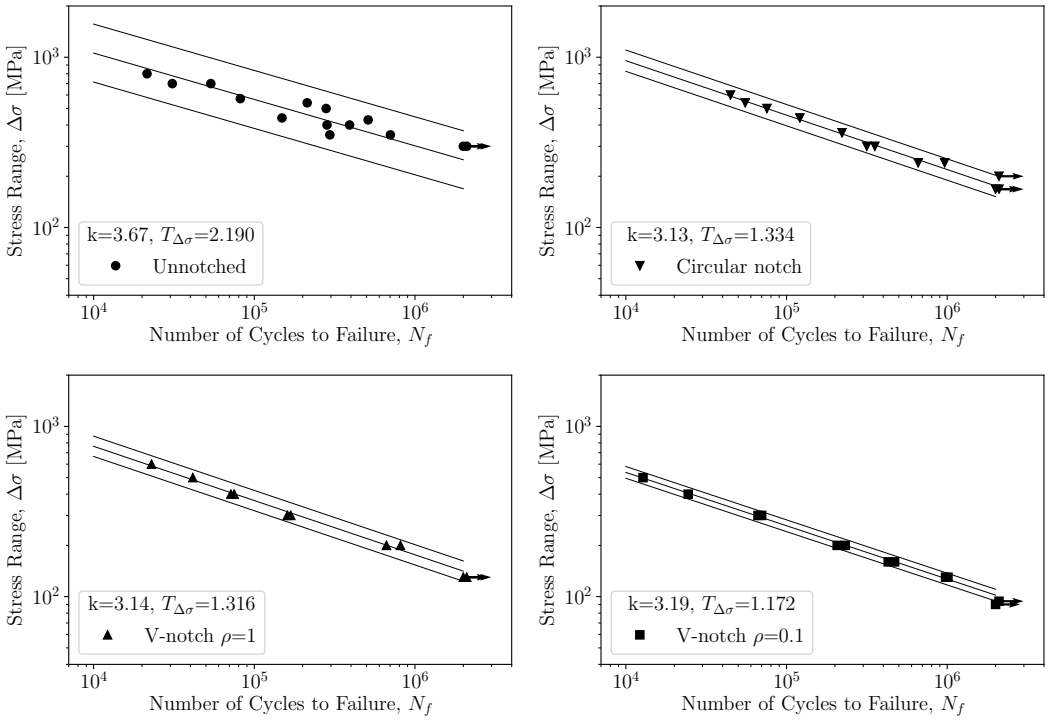

Figure 62: Fatigue data for all the different notch geometries plotted with Haibach scatter bands at 97.7%, 50% and 2.3%.

Table 15: Parameters for haibach scatter bands at 2×10^6 cycles.

	$\Delta\sigma$ - 97.7%	$\Delta\sigma$ - 50%	$\Delta\sigma$ - 2.3%
Unnotched	168.93	250.00	369.99
Semicircular notch	151.88	175.40	202.58
V-shaped notch ρ=1	123.12	141.23	161.99
V-shaped notch ρ=0.1	94.25	102.05	110.49

7.2 Notch sensitivity

Table 16: Theoretical and real notch sensitivity

	k_t	$k_f^{theoretical}$	k_f^{real}
Unnotched	1.0733	1.0731	1.0000
Semi-circular notch	1.3082	1.3022	1.4253
V-shaped notch ρ=1	2.2794	2.1633	1.7702
V-shaped notch ρ=0.1	6.2359	3.7161	2.4498

The stress concentration factor k_t is calculated based on numerical simulations in Section 6.3, based on these results and Peterson equation for fatigue notch sensitivity, k_f (Equation 16), using the ultimate tensile strength obtain from static test, the fatigue notch sensitivity is estimated. The real notch sensitivity is calculated based on the fatigue strength at 2×10^6 cycles for the different specimens, and the values are shown in Table 16 compared with

the estimated notch sensitivity. The semi-circular notch has a higher notch sensitivity than predicted, while the v-shaped notch specimens have lower notch sensitivity than predicted. The scatter band parameter $T_{\Delta\sigma}$ for the different notch geometries shows a correlation with the notch sensitivities. For a low notch sensitivity the scatter is high, while for a high notch sensitivity the scatter is low.

The notched fatigue behaviour of Q. Chen et al. for conventional manufactured IN718, displays a fatigue sensitivity much lower than the elastic stress concentration factor in room temperature, where $k_t = 5.67$ and $k_f = 1.74$ [34]. It should be noted that these results are from rotating bending, and the difference in the stress gradients can effect the difference in results. However it is not logic that the semi-circular notch should have higher notch sensitivity than the elastic stress concentration factor, as q is supposed to be between 0 and 1 [16]. This could indicate that there are other mechanisms causing the reduction in the fatigue life.

7.3 Comparison to Other Fatigue Data

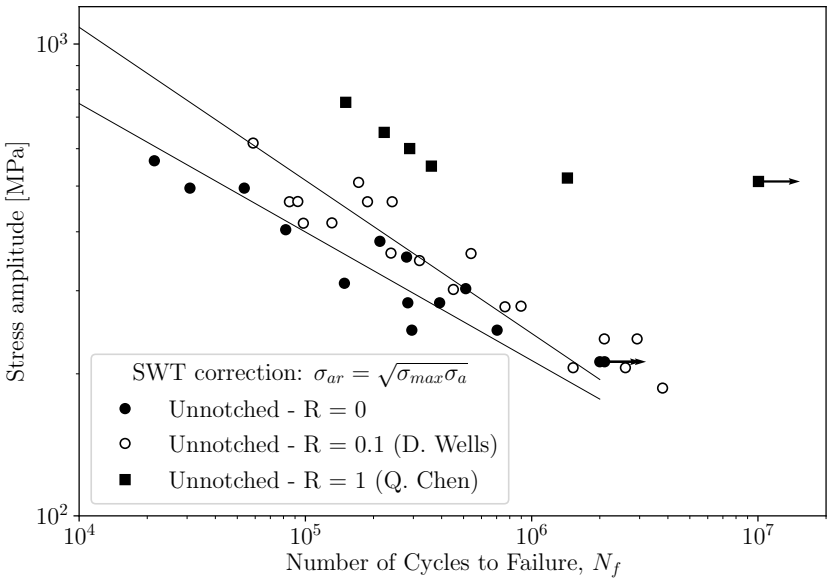

Figure 63: Fatigue data for unnotched specimen compared to results from D. Wells, corrected with SWT mean stress correction.

The fatigue results for the unnotched samples is compared to fatigue results of as-build specimens by D. Wells in Section 4.2, and the results are shown in Figure 63. The fatigue data is corrected for mean stress by SWT-correction [16]. Haibach scatter bands from were calculated, and is shown for confidence level 50%. The data shows a steeper slope for the D. Wells results than the results from this work, with an inverse slope k of 3.08 compared to 3.67. The difference in scatter is small, the scatter parameter $T_\Delta\sigma$ is of the D. Wells data is 2.176 compared to 2.190. The fatigue strength calculated at 2×10^6 cycles by Haibach scatter bands for the D. Wells data are 194.56 MPa, while the unnotched specimens from this work has 176.78 MPa (with SWT correction). This shows that at 2×10^6 cycles the fatigue strength is similar for the two different tests.

Using the 50% confidence Haibach scatter bands at 2×10^6 cycles for the unnotched specimens corrected with SWT, and comparing it to the Q. Chen et al. fatigue data also shown in Figure 63 for unnotched heat treated samples showing a fatigue limit of about 500 MPa, it is evident that the conventional manufactured IN718 is superior. However this comparison is not completely fair as the Chen et al. specimens was both machined and heat treated, and the loading was rotating bending, and not uniaxial tension.

7.4 Hysteresis Loop

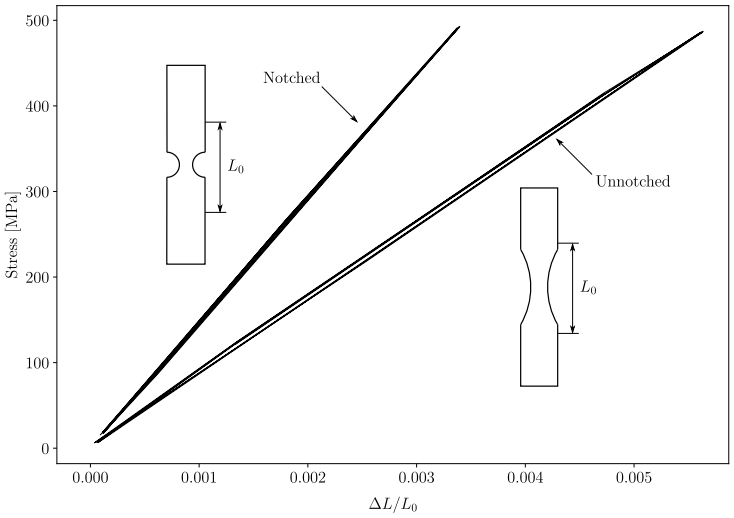

Figure 64: Load versus displacement plotted for unnotched and notched samples.

For specimens subjected to stress range of 500 MPa, the load versus relative displacement is plotted for semi-circular and unnotched specimens. The relative displacement is considered by evaluating the displacement of the grips on the testing machine, ΔL, and the distance, L_0, between the grips. This is plotted versus the nominal stress in the notched region. The slope of the curve does not show the elastic modulus of the material, but the stiffness of the specimens between the grips. The slope of the curves shows minimal amount of plasticity for both specimens. The notched specimen is showing a higher stiffness than the unnotched specimens, this is because of the amount of material present between the grips, even though the cross section in the notch in the notched specimen is smaller than the unnotched one. The load displacement curve is plotted from cycle 25 000 to 25 005 for both geometries.

7.5 Critical Average Strain Energy Density Range

In order to define the critical radius the formulation from Equation 27 is used and the results are shown in Table 17. The results shows a large variation in the critical radius. Since the method based on equation 27 gives different radius for different geometries, the formulation in Equation 29 is employed. The critical radius is calculated by comparing the unnotched geometry to the v-shaped geometry with radius of 1 mm. $\Delta\bar{W}_c^{Smooth}$ is calculated to be 0.15625 Nmm/mm^3, while $\Delta\bar{W}_c^{notched}$ is calculated in FEA for different values of R_0, both are evaluated at the stress level corresponding to fatigue strength at 2×10^6 cycles. The

Table 17: Values used for SED calculations

	K/σ_{nom}	$f_1(2\alpha)$	$\Delta\sigma^N$	ΔK_{IC}^N	R_0
Semi-circular	6.944	1.959	175.40	1188.96	5.8928
V-shaped notch ρ=1	1.166	1.852	141.23	153.336	0.1033
V-shaped notch ρ=0.1	1.018	1.852	102.05	103.007	0.0375
V-shaped notch ρ=0	1.022	1.852	102.05	103.354	0.0378

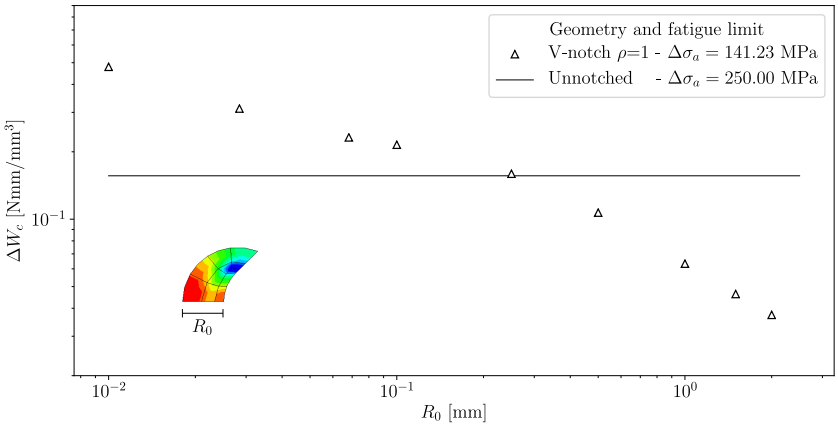

Figure 65: Critical avg. SED range at fatigue limit for v-shaped ρ = 1mm and unnotched geometry. The contour plot shows the results from strain energy with a control radius of 1 mm.

results are shown in log-log coordinates in Figure 65. The conditions of Equation 29 is met by using a value of $R_0 = 0.25$. It should also be noted that the slope of the $\Delta\bar{W}_c^{Notched}$ data is changing at this value.

When the critical radius is defined it is possible to calculate the critical avg. SED range for all the notched fatigue data by using the SED values obtained from the FEA:

$$\frac{\Delta W_c^{Notch}}{(\Delta\sigma_A^{Notch})^2} = \frac{\bar{W}_{FEA}^{Notch}}{(\sigma_{FEA}^{Notch})^2} \Rightarrow \quad \Delta W_c^{Notch} = \bar{W}_{FEA}^{Notch} \left(\frac{\Delta\sigma_A^{Notch}}{\sigma_{FEA}^{Notch}}\right)^2 \tag{39}$$

The result from this is shown in Figure 78 with $R_0 = 0.25$ mm. Haibach scatter bands are created in Faticaw, giving a inverse slope k = 1.48 and a scatter parameter $T_{\Delta W} = 2.777$. Comparing these results with the SED analysis of 900 weld data done by F. Berto et al. [25] the inverse slope is k = 1.5 and $T_{\Delta W} = 3.3$. In Appendix B avg. critical SED is shown for different values of R_0, compared to the scatter bands of F. Berto et al. [25]. The fact that the fatigue data is able to be represented in one unified curve, indicates that SED can be applied to AM materials under fatigue loading. It should also be noted that successfully approaches of relating SED to fatigue of AM components has not yet been reported in literature.

7.6 Fractography

Figure 67 shows SEM of an unnotched samples failing at 213 391 cycles, with an applied stress range of 540 MPa. The whole cross section is shown in Figure 67a, with crack propagation

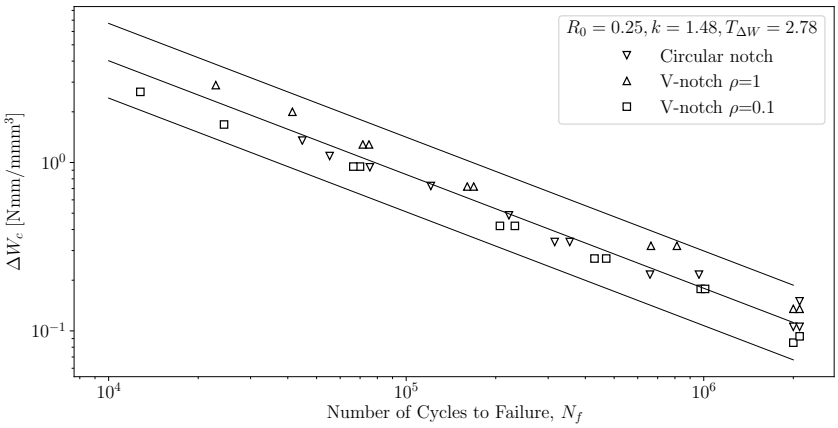

Figure 66: Critical strain energy density range versus number of cycles to failure, with Haibach scatter bands at 97.7%, 50% and 2.3%.

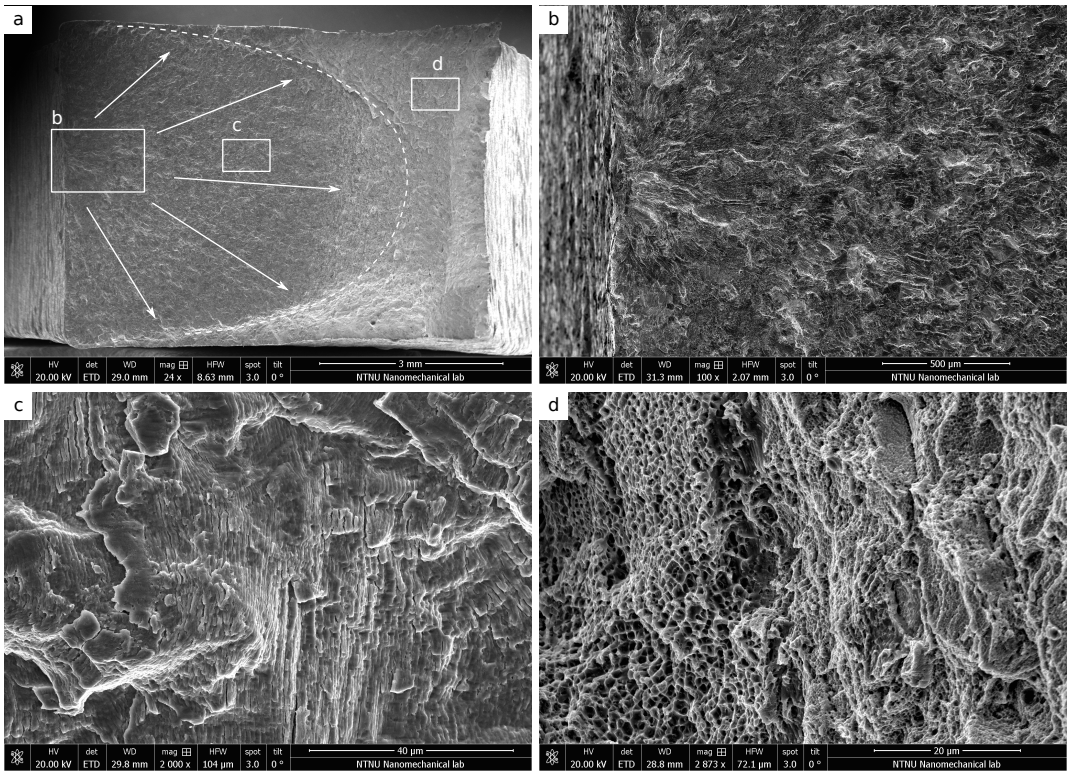

Figure 67: SEM of unnotched sample. a) whole cross section b) Crack initiation, c) Striations showing crack propagation direction, d) Ductile fracture surface for final rupture.

indicated by arrows, and transition from crack growth to final rupture indicated by dashed lines. The crack is initiating from a small defect in the surface shown in b). The striations from the crack propagation indicating the direction of the crack growth is shown in c). In the final rupture region the dimples formed by void coalescence and plasticity is visible, this

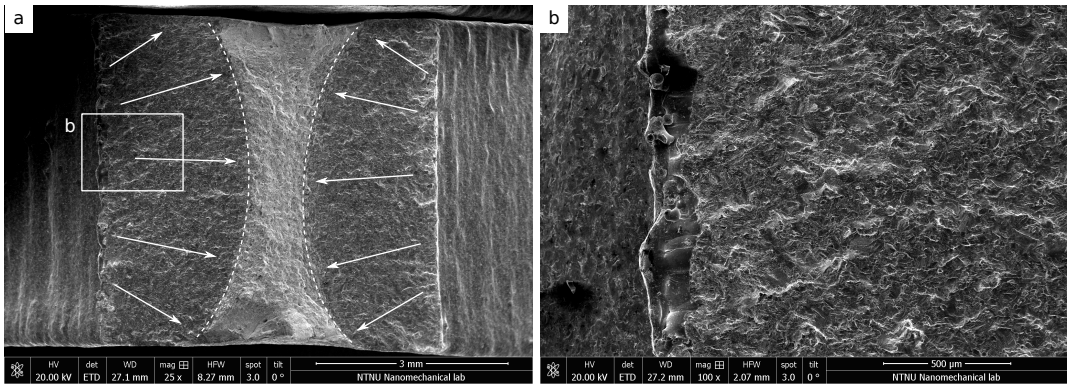

Figure 68: SEM of v-shaped notched sample with radius of 1 mm. a) Whole cross section. b) lack of fusion and partly unfused powder particles on surface.

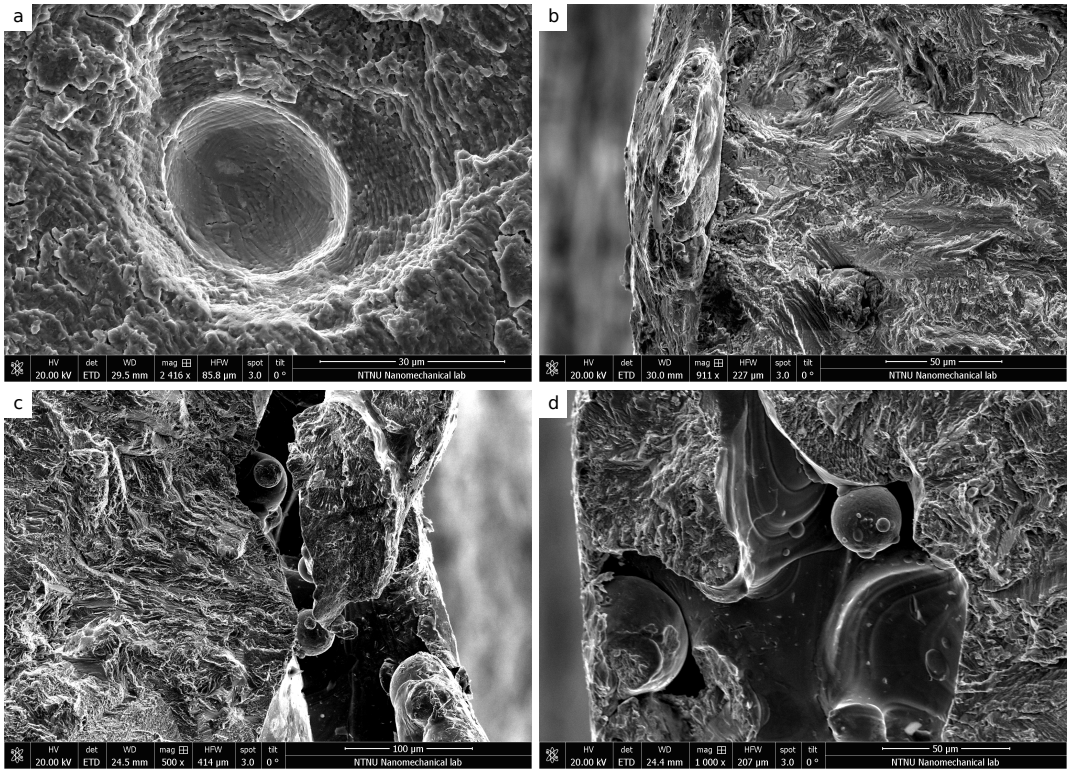

Figure 69: Defects in different samples. a) porosity inside sample. b) crack initiation site for unnotched sample. c), d) lack of fusion and unmelted particles at crack initiation site for notched samples.

is shown in d.

Figure 68 shows SEM of a v-shaped notched sample with radius of 1 mm, failing at 160 444 cycles with an applied stress range of 300 MPa. In the v-notched samples the cracks are propagating from both sides, and meeting at the centre of the specimen in final rupture. As in the unnotched sample (Figure 67) there is a distinct transition from fatigue crack to final

rupture. The crack starts from an area with lack of fusion in the surface of the notch as shown in b).

Figure 69 shows different defects in different samples. a) shows a void inside an unnotched sample, the striations are visible and clearly interacting with the void. b) Shows a typical crack initiation from an unnotched sample. There is no oblivious lack of fusion of unfused particles as in the notched samples, but still some kind of defect. c) and d) Shows crack initiation from lack of fusion at the surface of a semi-circular specimen. Unfused powder particles are visible in the unfused regions, the powder particles are of size $\sim$30 μm.

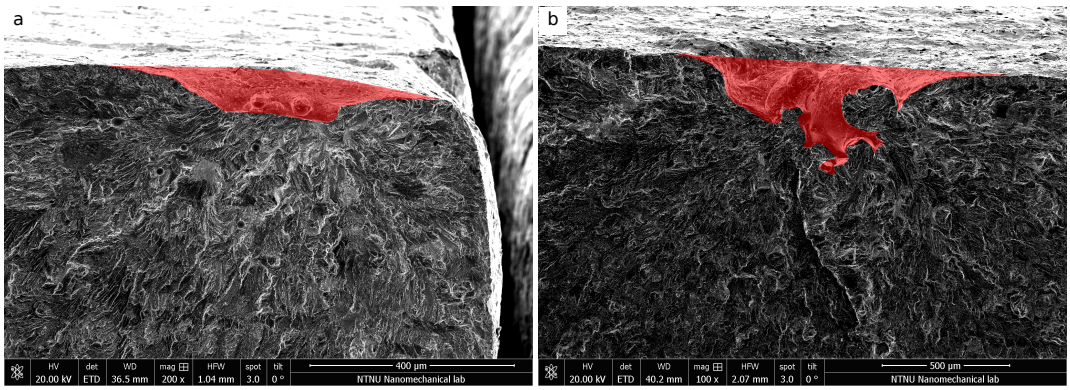

Figure 70: Comparison of size of defect between two samples tested at $\Delta\sigma = 175$ MPa. a) Failing at 703 473 cycles, b) failing at 295 332 cycles

For an applied stress range of 175 MPa the size of surface defect of two unnotched samples failing at different positions in the scatter bands where measured as shown in Figure 70. The specimen in a) failed at 703 473 cycles and had a surface defect of 31.64 μm^2, while the specimen in b) failed at 295 332 cycles and had a surface defect of 173.73 μm^2, both cracks initiated from the surface defects. This indicates that there is a correlation between the size of defect and fatigue life of the specimen, as has been proposed by Tammas-Williams et al. for AM Ti6Al4V [55].

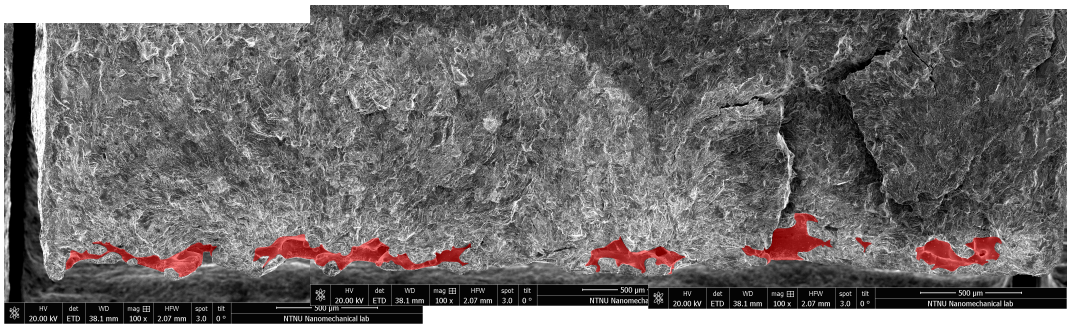

Figure 71: Lack of fusion defect in semi-circular specimen tested at $\Delta\sigma = 240MPa$ failing at 659 809 cycles.

The total area of lack of fusion for one semi-circular specimen with an applied stress of 240MPa failing at 659 809 cycles was measured, the lack of fusion area, shown in red in Figure 71. The total area was measured to be 235.6 μm^2. In the case of unnotched specimens there are just one defect initiating the crack (just one area of defect), while in the case of

the semi-circular specimen the surface defects are distributed along the whole edge of the notch, initiating crack from several places. This large region of lack of fusion could be the reason for the low fatigue life of the semi-circular specimens. Also be the semi-circular are not failing from the centre of the gauge section, but in the region slightly above where the material has been printed with overhang.

7.7 Material

The specimens used in this work in AM IN718 without any post processing. For IN718 post processing is usually done in order to increase the material properties. The reason for testing specimens without any post processing is that very limited data is yet published on AM IN718, and these data will function as a good fundament for comparing other IN718 data in the future, for example the effect of post processing such as machining, HIPing, heat treatment and etching. Starting at the worst possible condition of the samples, some positive effect should be seen when doing post treatment.

7.8 Elastic Stress Fields

The geometries used in the tests are analysed by use of elastic stress fields developed by P. Lazzarin, explained in Section 3.4.5. The stress fields are developed for 2D geometries with one notch. In this work the geometries are in 3D, the stress state is assumed to be plane strain, as the samples has approximately the same width and thickness. There are one notch on each side of the samples, this results in an interaction of the stress fields between the two notches. For the sharp v-notch geometry this was found to not give a large effect, as shown in the comparison of the analytically and the numerical solution to the stress distribution. For the blunt v-shaped notch the stress field is able to describe the stress intensity, which indicates that the interaction between the two notched is not to large for the mathematical model to be applied. For the semi-circular notch the stress field is not able to describe the stress intensity and the singularity very well, and also the comparison between the numerical and analytical solution does not give a great fit.

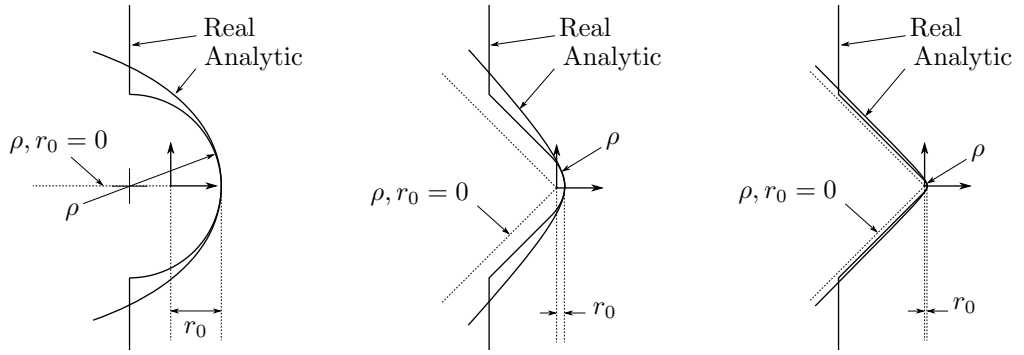

Figure 72: For the different notch geometries, the real and the analytic notch geometry is illustrated. For each geometry the model obtain when setting $\rho, r_0 = 0$ is also shown.

Figure 72 shows an illustration of the notch geometries and the mathematical models used to describe them. The models fits at the notch, however the opening angle for the mathematical model will be larger then for the real geometry it is trying to describe due to the coordinate

system transformation used to the describe the notch geometries. The model is accurate for sharp notch geometries, this is illustrated by plotting the stress distribution from the sharp v-notch, but for some notch geometries it will describe the geometry quite well, without capturing the singularity, this can be sees by comparing the stress distribution for v-shaped notch with radius of 0.1 mm from Figure 58, where it appears to give a accurate stress distribution, with the stress distribution from Figure 59 for the same geometry, where it fails to describe the stress intensity.

7.9 Reasons for Scatter in Fatigue Data

There is a large scatter in the fatigue data for the unnotched samples, while for the notched samples there are almost no scatter. Fatigue is a weakest link failure mechanism. For the notched geometries the notch should be the main driving factor, however the SEM showed the crack initiated from lack of fusion in the region of notch root. This indicates that for the notched samples the driving mechanisms for fatigue is a combination of lack of fusion region, acting as a crack, and the stress gradient from the notch. The small scatter in the fatigue data for the notched samples suggest that there are small variations in the driving mechanisms from specimen to specimen. In the case of the unnotched specimens Figure 69 showed a dependency of lack of fusion area and the placement in the scatter band. The printing angle for the unnotched specimens close to the gauge section is not high (not printed with large amount of overhang), and this probably gives less chance of lack of fusion. Other possible driving mechanisms for the fatigue failure can be the size effect, the cross section of the unnotched sample are larger than the notched samples, however this is not very likely as all the cracks initiates from the surface of the unnotched samples. The main reason for scatter in the data should irregular surface quality in the unnotched samples. The cracks are initiating at the surface of the specimens, these surface defects should be of different size. While for the notched components there should be relatively small variation in the surface defects, that is, the size of the area of lack of fusion close to the notch.

7.10 Use of SED on AM components

Additively manufactured materials are anisotropic and can contain residual stresses and geometrical discontinuities [2]. SED is based on linear elastic stress in homogeneous solids, but can be applied to other material assuming these conditions. SED is supposed to be applied to brittle and quasi-brittle failure in materials, the static behaviour of the AM IN718 is not brittle, but the fatigue failure of the material displays almost no plasticity (especially for high number of cycles). The fracture surface in the fatigue part of the crack propagation displays typical fatigue behaviour with striations and cleavage failure. This work is therefore an attempt to apply SED to a new material, and check if it is possible to employ it.

When designing components for AM, the geometries are likely to be complex, and containing highly notched regions. If it is possible to apply SED when designing notched components, huge amounts of computational time can be saved considering the number of notches, and the mesh required to capture the stress gradients, if a stress based failure criterion is used. SED is not mesh or notch dependent, and the fatigue life of a component could then be evaluated by use of FE models with coarse mesh, and knowing the master $\Delta\bar{W} - N$ curve for the material used.

One of the main problems for employing SED on AM materials will be determining the

critical radius, R_0, as this size is, for static, dependent on the fracture toughness and the ultimate tensile strength of the material, and for fatigue, dependent on the fatigue strength for both notched and notched geometries. These values are dependent on the process parameters and the post processing of the components, and this makes it difficult to determine one unified R_0 value for one material.

8 Conclusion

In this work the fatigue behaviour for different notch geometries of as-build AM IN718 has been investigated. First an introduction to concepts concerning AM, structural integrity, superalloys was given, then test and analysis methods has been explained, then the results of the tests and simulations has been presented and discussed. This conclusions will be given as a combination of some general conclusions, answers to the research questions and some possible future work.

General conclusion:

- AM is a relatively new fabrication process producing components in a layer-by-layer manner, allowing complex geometries not earlier possible in conventional manufacturing processes.
- With AM a large variety of materials can be used, for engineering purposes polymers and metals are considered most interesting.
- Topology optimization in computer softwares can be used in order to optimize designs for for examples stiffness and weight. However the designs obtained are often complex and can contain highly notched regions functioning as stress risers.
- Alloys such as IN718 and Ti6Al4V is commonly used when designing metal components for AM, this because of the mechanical properties.
- With heat treatment and other post processing, it is possible to obtain almost the same mechanical properties as for conventional manufacturing for IN718. However, post processing is not always possible or desirable using AM.

Answer to research questions:

1. What is the fatigue properties of as-built AM IN718?
    - The fatigue properties of AM IN718 has been documented and presented in $S-N$ curves where the data is presented in terms of scatter bands, slope of curve and fatigue strength at 2×10^6.
    - The $S-N$ data shows a clear notch sensitivity for the different geometries correlating with the elastic stress concentration factors obtained the stress field in FEA.
    - The surfaces built with overhang shows a higher surface roughness and more defects, the crack are initiating from these areas.
    - The unnotched fatigue behaviour exhibits a larger scatter in the fatigue data than the notched specimens.
    - Cracks are initiating from defects such as lack of fusion in the surface. These lack of fusion defects are larger for the notched samples, as they are manufactured with overhang.
    - The semi-circular notch exhibits a strong notch sensitivity, this indicates that there are different mechanisms causing fatigue for the different geometries, not just the stress gradient due to the notch. The SEM shows larger regions of lack of fusion than the unnotched specimens examined.

- When compared to conventional heat treated IN718, the AM material tested without any post processing is displaying a much lower fatigue strength.

2. How does notches influence the fatigue life of as-built AM718?

   - The notch influence the fatigue life of the specimens, functioning as a stress riser, but also as a region printed with overhang, causing larger areas containing defects such as lack of fusion.
   - The overhang regions from the notches has a strong influence to the fatigue properties, this is clear when comparing the fatigue notch sensitivity of the semi-circular specimen, which has a higher fatigue notch sensitivity then the elastic stress concentration factor, with the the v-shaped notched specimen the fatigue notch sensitivity, that is lower than the elastic stress concentration factor. This shows a correlation not only between the elastic stress concentration factor and fatigue notch sensitivity, but also between the printing angle and the fatigue notch sensitivity.
   - One important influence of notches in fatigue of AM components is simply that they will be present, and that removing surface defects by machining the components will be complicated or even impossible for complex geometries. Due to this, the notch fatigue behaviour needs to be studied in further detail.

3. Is it possible to predict the materials fatigue behaviour using linear elastic models and the energy-based approach of Strain Energy Density (SED)?

   - The SED analysis of the $S-N$ curves are able to be presented in a unified $\Delta\bar{W}-N$ curve, with a small scatter.
   - The critical radius used for the control parameter has been set to 0.25 mm, this is close to the value used for welded steel joints.
   - Post processing should effect the material parameters, therefore its likely that different values of critical radius needs to be employed for different post processing. But the $\Delta\bar{W}-N$ curve allows the engineers to only test one geometry, and based on this estimate the fatigue life of components, rather than testing different notch specimens corresponding to different notched present in the component.
   - The $\Delta\bar{W}-N$ curve obtained for the AM IN718 data fits with 900 weld data on steel joints, and gives approximately the same scatter, and critical value of SED.

Further work:

- IN718 is a material that is usually heat treated in order to increase the mechanical properties, this should be done, investigating the notched fatigue behaviour for different heat treatments, and evaluated at different temperatures.
- The effect of defects such as porosities, surface roughness and lack of fusion should be further investigated as they are likely to be present and have some effect on any AM component produced.
- The effect of machining and HIPing the specimens should be investigated focusing on the effect of the fatigue life, by closing porosities and removing surface defects.

References

[1] Matthew J. Donachie and Stephen J. Donachie. *Superalloys: A Technical Guide*. ASM International, 2002.

[2] John J. Lewandowski and Mohsen Seifi. Metal additive manufacturing: A review of mechanical properties. *Annual Review of Materials Research*, 46(1):151–186, 2016.

[3] Prashanth K G, Sri Kolla, and Jürgen Eckert. Additive manufacturing processes: Selective laser melting, electron beam melting and binder jetting—selection guidelines. *Materials (Basel)*, 10, 06 2017.

[4] Jan Torgersen. Additive manufacturing: From fundamentals to applications. Stanford University - Summer Session, June 2018.

[5] Impression 3D par Stéréolithographie united 3d makers. `https://www.united-3dmakers.com/les-technologies/impression-3d-stereolithographie/`. Accessed: 01-06-2018.

[6] C.W. Hull. Apparatus for production of three-dimensional objects by stereolithography, 4575330, 1986.

[7] Jan Torgersen, Xiao-Hua Qin, Zhiquan Li, Aleksandr Ovsianikov, Robert Liska, and Jurgen Stampfl. Hydrogels for two-photon polymerization: A toolbox for mimicking the extracellular matrix. *Advanced Functional Materials*, 23:4542–4554, 09 2013.

[8] Fused Deposition Modeling (FDM) amfas. `http://www.amfasinternational.com/services/rapid-prototyping/3d-printing/fused-deposition-modeling-fdm/`. Accessed: 01-06-2018.

[9] H. Rezayat, W. Zhou, A. Siriruk, D. Penumadu, and S. S. Babu. Structure–mechanical property relationship in fused deposition modelling. *Materials Science and Technology*, 31(8):895–903, 2015.

[10] CARDIFF UNIVERSITY PURCHASES RENISHAW AM250 FOR METAL 3D PRINTING 3d printing industry. `https://3dprintingindustry.com/news/cardiff-university-renishaw-am250-metal-3d-printing-35782/`. Accessed: 01-06-2018.

[11] S. Tammas-Williams, H. Zhao, F. Léonard, F. Derguti, I. Todd, and P.B. Prangnell. Xct analysis of the influence of melt strategies on defect population in ti–6al–4v components manufactured by selective electron beam melting. *Materials Characterization*, 102:47 – 61, 2015.

[12] Mark Cotteleer and Jim Joyce. 3d opportunity: Additive manufacturing paths to performance, innovation, and growth. *Deloitte Review*, 14, 2015.

[13] Salomé Galjaard, Sander Hofman, and Shibo Ren. *New Opportunities to Optimize Structural Designs in Metal by Using Additive Manufacturing*. 09 2015.

[14] SPACEX LAUNCHES 3D-PRINTED PART TO SPACE, CREATES PRINTED ENGINE CHAMBER. `http://www.spacex.com/news/2014/07/31/spacex-launches-3d-printed-part-space-creates-printed-engine-chamber-crewed`. Accessed: 06-06-2018.

[15] T. L. Anderson. *Fracture Mechanics: Fundamentals and Applications*. CRC Press, 2005.

[16] Norman E. Dowling. *Mechanical Behaviour of Materials*. Pearson Education Limited, 2005.

[17] Kirsch E.G. Die theorie der elastizität und die bedürfnisse der festigkeitslehre. *Zeitschrift des Vereines deutscher Ingenieure*, 42:797–807, 1898.

[18] Inglis C.E. Stresses in plates due to the presence of cracks and sharp corners. *Transactions of the Institute of Naval Architects*, 55:219–241, 1913.

[19] M.L. Williams. Stress singularities resulting from various boundary conditions in angular corners of plates in extension. *Journal of Applied Mechanics*, 19:526–528, 1952.

[20] P. Lazzarin and R. Tovo. A unified approach to the evaluation of linear elastic stress fields in the neighborhood of cracks and notches. *International Journal of Fracture*, 78:3–19, 1996.

[21] ASTM E1820 17a. Standard test method for measurement of fracture toughness. Technical report, ASTM, 2018.

[22] S.J Findlay and N.D Harrison. Why aircraft fail. *Materials Today*, 5(11):18 – 25, 2002.

[23] P A Davies, M Novovic, V Randle, and P Bowen. Application of electron backscatter diffraction (ebsd) to fracture studies of ferritic steels. *Journal of microscopy*, 205:278–84, 04 2002.

[24] J.R Barber. *Elasticity, Solid Mechanics and Its Applications*. Springer Science+Business Media, 2010.

[25] F. Berto and P. Lazzarin. A review of the volume-based strain energy density approach applied to v-notches and welded structures. *Theoretical and Applied Fracture Mechanics*, 52(3):183 – 194, 2009.

[26] P. Livieri and P. Lazzarin. Fatigue strength of steel and aluminium welded joints based on generalised stress intensity factors and local strain energy values. *International Journal of Fracture*, 133(3):247–276, Jun 2005.

[27] P. Lazzarin and R. Zambardi. A finite-volume-energy based approach to predict the static and fatigue behavior of components with sharp v-shaped notches. *International Journal of Fracture*, 112(3):275–298, Dec 2001.

[28] P. Lazzarin, F. Berto, F.J. Gomez, and M. Zappalorto. Some advantages derived from the use of the strain energy density over a control volume in fatigue strength assessments of welded joints. *International Journal of Fatigue*, 30(8):1345 – 1357, 2008.

[29] Nickel Based Superalloys, University of Cambridge. `http://www.phase-trans.msm.cam.ac.uk/2003/Superalloys/superalloys.html`. Accessed: 06-06-2018.

[30] Bryton Farber, Kathryn A. Small, Christopher Allen, Robert J. Causton, Ashley Nichols, John Simbolick, and Mitra L. Taheri. Correlation of mechanical properties to microstructure in metal laser sintering inconel 718. *Materials Science and Engineering: A*, 712:539 – 547, 2018.

[31] K.N. Amato, S.M. Gaytan, L.E. Murr, E. Martinez, P.W. Shindo, J. Hernandez, S. Collins, and F. Medina. Microstructures and mechanical behavior of inconel 718 fabricated by selective laser melting. *Acta Materialia*, 60(5):2229 – 2239, 2012.

[32] M. G. Stout and W. W. Gerberich. Structure/property/continuum synthesis of ductile fracture in inconel alloy 718. *Metallurgical Transactions A*, 9(5):649–658, May 1978.

[33] Kawagoishi, Chen, and Nisitani. Fatigue strength of inconel 718 at elevated temperatures. *Fatigue and Fracture of Engineering Materials and Structures*, 23(3):209–216, 2000.

[34] Qiang Chen, Norio Kawagoishi, and Hironobu Nisitani. Evaluation of notched fatigue strength at elevated temperature by linear notch mechanics. *International Journal of Fatigue*, 21(9):925 – 931, 1999.

[35] D. Fournier and A. Pineau. Low cycle fatigue behavior of inconel 718 at 298 k and 823 k. *Metallurgical Transactions A*, 8(7):1095–1105, Jul 1977.

[36] J.P. Pédron and A. Pineau. The effect of microstructure and environment on the crack growth behaviour of inconel 718 alloy at 650 °c under fatigue, creep and combined loading. *Materials Science and Engineering*, 56(2):143 – 156, 1982.

[37] ISO/ASTM 52921. Standard terminology for additive manufacturing - coordinate systems and test methodologies. Technical report, ISO/ASTM, 2013.

[38] John J. Lewandowski and Mohsen Seifi. Metal additive manufacturing: A review of mechanical properties. *Annual Review of Materials Research*, 46(1):151–186, 2016.

[39] O. Scott-Emuakpor, J. Schwartz, T. George, C. Holycross, C. Cross, and J. Slater. Bending fatigue life characterisation of direct metal laser sintering nickel alloy 718. *Fatigue & Fracture of Engineering Materials & Structures*, 38(9):1105–1117, 2015.

[40] Johannes Strößner, Michael Terock, and Uwe Glatzel. Mechanical and microstructural investigation of nickel-based superalloy in718 manufactured by selective laser melting (slm). *Advanced Engineering Materials*, 17(8):1099–1105, 2015.

[41] L. E. Murr, E. Martinez, S. M. Gaytan, D. A. Ramirez, B. I. Machado, P. W. Shindo, J. L. Martinez, F. Medina, J. Wooten, D. Ciscel, U. Ackelid, and R. B. Wicker. Microstructural architecture, microstructures, and mechanical properties for a nickel-base superalloy fabricated by electron beam melting. *Metallurgical and Materials Transactions A*, 42(11):3491–3508, Nov 2011.

[42] Bernd Baufeld. Mechanical properties of inconel 718 parts manufactured by shaped metal deposition (smd). *Journal of Materials Engineering and Performance*, 21(7):1416–1421, Jul 2012.

[43] P.L. Blackwell. The mechanical and microstructural characteristics of laser-deposited in718. *Journal of Materials Processing Technology*, 170(1):240 – 246, 2005.

[44] Xiaoming Zhao, Jing Chen, Xin Lin, and Weidong Huang. Study on microstructure and mechanical properties of laser rapid forming inconel 718. *Materials Science and Engineering: A*, 478(1):119 – 124, 2008.

[45] M.M. Kirka, D.A. Greeley, C. Hawkins, and R.R. Dehoff. Effect of anisotropy and texture on the low cycle fatigue behavior of inconel 718 processed via electron beam melting. *International Journal of Fatigue*, 105:235 – 243, 2017.

[46] F. Caiazzo, V. Alfieri, G. Corrado, and P. Argenio. Mechanical properties of inconel 718 in additive manufacturing via selective laser melting: An investigation on possible anisotropy of tensile strength. In *2017 IEEE 3rd International Forum on Research and Technologies for Society and Industry (RTSI)*, pages 1–4, Sept 2017.

[47] W.E. Luecke and J.A. Slotwinski. Mechanical properties of austenitic stainless steel made by additive manufacturing. *Journal of Research of the National Institute of Standards and Technology*, 119:398–418, 2014.

[48] Alex S. Johnson, Shuai Shao, Nima Shamsaei, Scott M. Thompson, and Linkan Bian. Microstructure, fatigue behavior, and failure mechanisms of direct laser-deposited inconel 718. *JOM*, 69(3):597–603, Mar 2017.

[49] D. Wells. Overview of fatigue and damage tolerance performance of powder bed fusion alloy n07718. *NASA Marshall Sp. Flight Cent*, 2016.

[50] Aref Yadollahi and Nima Shamsaei. Additive manufacturing of fatigue resistant materials: Challenges and opportunities. *International Journal of Fatigue*, 98:14 – 31, 2017.

[51] E. Madenci and I. Guven. *The finite element method and applications in engineering using ANSYS®, second edition*. 2015. cited By 27.

[52] Abaqus Analysis User's Manual. 24.1.1 element library: overview.

[53] Inconel alloy 718 - Special Metals. `http://www.specialmetals.com/assets/smc/documents/inconel_alloy_718.pdf`. Accessed: 06-06-2018.

[54] P. Lazzarin and S. Filippi. A generalized stress intensity factor to be applied to rounded v-shaped notches. *International Journal of Solids and Structures*, 43(9):2461 – 2478, 2006.

[55] S. Tammas-Williams, P.J. Withers, I. Todd, and P.B. Prangnell. The influence of porosity on fatigue crack initiation in additively manufactured titanium components. *Scientific Reports*, 7(1), 2017. cited By 8.

List of Figures

List of Tables

Appendices

A Stress fields

In this appendix a more thorough review of linear elastic stress fields is given. First a singularity criterion is given, then Airy stress function is presented. Williams' solution and Lazzarin-Tovo's solution for stress fields in linear elastic materials is described in more detail than in section 3.4. The derivation of these models are not complete but the main steps are reproduced.

A.1 Airy stress function

The Airy stress function, Φ, is a function from which the stresses in a body can be derived. The following section is adapted from Anderson [15].

A.1.1 Cartesian coordinates

Equilibrium conditions:

$$\frac{\partial \sigma_{xx}}{\partial x} + \frac{\partial \tau_{xy}}{\partial y} = 0, \quad \frac{\partial \sigma_{yy}}{\partial y} + \frac{\partial \tau_{xy}}{\partial x} = 0 \tag{40}$$

Compatibility equation:

$$\nabla^2(\sigma_{xx} + \sigma_{yy}) = 0, \quad \nabla^2 = \frac{\partial^2}{\partial x^2} + \frac{\partial^2}{\partial y^2} \tag{41}$$

The Airy stress function is a function from which the stresses can be derived

$$\sigma_{xx} = \frac{\partial^2 \Phi}{\partial y^2}, \quad \sigma_{yy} = \frac{\partial^2 \Phi}{\partial x^2}, \quad \tau_{xy} = -\frac{\partial^2 \Phi}{\partial y \partial x} \tag{42}$$

From the equilibrium conditions and compatibility equation:

$$\frac{\partial^4 \Phi}{\partial x^4} + 2\frac{\partial^4 \Phi}{\partial x^2 \partial y^2} + \frac{\partial^4 \Phi}{\partial y^4} = 0, \qquad \nabla^2 \nabla^2 \Phi = 0 \tag{43}$$

A.1.2 Polar coordinates

$$\sigma_{rr} = \frac{1}{r^2}\frac{\partial^2 \Phi}{\partial \theta^2} + \frac{1}{r}\frac{\partial \Phi}{\partial r}, \quad \sigma_{\theta\theta} = \frac{\partial^2 \Phi}{\partial r^2}, \quad \tau_{r\theta} = -\frac{1}{r}\frac{\partial^2 \Phi}{\partial r \partial \theta} + \frac{1}{r^2}\frac{\partial \Phi}{\partial \theta} \tag{44}$$

A.2 Singularities

For engineering purposes linear-elastic material models are convenient. In real materials there is no singularities, the material will yield, and the stresses will redistribute. This section is reproduced from J.R Barber[24].

The strength of acceptable singularies shall be determined. Acceptable singularieties: those for which the total strain energy in a small region surrounding the singular point vanishes as the size of the region tends to zero. If the stress varies with r^a as the point $r = 0$ is approached, the strain energy will be on the form:

$$U = \int_0^{2\pi} \int_0^r \sigma_{ij} e_{ij} r dr d\theta = C \int_0^r r^{2a+1} dr \tag{45}$$

If $a > -1$ the integral in bounded, if $a \leq -1$ the integral is unbounded. Singular stress fields are acceptable if $a > -1$ and not for $a \leq -1$.

A.3 Williams' Solution

The following section is reproduced from J.R Barber [24]. Williams developed a method for determining the stress fields at the tip a sharp notch (v-shaped notch). A semi infinite wedge element is used. The angles are set to be 2α, such that the wedge forms a sharp notch. At the tip of the notch, a polar coordinate system is defined.

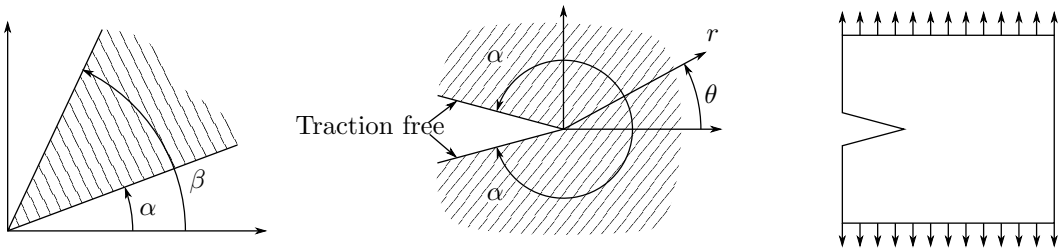

Figure 73: Left: Arbitrary wedge element. Middle: Semi-infinite sharp notch. Right: Notched plate in tension.

Willams postulated the following Airy stress function:

$$\Phi = r^{\lambda+1}[A_1 \sin(\lambda+1)\theta^* + A_2 \cos(\lambda+1)\theta^* + A_3 \sin(\lambda-1)\theta^* + A_4 \cos(\lambda-1)\theta^*] = r^{\lambda+1}\Phi(\theta^*, \lambda) \tag{46}$$

Giving the following stress field:

$$\begin{aligned} \sigma_{rr} = r^{\lambda-1}[&-A_1\lambda(\lambda+1)\cos(\lambda+1)\theta - A_2\lambda(\lambda-3)\cos(\lambda-1)\theta \\ &- A_3\lambda(\lambda+1)\sin(\lambda+1)\theta - A_4\lambda(\lambda-3)\sin(\lambda-1)\theta] \end{aligned} \tag{47}$$

$$\begin{aligned} \sigma_{\theta\theta} = r^{\lambda-1}[&A_1\lambda(\lambda+1)\sin(\lambda+1)\theta + A_2\lambda(\lambda-1)\sin(\lambda-1)\theta \\ &- A_3\lambda(\lambda+1)\cos(\lambda+1)\theta - A_4\lambda(\lambda-1)\cos(\lambda-1)\theta] \end{aligned} \tag{48}$$

$$\begin{aligned} \tau_{r\theta} = r^{\lambda-1}[&A_1\lambda(\lambda+1)\cos(\lambda+1)\theta + A_2\lambda(\lambda+1)\cos(\lambda-1)\theta \\ &+ A_3\lambda(\lambda+1)\sin(\lambda+1)\theta + A_4\lambda(\lambda+1)\sin(\lambda-1)\theta] \end{aligned} \tag{49}$$

Boundary conditions, so that surface of crack is traction free:

$$\sigma_{\theta\theta} = \tau_{r\theta} = 0; \quad \theta = +\alpha \tag{50}$$

$$\begin{aligned} 0 = \lambda[&A_1(\lambda+1)\sin(\lambda+1)\alpha - A_2(\lambda-1)\sin(\lambda-1)\alpha \\ &- A_3(\lambda+1)\cos(\lambda+1)\alpha - A_4(\lambda-1)\cos(\lambda-1)\alpha] \end{aligned} \tag{51}$$

$$\begin{aligned} 0 = \lambda[&-A_1(\lambda+1)\sin(\lambda+1)\alpha - A_2(\lambda-1)\sin(\lambda-1)\alpha \\ &- A_3(\lambda+1)\cos(\lambda+1)\alpha - A_4(\lambda-1)\cos(\lambda-1)\alpha] \end{aligned} \tag{52}$$

$$\sigma_{\theta\theta} = \tau_{r\theta} = 0; \quad \theta = -\alpha \tag{53}$$

$$\begin{aligned} 0 = \lambda[&A_1(\lambda+1)\sin(\lambda+1)\alpha + A_2(\lambda-1)\sin(\lambda-1)\alpha \\ &+ A_3(\lambda+1)\cos(\lambda+1)\alpha + A_4(\lambda-1)\cos(\lambda-1)\alpha] \end{aligned} \tag{54}$$

$$\begin{aligned} 0 = \lambda[&A_1(\lambda+1)\sin(\lambda+1)\alpha + A_2(\lambda-1)\sin(\lambda-1)\alpha \\ &- A_3(\lambda+1)\cos(\lambda+1)\alpha - A_4(\lambda-1)\cos(\lambda-1)\alpha] \end{aligned} \tag{55}$$

This gives 4 homogeneous sets of equations of λ:

$$A_1(\lambda+1)\sin(\lambda+1)\alpha + A_2(\lambda-1)\sin(\lambda-1)\alpha = 0 \tag{56}$$

$$A_1(\lambda+1)\cos(\lambda+1)\alpha + A_2(\lambda+1)\cos(\lambda-1)\alpha = 0 \tag{57}$$

$$A_3(\lambda+1)\cos(\lambda+1)\alpha + A_4(\lambda-1)\cos(\lambda-1)\alpha = 0 \tag{58}$$

$$A_3(\lambda+1)\sin(\lambda+1)\alpha + A_4(\lambda+1)\sin(\lambda-1)\alpha = 0 \tag{59}$$

Which can be formed into two independent sets of equations:

$$\begin{bmatrix} (\lambda+1)\sin(\lambda+1)\alpha & (\lambda-1)\sin(\lambda-1)\alpha \\ (\lambda+1)\cos(\lambda+1)\alpha & (\lambda+1)\cos(\lambda-1)\alpha \end{bmatrix} \begin{bmatrix} A_1 \\ A_2 \end{bmatrix} = \begin{bmatrix} 0 \\ 0 \end{bmatrix} \tag{60}$$

$$\begin{bmatrix} (\lambda+1)\cos(\lambda-1)\alpha & (\lambda-1)\cos(\lambda-1)\alpha \\ (\lambda+1)\sin(\lambda+1)\alpha & (\lambda+1)\sin(\lambda-1)\alpha \end{bmatrix} \begin{bmatrix} A_3 \\ A_4 \end{bmatrix} = \begin{bmatrix} 0 \\ 0 \end{bmatrix} \tag{61}$$

Equation 60 gives symmetric terms for A_1 and A_2 if the determinant of the matrix is zero:

$$\lambda\sin(2\alpha) + \sin(2\lambda\alpha) = 0 \tag{62}$$

Equation 61 gives asymmetric terms for A_3 and A_4 if the determinant of the matrix is zero:

$$\lambda\sin(2\alpha) - \sin(2\lambda\alpha) = 0 \tag{63}$$

Figure 74 shows a plot of the lowest eigenvalue of equation 62 and 63. The lowest eigenvalue will determine the strongest singularity.

From Equation 47 - 49 the stress components are proportional to $r^{\lambda-1}$. From the mathematical singularity criterion for elasticity in section A.2: $\lambda > 0$. In the case of a crack, $2\alpha = 360^o$ and $\lambda_1 = \lambda_2 = 0.5$. In the case of an unnotched specimen $2\alpha = 180^o$ and $\lambda_1 = \lambda_2 = 1$.

Solving the Equation 62 $\lambda = \lambda_S$. Equation XX YY will not be linearly dependent and can be solved for A_1 and A_2 such that:

$$A_1 = A(\lambda_s - 1)\sin(\lambda_s - 1)\alpha \tag{64}$$

$$A_2 = -A(\lambda_s + 1)\sin(\lambda_s + 1)\alpha \tag{65}$$

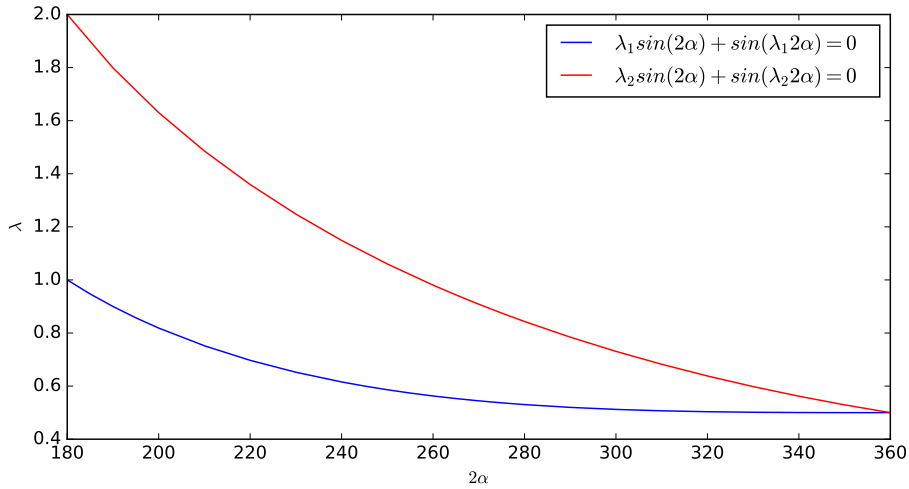

Figure 74: Lowest eigenvalue of λ plotted against 2α. λ_1 is the symmetric term and λ_2 is the asymmetric term.

This will produce the following airy stress function:

$$\phi_S = Ar^{\lambda_s+1}[(\lambda_s - 1)\sin(\lambda_s - 1)\alpha\cos(\lambda_s + 1)\theta - (\lambda_s + 1)\sin(\lambda_s + 1)\alpha\cos(\lambda_s - 1)\theta] \quad (66)$$

The same is done for the asymmetric stress field.

$$\phi_A = Br^{\lambda_A+1}[(\lambda_A + 1)\sin(\lambda_A - 1)\alpha\sin(\lambda_A + 1)\theta - (\lambda_s + 1)\sin(\lambda_A + 1)\alpha\sin(\lambda_A - 1)\theta] \quad (67)$$

For a crack $\lambda_S = \lambda_A = 0.5$. Setting $3A\sqrt{\pi/2} = K_I$ and using Equation 42 in polar coordinates the following components of the symmetric stress field is obtained:

$$\sigma_{rr} = \frac{K_I}{\sqrt{2\pi r}}\left[\frac{5}{4}\cos\left(\frac{\theta}{2}\right) - \frac{1}{4}\cos\left(\frac{3\theta}{2}\right)\right] \quad (68)$$

$$\sigma_{\theta\theta} = \frac{K_I}{\sqrt{2\pi r}}\left[\frac{3}{4}\cos\left(\frac{\theta}{2}\right) + \frac{1}{4}\cos\left(\frac{3\theta}{2}\right)\right] \quad (69)$$

$$\tau_{r\theta} = \frac{K_I}{\sqrt{2\pi r}}\left[\frac{1}{4}\sin\left(\frac{\theta}{2}\right) + \frac{1}{4}\sin\left(\frac{3\theta}{2}\right)\right] \quad (70)$$

For the asymmetric stress field the following result is obtained:

$$\sigma_{rr} = \frac{K_{II}}{\sqrt{2\pi r}}\left[-\frac{5}{4}\sin\left(\frac{\theta}{2}\right) + \frac{3}{4}\sin\left(\frac{3\theta}{2}\right)\right] \quad (71)$$

$$\sigma_{\theta\theta} = \frac{K_{II}}{\sqrt{2\pi r}}\left[-\frac{3}{4}\sin\left(\frac{\theta}{2}\right) - \frac{3}{4}\sin\left(\frac{3\theta}{2}\right)\right] \quad (72)$$

$$\tau_{r\theta} = \frac{K_{II}}{\sqrt{2\pi r}}\left[\frac{1}{4}\cos\left(\frac{\theta}{2}\right) + \frac{3}{4}\cos\left(\frac{3\theta}{2}\right)\right] \quad (73)$$

K_I corresponds to mode I loading and K_{II} corresponds to mode II loading.

A.4 Lazzarin-Tovo

The following section is reproduced from P. Lazzarin and R.Tovo [20]. The method gives a unifying mathematical approach for evaluation linear elastic stress fields around cracks, sharp notches and blunt notches, as shown in Figure 75.

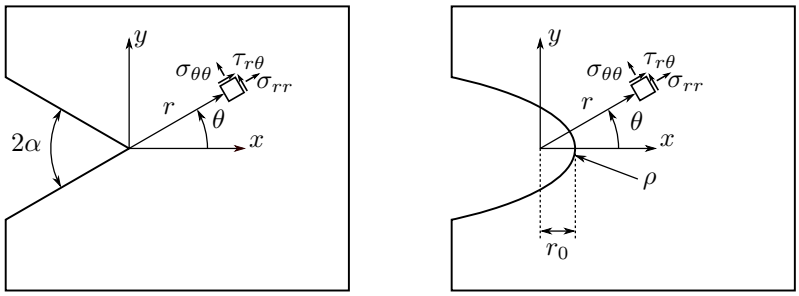

Figure 75: Geometry, stress components and coordinate system for the Lazzarin-Tovo solution. Left: Sharp notch, coordinate system at notch tip. Right: Blunt notch, coordinate system at distance r_0 from notch tip.

The stress field is based on Kolosoff-Muskelishvili's method using the following potential function, with real and complex components:

$$\phi(z) = az^{\lambda}, \quad \psi(z) = bz^{\lambda} + cz^{\mu} \tag{74}$$

From this the stresses can be written as:

$$\sigma_{\theta\theta} = \lambda r^{\lambda-1}[a_1(1+\lambda)\cos(1-\lambda)\theta + a_2\lambda(1+\lambda)\sin(1-\lambda)\theta + b_1\cos(1+\lambda)\theta - b_2\sin(1+\lambda)\theta] \tag{75}$$
$$+\mu r^{\mu-1}[c_1\cos(1+\mu)\theta - c_2\sin(1+\mu)\theta]$$
$$\sigma_{rr} = \lambda r^{\lambda-1}[a_1(3-\lambda)\cos(1-\lambda)\theta + a_2(3-\lambda)\sin(1-\lambda)\theta - b_1\cos(1+\lambda)\theta + b_2\sin(1+\lambda)\theta] \tag{76}$$
$$+\mu r^{\mu-1}[-c_1\cos(1+\mu)\theta + c_2\sin(1+\mu)\theta]$$
$$\tau_{r\theta} = \lambda r^{\lambda-1}[a_1(1-\lambda)\sin(1-\lambda)\theta - a_2(1-\lambda)\cos(1-\lambda)\theta + b_1\sin(1+\lambda)\theta + b_2\cos(1+\lambda)\theta] \tag{77}$$
$$+\mu r^{\mu-1}[c_1\sin(1+\mu)\theta + c_2\cos(1+\mu)\theta]$$

A.4.1 Coordinate system

A new coordinate system is defined in order to be able to impose the correct boundary conditions to the notch. The coordinate system is curvilinear in order to describe the notch geometry. The coordinate system: $z = x + iy$ is replaced with $w = u + iv$:

$$x + iy = re^{i\theta} = z = w^q = (u + iv)^q \tag{78}$$

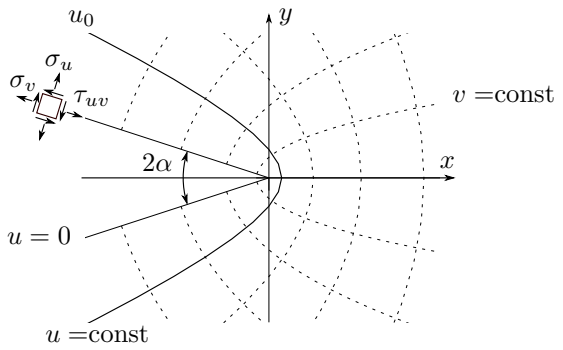

Figure 76: Coordinate system from Lazzarin-Tovo stress field. The Cartesian coordinate system(x, y) is replaced with a curvilinear coordinate system (u, v) in order to describe an arbitrary notch geometry.

The coordinate system is shown in Figure 76. $u = 0$ describes a sharp angle, while any constant positive value of u describes a smooth notch. The opening angle (along $u = 0$) 2α can be expressed in terms of q:

$$2\alpha = \pi(2 - q) \tag{79}$$

The radius, ρ, of the notch at the abscissa axis is given by:

$$\rho = \frac{qr_0}{q - 1} \tag{80}$$

Figure 77 shows the curvilinear coordinate system for different values of q. A crack can be described by $q = 2$ along $u = 0$. When $2 > q > 0$ a sharp notch will be described along $u = 0$. When $q = 1$ a unotched geometry is decribed for all values of u.

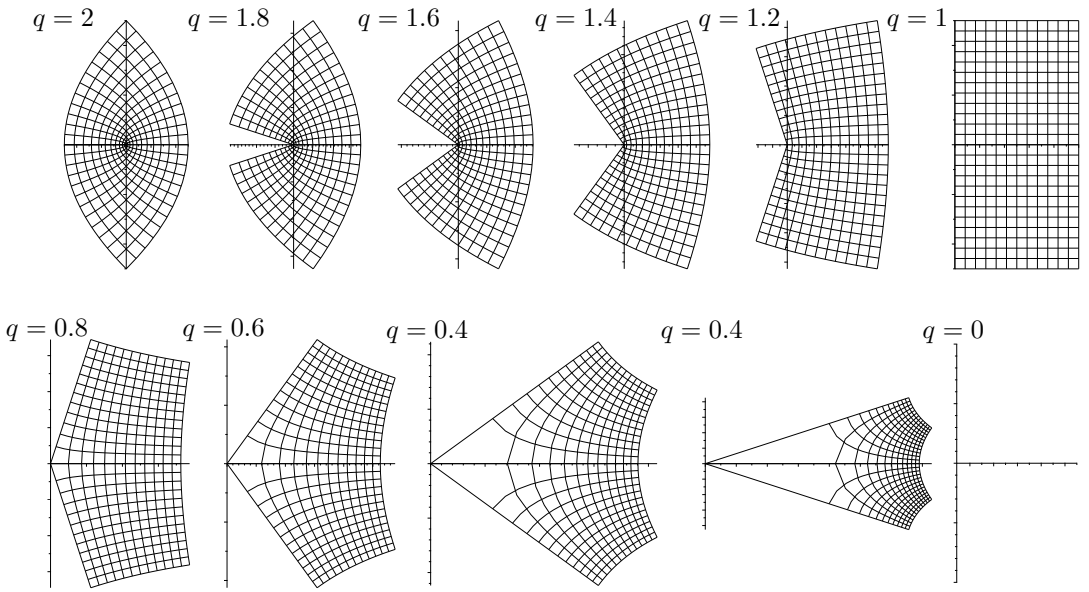

Figure 77: Curvilinear coordinate system for different values of q.

A.4.2 Boundary conditions

In curvilinear coordinates the stress components can be written as:

$$\sigma_{uu} = \frac{1}{2}(\sigma_{rr} + \sigma_{\theta\theta}) + \frac{1}{2}(\sigma_{rr} - \sigma_{\theta\theta})\cos\frac{2\theta}{q} - \tau_{r\theta}\sin\frac{2\theta}{q} \tag{81}$$

$$\sigma_{vv} = \frac{1}{2}(\sigma_{rr} + \sigma_{\theta\theta}) - \frac{1}{2}(\sigma_{rr} - \sigma_{\theta\theta})\cos\frac{2\theta}{q} + \tau_{r\theta}\sin\frac{2\theta}{q} \tag{82}$$

$$\tau_{uv} = \frac{1}{2}(\sigma_{rr} + \sigma_{\theta\theta})\sin\frac{2\theta}{q} + \tau_{r\theta}\sin\frac{2\theta}{q} \tag{83}$$

Along the surface of a notch the two following boundary conditions are given:

$$(\sigma_{uu})_{u=u_0} = 0, \qquad (\tau_{uv})_{u=u_0} = 0 \tag{84}$$

The mathematcial model are used to describe the stresses in the areas close to the notch tip, and will only be valid in a certain distance away from this. After these boundary conditions are applied for the correct distance from the notch tip, the stress field can be described.

A.4.3 Paramters and constants

According to the boundary conditions the following system is obtaied (the same as in Williams' solution):

$$\begin{bmatrix} (\lambda+1)\cos(1-\lambda)\frac{q\pi}{2} & \cos(1+\lambda)\frac{q\pi}{2} & 0 & 0 \\ (\lambda-1)\sin(1-\lambda)\frac{q\pi}{2} & \sin(1+\lambda)\frac{q\pi}{2} & 0 & 0 \\ 0 & 0 & (\lambda+1)\sin(1-\lambda)\frac{q\pi}{2} & -\sin(1+\lambda)\frac{q\pi}{2} \\ 0 & 0 & (\lambda-1)\cos(1-\lambda)\frac{q\pi}{2} & -\cos(1+\lambda)\frac{q\pi}{2} \end{bmatrix} \begin{bmatrix} a_1 \\ b_1 \\ a_2 \\ b_2 \end{bmatrix} = \mathbf{0} \tag{85}$$

This gives the following expressions for λ:

$$\sin(\lambda_1 q\pi) + \lambda_1 \sin(q\pi) = 0 \tag{86}$$

$$\sin(\lambda_2 q\pi) - \lambda_2 \sin(q\pi) = 0 \tag{87}$$

The solution to Equation 86 and 87, gives the eigenvalues. Equation 86 gives λ_1 corresponding to mode I loading, while Equation 87 gives λ_2 corresponding to mode II loading.

The constants, a_1, b_1, a_2 and b_2 are given by:

$$b_{1n} = a_{1n}(1-\lambda_{1n})X_{1n}, \quad b_{2n} = -a_{2n}(1-\lambda_{2n})X_{2n} \tag{88}$$

Where the coefficient X_{ik} are given:

$$X_{ik} = -\frac{\sin(1-\lambda_{ik})q\pi/2}{\sin(1+\lambda_{ik})q\pi/2} \tag{89}$$

A.4.4 General formulation of stress components

Mode I

$$\begin{bmatrix} \sigma_{\theta\theta} \\ \sigma_{rr} \\ \tau_{r\theta} \end{bmatrix} = \lambda_1 r^{\lambda_1 - 1} \alpha_1 \left[\left[\begin{bmatrix} (1+\lambda_1)\cos(1-\lambda_1)\theta \\ (3-\lambda_1)\cos(1-\lambda_1)\theta \\ (1-\lambda_1)\cos(1-\lambda_1)\theta \end{bmatrix} + X_1(1-\lambda_1) \begin{bmatrix} \cos(1+\lambda_1)\theta \\ -\cos(1+\lambda_1)\theta \\ \sin(1+\lambda_1)\theta \end{bmatrix} \right] \right.$$
$$\left. + \left(\frac{r}{r_0}\right)^{\mu_1 - \lambda_1} [(3-\lambda_1) - X_1(1-\lambda_1)] \begin{bmatrix} \cos(1+\mu_1)\theta \\ -\cos(1+\mu_1)\theta \\ \sin(1+\mu_1)\theta \end{bmatrix} \right] \quad (90)$$

Mode II

$$\begin{bmatrix} \sigma_{\theta\theta} \\ \sigma_{rr} \\ \tau_{r\theta} \end{bmatrix} = \lambda_2 r^{\lambda_2 - 1} \alpha_2 \left[\left[\begin{bmatrix} (1+\lambda_2)\sin(1-\lambda_2)\theta \\ (3-\lambda_2)\sin(1-\lambda_2)\theta \\ (1-\lambda_2)\cos(1-\lambda_2)\theta \end{bmatrix} + X_2(1+\lambda_2) \begin{bmatrix} \sin(1+\lambda_2)\theta \\ -\sin(1+\lambda_2)\theta \\ \cos(1+\lambda_2)\theta \end{bmatrix} \right] \right.$$
$$\left. - \left(\frac{r}{r_0}\right)^{\mu_2 - \lambda_2} [(1-\lambda_2) + X_2(1+\lambda_1)] \begin{bmatrix} \sin(1+\mu_2)\theta \\ -\sin(1+\mu_2)\theta \\ \cos(1+\mu_2)\theta \end{bmatrix} \right] \quad (91)$$

The stress components can be expressed by the stress field parameter K.

$$K_I = \sqrt{2\pi} \lim_{r \to 0} (\sigma_{\theta\theta})_{\theta=0} r^{1-\lambda_1}, \quad K_{II} = \sqrt{2\pi} \lim_{r \to 0} (\tau_{r\theta})_{\theta=0} r^{1-\lambda_2} \quad (92)$$

The coefficients a_1 and a_2 are then expressed as:

$$\alpha_1 = \frac{K_I}{\lambda_1 \sqrt{2\pi}[(1+\lambda_1) + X_1(1-\lambda_1]}, \quad \alpha_2 = \frac{K_{II}}{\lambda_2 \sqrt{2\pi}[(1-\lambda_2) + X_1(1+\lambda_2]} \quad (93)$$

The stress field for mode I loading can be expressed as:

$$\begin{bmatrix} \sigma_{\theta\theta} \\ \sigma_{rr} \\ \tau_{r\theta} \end{bmatrix} = \frac{1}{\sqrt{2\pi}} \frac{r^{\lambda_1 - 1} K_I}{(1+\lambda_1) + X(1-\lambda_1)} \left[\left[\begin{bmatrix} (1+\lambda_1)\cos(1-\lambda_1)\theta \\ (3-\lambda_1)\cos(1-\lambda_1)\theta \\ (1-\lambda_1)\cos(1-\lambda_1)\theta \end{bmatrix} \right. \right.$$
$$\left. + X_1(1-\lambda_1) \begin{bmatrix} \cos(1+\lambda_1)\theta \\ -\cos(1+\lambda_1)\theta \\ \sin(1+\lambda_1)\theta \end{bmatrix} \right]$$
$$+ \left(\frac{r}{r_0}\right)^{\mu_1 - \lambda_1} [(3-\lambda_1) - X_1(1-\lambda_1)] \left. \begin{bmatrix} \cos(1+\mu_1)\theta \\ -\cos(1+\mu_1)\theta \\ \sin(1+\mu_1)\theta \end{bmatrix} \right] \quad (94)$$

The stress field for mode II loading can be expressed as:

$$\begin{bmatrix} \sigma_{\theta\theta} \\ \sigma_{rr} \\ \tau_{r\theta} \end{bmatrix} = \frac{1}{\sqrt{2\pi}} \frac{r^{\lambda_2 - 1} K_{II}}{(1-\lambda_2) + X(1+\lambda_2)} \Bigg[\Bigg[\begin{bmatrix} -(1+\lambda_2)\sin(1-\lambda_2)\theta \\ -(3-\lambda_2)\sin(1-\lambda_2)\theta \\ (1-\lambda_2)\cos(1-\lambda_2)\theta \end{bmatrix} + X_2(1+\lambda_2) \begin{bmatrix} -\sin(1+\lambda_2)\theta \\ \sin(1+\lambda_2)\theta \\ \cos(1+\lambda_2)\theta \end{bmatrix} \Bigg] - \left(\frac{r}{r_0}\right)^{\mu_2 - \lambda_2} [(1-\lambda_2) + X_2(1+\lambda_1)] \begin{bmatrix} \sin(1+\mu_2)\theta \\ -\sin(1+\mu_2)\theta \\ -\cos(1+\mu_2)\theta \end{bmatrix} \Bigg] \tag{95}$$

A.4.5 William' Solution

Using Lazzarin-Tovos solution for a v-shaped notch (and cracks), the part relating to r_0 is left out, and the solution is indentical to Williams solution. The stress field for mode I loading is written as:

$$\begin{bmatrix} \sigma_{\theta\theta} \\ \sigma_{rr} \\ \tau_{r\theta} \end{bmatrix} = \frac{1}{\sqrt{2\pi}} \frac{r^{\lambda_1 - 1} K_{I}}{(1+\lambda_1) + X(1-\lambda_1)} \Bigg[\Bigg[\begin{bmatrix} (1+\lambda_1)\cos(1-\lambda_1)\theta \\ (3-\lambda_1)\cos(1-\lambda_1)\theta \\ (1-\lambda_1)\cos(1-\lambda_1)\theta \end{bmatrix} + X_1(1-\lambda_1) \begin{bmatrix} \cos(1+\lambda_1)\theta \\ -\cos(1+\lambda_1)\theta \\ \sin(1+\lambda_1)\theta \end{bmatrix} \Bigg] \tag{96}$$

The stress field for mode II is written as:

$$\begin{bmatrix} \sigma_{\theta\theta} \\ \sigma_{rr} \\ \tau_{r\theta} \end{bmatrix} = \frac{1}{\sqrt{2\pi}} \frac{r^{\lambda_2 - 1} K_{II}}{(1-\lambda_2) + X(1+\lambda_2)} \Bigg[\Bigg[\begin{bmatrix} -(1+\lambda_2)\sin(1-\lambda_2)\theta \\ -(3-\lambda_2)\sin(1-\lambda_2)\theta \\ (1-\lambda_2)\cos(1-\lambda_2)\theta \end{bmatrix} + X_2(1+\lambda_2) \begin{bmatrix} -\sin(1+\lambda_2)\theta \\ \sin(1+\lambda_2)\theta \\ \cos(1+\lambda_2)\theta \end{bmatrix} \Bigg] \tag{97}$$

A.4.6 Creager-Glinka's Solutions

Using Lazzarin-Tovo's solution for a u-shaped notch, Creager-Glinka's solution are obtained. The opening angle $2\alpha = 0$, such that $q = 2$, $\lambda_1 = 0.5$ and $\mu_1 = -0.5$. This gives the following solution:

$$\begin{bmatrix} \sigma_{\theta\theta} \\ \sigma_{rr} \\ \tau_{r\theta} \end{bmatrix} = \frac{K_I}{\sqrt{2\pi}} \Bigg[\frac{1}{4} \Bigg[\begin{bmatrix} 3\cos\theta/2 \\ 5\cos\theta/2 \\ \sin\theta/2 \end{bmatrix} + \begin{bmatrix} \cos 3\theta/2 \\ -\cos 3\theta/2 \\ \sin 3\theta/2 \end{bmatrix} \Bigg] + \frac{\rho}{2r} \begin{bmatrix} \cos\theta/2 \\ -\cos\theta/2 \\ \sin\theta/2 \end{bmatrix} \Bigg]$$
$$= \frac{K_I}{\sqrt{2\pi r}} \begin{bmatrix} \cos(\theta/2((1-\sin^2\theta/2) + \rho/2r) \\ \cos(\theta/2((1+\sin^2\theta/2) - \rho/2r) \\ \sin(\theta/2((\cos^2\theta/2) + \rho/2r) \end{bmatrix} \tag{98}$$

In order to relate the stress field parameter to the maximum stress at the notch tip:

$$K_I = \sigma_{max}\sqrt{\pi\rho}/2 \tag{99}$$

The same can be done for mode II loading.

B Strain Energy Density with different critical radius

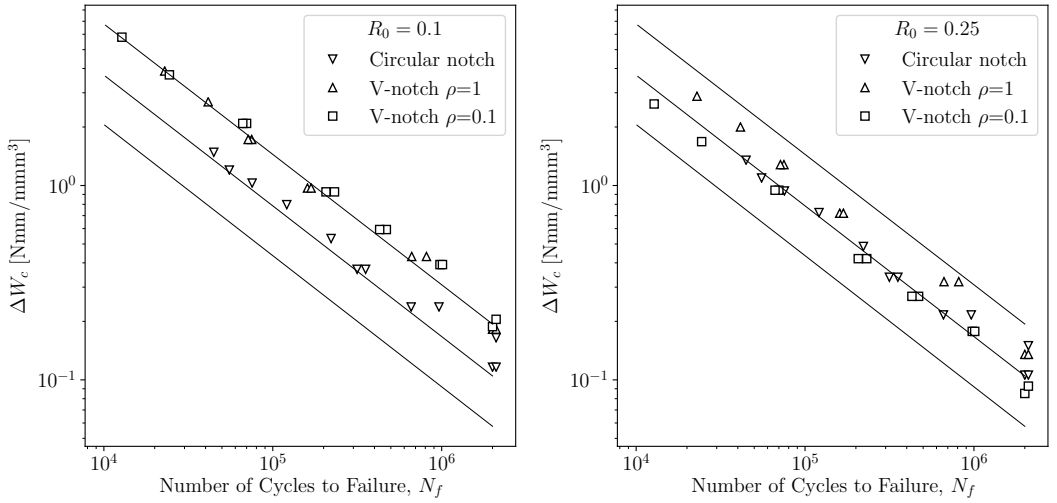

Figure 78: SED of fatigue data with critical radius of 0.1 mm and 0.25 mm.

$\Delta W_c - N$ curves for different values of critical radius is shown in Figure 78. The data is compared with the scatter bands from 900 weld geometries presented in Section 3.7 Figure 28. The SED analysis performed with a control radius of 0.25 fits the data from the welded joints well, as well as giving a one unified curve.